Colloidal Self-Assembly: Particle Synthesis, Functionalisation and Applications

Mykolas Zupkauskas

Sidney Sussex College

Department of Physics

University of Cambridge

This dissertation is submitted for the degree of Doctor of Philosophy

August 2018

ABSTRACT

Colloids, broadly defined as particles small enough to not sediment under gravitational force while dispersed in a continuous medium, are of great scientific and industrial importance. They are present in foods, cosmetics, paints and other materials, often in a jammed or a gelled state. This dissertation explores the self-assembly of hard and soft colloidal particles into mesoscopic structures through modification and control of their surface potentials. Due to its selective binding properties and thermal reversibility, deoxyribonucleic acid (DNA) was used to coat spherical polymeric colloids and subsequently have them assemble into high density colloidal gels. The formation and morphology of one- and two-component colloidal gels was investigated; the use of in-house synthesised fluorinated latex colloids (n = 1.36) allowed for refractive index-matching of such systems in aqueous solutions, greatly aiding the imaging process deep inside dense gels. Additionally, the diffusion of tracer particles in the confinement of the gel structure was investigated. Furthermore, using the same coating technique, oil droplets (ODs) were functionalised with DNA: various sizes and configurations of DNA-coated ODs were investigated with the goal of creating functional oil-in-water emulsions for possible industrial and biotechnological applications. Taking a different assembly approach, 200 nm diameter fluorinated latex particles without any DNA coating were assembled into photonic crystals which, rather than showing iridescence, displayed strong single colour reflectance along with high transmittance, with the reflection colour varying with interparticle distance. Jumping back to colloidal assembly via DNA, rod-sphere structures made from DNA-coated gold nanoparticles and long DNA-coated virions were explored, demonstrating how anisotropic building blocks could create composite structures with increased porosity. Finally, an external magnetic field was shown to aid the assembly of superparamagnetic DNA-coated colloids into long linear constructs, while an additional coating of colloids was shown to stabilise the constructs after the magnetic field had been switched off.

DECLARATION

This dissertation is the result of my own work and includes nothing, which is the outcome of work done in collaboration except where specifically indicated in the text. It is not substantially the same as any that I have submitted, or, is being concurrently submitted for a degree or diploma or other qualification at the University of Cambridge or any other University or similar institution except as declared in the Preface and specified in the text. I further state that no substantial part of my dissertation has already been submitted, or, is being concurrently submitted for any such degree, diploma or other qualification at the University of Cambridge or any other University or similar institution except as declared in the Preface and specified in the text. In accordance with the Department of Physics guidelines, this thesis does not exceed 60,000 words, and it contains fewer than 150 figures.

Mykolas Zupkauskas

Cambridge

ACKNOWLEDGEMENTS

I am writing this with the rest of my dissertation done, having put off this section until the last minute because it is by far one of the most difficult to write.

First and foremost, I would like to thank my supervisors, Erika Eiser and William J. Frith, for their mentorship. Learning new topics and discovering new things is always a daunting task, one that is not without pitfalls and dead ends, and I am thankful to Erika and Bill for their guidance and patience with my silly questions!

To the Eiser Group members, past and present: Darshana, Rob, Taiki and Simon, thank you for teaching me the basics of experimental techniques and your encouragement! My special thank you go to Yang for being my teacher in colloid synthesis and to Zach for helping me with colloid coatings! Zhongyang, Jerome, Alessio, Chris, Iliya, Peicheng and Talha: discussing science and life with you has always been a pleasure! To the newest members of the group, David and Iria; best of luck in the future and thank you for the brief discussions that we have had.

A heartfelt thanks to Rob, Darshana, Tom and Zhongyang for your friendship and support, I feel very lucky to have you as co-workers and friends.

To Tomas and Eglė – thank you for the lunches and dinners together, a time to relax and sometimes share the inevitable miseries of a PhD candidate!

Research is a challenging endeavour and finally I wish to thank the people closest to me – my family – for their support. To my parents, Janina and Stasys, thank you for never doubting me and for your words of encouragement. Lastly, I would like to thank my wife Jūratė, with whom I can share both my successes and my failures. I love you, you are the light in my life and this thesis is for you.

LIST OF PUBLICATIONS

- Z. Ruff, S. H. Nathan, R. R. Unwin, M. Zupkauskas, D. Joshi, G. P. C. Salmond, C. P. Grey and E. Eiser, "Designing disordered materials using DNA-coated colloids of bacteriophage fd and gold," *Faraday Discuss.*, no. 186, pp. 473–488, 2016.
- M. Zupkauskas, Y. Lan, D. Joshi, Z. Ruff, and E. Eiser, "Optically Transparent Dense Colloidal Gels," *Chem. Sci.*, vol. 8, pp. 5559–5566, 2017.
- J. Burelbach, M. Zupkauskas, R. Lamboll, Y. Lan, and E. Eiser, "Colloidal motion under the action of a thermophoretic force," *J. Chem. Phys.*, vol. 147, no. 9, 2017.
- Z. Xing, A. Caciagli, T. Cao, I. Stoev, M. Zupkauskas, T. O'Neill, T. Wenzel, R. Lamboll, D. Liu and E. Eiser, "Microrheology of DNA Hydrogels," *Proc. Natl. Acad. Sci.*, pp. 1–6, 2018.
- A. Caciagli[1], M. Zupkauskas[1], A. Levin, T. P. J. Knowles, C. Mugemana, N. Bruns, T. O'Neill, W. J. Frith and E. Eiser, "DNA-coated Functional Oil Droplets," *Langmuir*, vol. 34, no. 34, pp. 10073–10080, 2018.

  [1] - these authors contributed equally.

- T. Erdem, M. Zupkauskas, T. O'Neill, A. Caciagli, P. Xu, Y. Lan, P. Boesecke and E. Eiser, "Tunable colloidal photonic crystals," 2019. (Manuscript accepted to *Mater. Horiz.*). http://arxiv.org/abs/1808.06260

CONTENTS

LIST OF TABLES

List of Figures

List of Abbreviations and Acronyms

ATR: attenuated total reflectance

BCC: body-centred cubic

DCM: dichloromethane

DDM: differential dynamic microscopy

DLS: dynamic light scattering

DNA: deoxyribonucleic acid

DNACC: DNA-coated colloid

dsDNA: double-stranded DNA

FCC: face-centred cubic

FL: fluorinated latex

FTIR: Fourier transform infrared spectroscopy

HCP: hexagonal close-packing

KPS: potassium persulfate

MsCl: methanesulfonyl chloride

NP: nanoparticle

OD: oil droplet

PB: phosphate buffer

PDI: polydispersity index

PEG: polyethylene glycol

PLL: polylysine

PMMA: poly(methyl methacrylate)

PS: polystyrene

SAXS: small-angle X-ray scattering

SDS: sodium dodecyl sulphate

SEM: scanning electron microscopy

SPAAC: strain-promoted alkyne-azide cycloaddition

ssDNA: single-stranded DNA

SVBS: sodium 4-vinylbenzenesulfonate

TE: Tris EDTA (tris(hydroxymethyl)aminomethane ethylenediaminetetraacetic acid)

TEA: triethylamine

TEM: transmission electron microscopy

THF: tetrahydrofuran

UV-Vis: ultraviolet and visible

LIST OF APPENDICES

1 INTRODUCTION: COLLOIDS AND DNA FUNCTIONALISATION

Colloids are broadly defined as small insoluble particles microscopically dispersed in a continuous medium. The dispersion medium can be solid, liquid or gaseous. The particles themselves are usually solid or liquid and are small enough – typically 1 nm to 10 μm - to not sediment under gravitational force [1]. Colloids are abundant in our everyday lives (fog is an aerosol of water droplets dispersed in air, milk is an emulsion of butterfat droplets in water, mayonnaise is another oil-in-water emulsion, etc.), so they are of immense industrial importance [2, 3]. Moreover, food, pharmaceutical compounds and personal care products frequently contain colloidal structures or active ingredients that are in a metastable arrested phase, e.g. a gelled or jammed structure [4]. Therefore, to construct model systems for such applications, it is important to understand the interactions that govern the behaviour of colloids.

1.1 Colloidal Interactions

1.1.1 Colloid-medium Interactions

The thermal forces exerted on the colloid by the molecules of the surrounding medium should be larger or comparable to the gravitational force: $k_B T \geq |mgz|$, where k_B is the Boltzmann constant, T is the temperature of the system, m is the effective mass of the colloid, g is the gravitational acceleration and z is the characteristic length-scale of the system. As a result, the suspended colloidal particles exhibit stochastic (Brownian) motion, as first mathematically described by Albert Einstein [5]:

$$< \Delta x^2 > = (2n) D \Delta t \,, \tag{1.1}$$

where Δx is the displacement of the particle's position in time Δt, n is the spatial dimension number and D is the diffusion constant. For a purely viscous suspension medium, D is related to the temperature of the medium T, its viscosity η and the radius of the (assumed spherical) particle R via the Stokes-Einstein equation:

$$D = \frac{k_B T}{6\pi\eta R}. \tag{1.2}$$

By tracking the motion of colloids in a suspension, it is then possible to extract information on the viscoelastic properties of said medium; for a complex fluid that exhibits both viscous and elastic behaviour, the above equation can be written in a more general form as [6, 7]:

$$D(s) = \frac{k_B T}{6\pi s\eta(s) R}, \tag{1.3}$$

where $D(s)$ is the Laplace transform of the time dependent diffusion coefficient $D(t)$, $\eta(s)$ is the Laplace transform of the time dependent viscosity and $G(s) = s\eta(s)$ is the Laplace transform of the complex shear modulus.

The process of extracting rheological properties of a medium through the motion of a tracer particle is called micro-rheology and it encompasses many different techniques: particle tracking from video [8, 9], dynamic light scattering (DLS), differential dynamic microscopy (DDM, a method that applies DLS-like correlation analysis to small image fluctuations) [10] and diffusing wave spectroscopy (DWS) [11].

In denser suspensions, colloid-colloid interactions become important. These are outlined below.

1.1.2 Colloid-colloid Interactions

In close proximity, the interactions between non-reactive atoms are repulsive due to the Pauli exclusion principle. Therefore, hard colloidal particles cannot overlap [12].

Dispersion or van der Waals forces arise due to correlations in the fluctuating electric polarisabilities of nearby particles. These forces are long ranged, however, they exceed the thermal forces of colloidal particles only at very short (a few nm) distances. To obtain the interaction potential between two spherical colloids, a few approximations are made: the molecular dipoles are non-interacting, the interactions are non-retarded and pairwise additive. At any given instant, a molecule will have a dipole moment because of the fluctuations in the distribution of the electrons in the molecule. This dipole creates an

electric field that polarises another nearby molecule, and an induced dipole results. The net attractive potential due to two instantaneous dipoles scales as $-\mathrm{C}r^{-6}$, where r is the separation between the dipoles and C is the interatomic pair potential coefficient [12]. It is related to the Hamaker constant $A = \pi^2 \mathrm{C}\rho_1\rho_2$, where ρ_i is the atomic number density in the interacting body *i*. For two spherical colloids, the van der Waals potential can be obtained by integrating over the volumes of the two spherical particles [13]:

$$V_{disp}(r) = -\frac{A}{6}\left\{\frac{2R_1R_2}{r^2-(R_1+R_2)^2} + \frac{2R_1R_2}{r^2-(R_1-R_2)^2} + ln\frac{r^2-(R_1+R_2)^2}{r^2-(R_1-R_2)^2}\right\}, \tag{1.4}$$

where A is the Hamaker constant, R_1 and R_2 are the radii of the interacting colloids and r is the distance between their centres. If we now apply the Derjaguin approximation which assumes that the size of the colloids is much larger than their closest approach distance and that interaction between the two particles decays over a distance much smaller than their size, this expression becomes [13, 14]:

$$V_{disp}(r) = -\frac{A}{6}\frac{R_1R_2}{d(R_1+R_2)}, \tag{1.5}$$

where d is the closest approach between the surfaces of the colloids.

It is worth noting that van der Waals forces are usually attractive, but they can become repulsive between two dissimilar colloids of different electric polarisabilities when the dispersion mediums's electric polarisability lies between the polarisabilities of the two colloids [12]. Another special case is when the colloids are refractive index matched to the dispersion medium; van der Waals forces are then reduced to zero (Clausius-Mossotti relation) [12, 15].

From equation (1.5) we see that a colloidal suspension would flocculate if the surface of the colloids was unmodified in any way. Electrostatic and steric stabilisation are ways of avoiding this. In fact, colloids will almost always have some surface charge, as the surface groups on the colloid can ionise or dissociate, and the particle can also adsorb ions from the solution. The co-ions will then form a tightly-bound Stern layer around the colloid, and a diffuse exponentially decaying electric double-layer further away from the surface [16, 17]. In an electrolyte solution, the electrostatic potential energy between two spherical colloids of radius R and charge Q is then given by:

$$V_{el}(r) = \left\{\frac{Qe^{\kappa R}}{1+\kappa R}\right\}^2 \frac{e^{-\kappa r}}{4\pi\varepsilon r}, \tag{1.6}$$

where r is the distance between their centres. The inverse of κ, in the limit of small potentials (Debye-Hückel approximation) is known as the Debye screening length:

$$\lambda_D = \sqrt{\frac{\varepsilon k_B T}{\sum_i \rho_i^0 q^2{}_i}}, \tag{1.7}$$

where ε is the electric permittivity of the medium, ρ_i^0 is the mean charge density of the ionic species i and q_i is the charge of one ion of species i.

By combining equations (1.4) and (1.6), a potential between two charged colloidal particles of the same radius R was derived by Derjaguin and Landau, and by Verwey and Overbeek independently [16, 18]. It is therefore called the DLVO potential:

$$V_{DLVO}(r) = \left\{\frac{Qe^{\kappa R}}{1+\kappa R}\right\}^2 \frac{e^{-\kappa r}}{4\pi\varepsilon r} - \frac{A}{6}\left\{\frac{2R^2}{r^2-4R^2} + \frac{2R^2}{r^2} + ln\frac{r^2-4R^2}{r^2}\right\}. \tag{1.8}$$

A sketch of a typical DLVO potential between two colloids is shown in Figure 1.1. Red and green solid lines denote the double-layer electrostatic repulsion and the van der Waals attraction, respectively. DLVO potentials are indicated by the dashed lines. At short distances, the van der Waals forces dominate, however, aggregation of colloids is prevented by an electrostatic repulsion barrier and the particles usually end up in the secondary minimum. The height of said barrier depends on the salinity of the dispersion medium (through κ) and the surface charge of the particles (through Q). Adding more electrolytes to the solution lowers the barrier which eventually leads to aggregation.

For completeness, I include a brief overview of other colloid-colloid interactions that need to be considered in colloidal systems, namely hard-sphere repulsion, steric repulsion and depletion interactions.

At short distances, the interaction between colloids is highly repulsive due to the Pauli exclusion principle – the particles cannot interpenetrate. For colloidal particles, this is called the hard-sphere repulsion potential, which is usually an infinite potential at the surface of the colloid. In the DLVO theory, we then have a primary minimum when the particles are in close contact [12, 19].

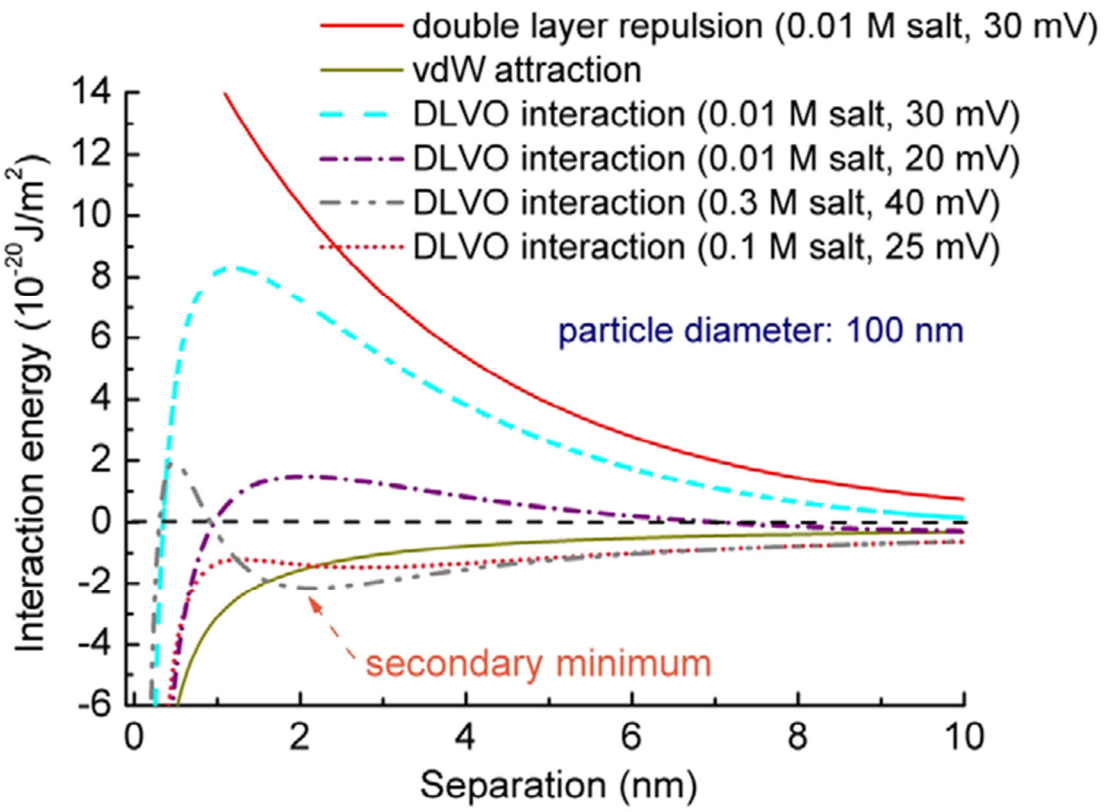

Figure 1.1. A schematic sketch of the DLVO potential. Modified from ref. [19].

Rather than having the colloids charged, another way of preventing flocculation is having them coated with ligands – such as polymers – that provide steric stability. When two such colloids approach each other, the local concentration of the grafted ligand increases, which causes the osmotic pressure to repel the two colloids to increase the entropy [12, 20].

While polymers grafted to the surface of a colloid help stabilise it, free polymers or other small particles in the solution have an opposite effect and give rise to attractive depletion forces. First explained by F. Oosawa and S. Asakura, these forces are entropic in nature and arise because the free polymers (depletants) gain entropy due to the increased available volume when the colloids aggregate [21]. This gain is greater than the loss of entropy of the system due to aggregation.

Figure 1.2 shows colloids (dark red) far apart from each other; they experience an isotropic force and have an exclusion volume (red) proportional to the radius of the depletant (green). When the exclusion volumes start

overlapping (Figure 1.2 b)), the depletants tend to escape from the gap due to reduced entropy in that confinement. Therefore, as the depletants escape from the gap, an

attractive force causes aggregation of the colloids (Figure 1.2 c)). The range of these depletion forces is of the order of the size of the depletant, while the depth of the attraction potential increases with polymer concentration [12, 21].

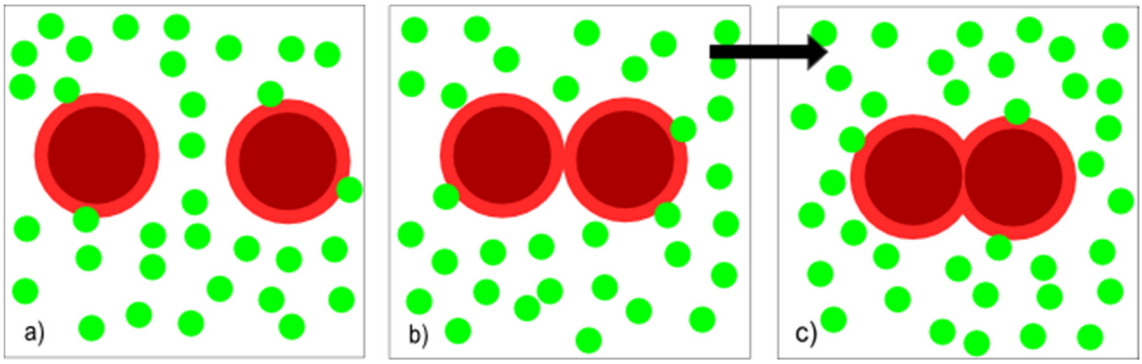

Figure 1.2. A schematic presentation of depletion interaction.

1.2 Functional Colloids and DNA

To convey interaction specificity to colloidal particles, their surface or shape can be modified, which opens up routes for designing self-assembling systems. For example, tuning the surface roughness changes how the particle experiences depletion forces, as shown by Kraft et al. [22], who synthesized dumbbell-shaped particles with one smooth and one rough end. In the presence of a depletant, the smooth side experiences a greater depletion force than the rough side because it has a larger exclusion volume. The colloids can then assemble into micelles; particles with one smooth and two rough parts were then shown to assemble into tubular structures [23]. Another famous example are lock-and-key particles, where the 'lock' colloid has a spherical dimple [24]. This was later extended to include other shapes and patchy particles [25].

Another common method of particle functionalisation is grafting molecules or supramolecular structures to their surface. These include lipids, enzymes, proteins, RNA and DNA [26, 27], and bigger structures such as cucurbit[8]urils (CB[8]). CB[8] is a macrocyclic host molecule, capable of simultaneously encapsulating two guest molecules inside its cavity, forming a stable yet dynamic ternary complex [28, 29]. This thesis focuses on DNA functionalisation, with reasons given below.

1.2.1 DNA

DNA (deoxyribonucleic acid) is best known for coding the genetic information of life. The reason behind its success at making copies of itself and therefore storing information lies in its structure. DNA is a copolymer with a ribose-phosphate backbone and functional

side-chains, Adenine, Cytosine, Guanine and Thymine (A, C, G, T), called bases, attached to each ribose unit [30]. Each base has an affinity for its complementary base: A and T bind with two hydrogen bonds, while C and G bind with three (interestingly, other pairings are possible, but are energetically unfavourable due to the torsion exerted on the backbone) [30]. As the base pairs are hydrophobic, the backbones twist against each other antiparallelly, forming a double helix (Figure 1.3) [31].

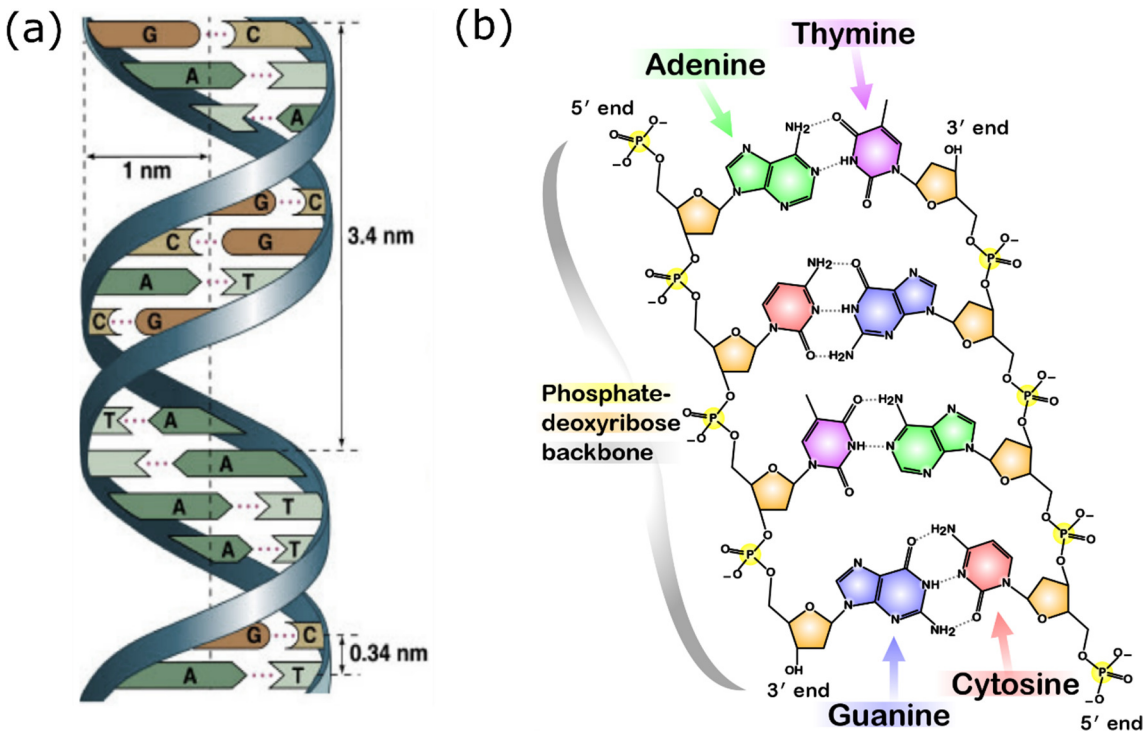

Figure 1.3. A schematic depiction of DNA. (a) Key features of the DNA double helix (taken from [32]). (b) Partial chemical structure of DNA (taken from [33]).

From Figure 1.3 b we see that the two sequences are not symmetric with respect to the backbone. Such sequences, by convention, are listed starting with their initial phosphate group (5') and ending with the final sugar hydroxyl group (3').

The hydrogen bonds between the base pairs are thermally reversible: the melting temperature of a double-stranded DNA (dsDNA) oligomer, T_m, is defined as the temperature at which half of all the available hydrogen bonds between the bases are broken. It depends on the length of the DNA, the specific sequence, the total DNA concentration and the ionic strength of the solution [31, 34, 35]. SantaLucia et al. developed a nearest-neighbour model for predicting the free energy of hybridisation between single-stranded DNA (ssDNA) oligomers [36, 37]; accordingly, the ssDNA oligomers used in this thesis have free energies of hybridisation of the order of tens of $k_B T$, meaning they remain hybridised at room temperature. The tuneable interactions,

coupled with the fact that polymerase chain reaction (PCR) has made artificial DNA strands commercially readily available, makes DNA a very versatile candidate for colloid functionalisation [38, 39].

1.2.2 DNA-coated Colloids

Grafting DNA to the surface of colloids changes the potential of a colloidal system in several ways. Firstly, the DNA backbone is negatively charged, thus it changes the electrostatic potential of a colloid. Secondly, DNA provides steric repulsion at sufficient grafting densities. At low densities, DNA coils up to maximise entropy (ssDNA has a persistence length of ~1 nm), but as the grafting density increases, straight strands become more favourable due to both entropic and electrostatic contributions (see Figure 1.4). dsDNA has a persistence length of ~35 nm and therefore provides even more steric stabilisation [40].

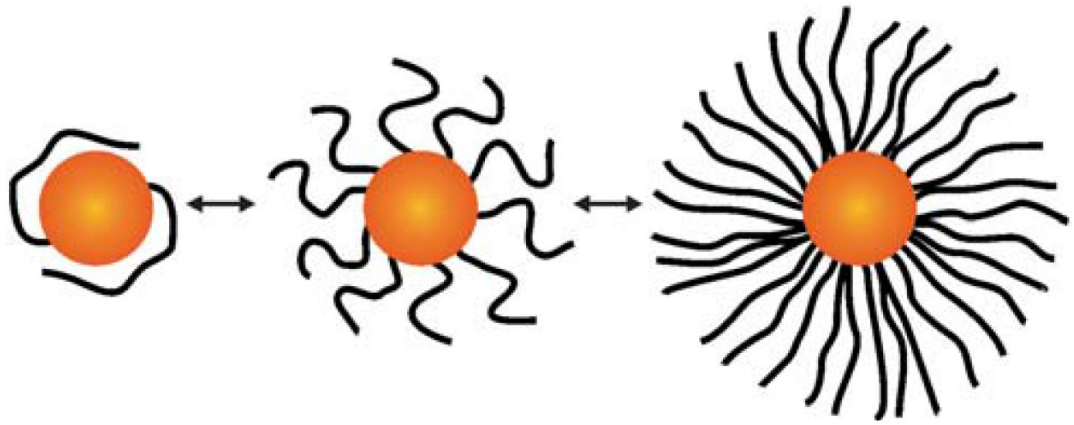

Figure 1.4. A cartoon showing different grafting densities of DNA on a colloid. Taken from ref. [41].

The third contribution is the Watson-Crick base pair interaction: ssDNA oligomers will attract their complementary strands to form hydrogen bonds between the bases - the DNA will hybridise. These interactions can be tuned by changing the length/specific sequence of the strand, as described above, making DNA act as a selective and reversible binding agent when attached to colloids. The hybridisation of DNA can be measured using UV absorption spectroscopy: at 260 nm wavelength ssDNA absorbs stronger than dsDNA. DNA grafted to colloids exhibits a much sharper hybridisation/melting transition than free DNA (Figure 1.5 a).

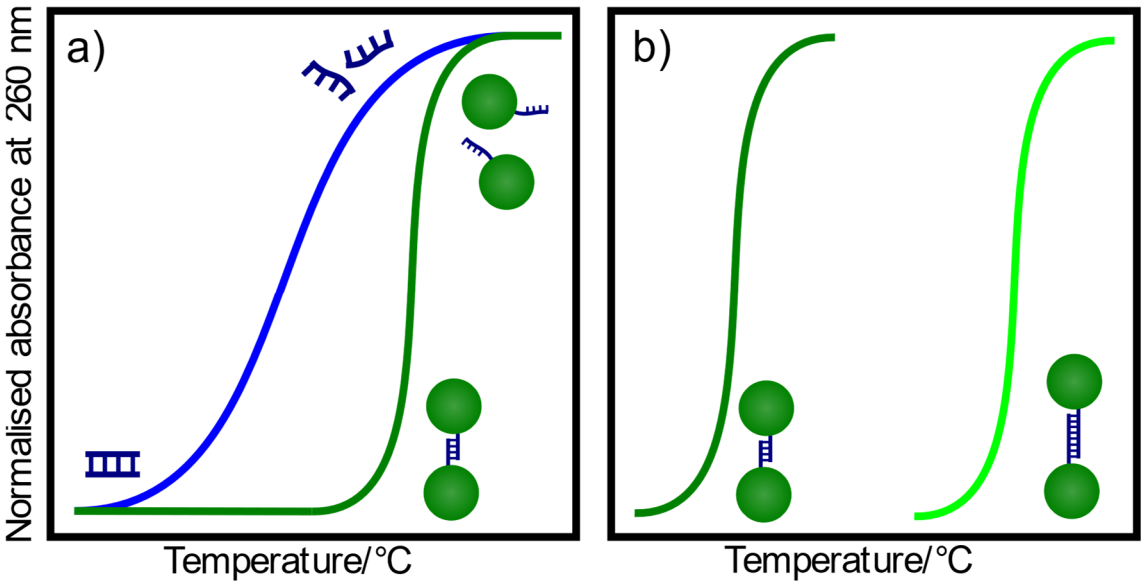

Figure 1.5. Schematic DNA melt curves. a) Melting of free strands vs DNA on colloids. b) Melting temperature change with increasing strand length.

This melting behaviour was explained by Geerts and Eiser [41] using simple probabilistic calculations. The statistical probability P_1 that a single strand is unbound at a temperature T is given by [41]:

$$P_1(T) = \frac{1}{1+e^{-\beta\Delta f(T)}}, \tag{1.9}$$

where $\beta = 1/k_\mathrm{B}T$ and $\Delta f(T)$ is the free energy of hybridisation. The melt curve is s-shaped and not sharp (blue curve in Figure 1.5 a): the temperature window over which hybridisation takes place is typically between 10 to 30 °C. However, if there are N strands connecting two colloidal particles, all strands must unbind for the colloids to unbind, and $P_N(T)$ changes to

$$P_N(T) = \left(\frac{1}{1+e^{-\beta\Delta f(T)}}\right)^N. \tag{1.10}$$

This assumes negligible DNA-DNA interactions and unique binding sites. For sufficiently high N the melt curve is almost a step function (green curve in Figure 1.5 a). Note that T_m also increases (logarithmic dependence on N) [41]. An increase in the number of binding base pairs per strand of grafted DNA also increases T_m (Figure 1.5 b). This shows that DNA-coated colloids (DNACCs) have a well-defined and tuneable melting temperature, a desired feature in programmable self-assembling systems.

1.2.3 DNA-coated Colloidal Gels

DNACCs first appeared in literature in 1987 with Wolf et al. [42], who functionalized hydrazide-coated particles with carboxyl-terminated DNA strands via the formation of a peptide bond. Work on aggregated DNACC systems was published in 1996, when Mirkin et al. [43] demonstrated temperature-reversible aggregation of DNA-coated gold nanoparticles. In the same year, Alivisatos et al. [44] assembled gold DNACCs into dimers and trimers – what they called 'nanocrystal molecules'.

It was later shown that DNACCs could form amorphous aggregates, short-ranged ordered phases or colloidal crystals, depending on the properties of the particles and the kinetics of assembly. Most studies on DNA-coated nanoparticles have focused on the formation of crystals or superlattices [45–47], however, for most micron-sized colloids only amorphous, fractal-like phases form, despite a crystalline phase being thermodynamically more favourable [48]. This is caused by the sharp melting behaviour of the DNA grafted to colloids and by the strength of the attractive forces between the oligomers. While nanoparticles can overcome these barriers as they diffuse more easily, microparticles become kinetically arrested in these metastable states [48, 49]. This kinetic arrest can be avoided by precisely controlling the temperature of the system and having a dense coating of DNA [50, 51]. Near the melt temperature, such particles can roll and rearrange, which allows them to reach the thermodynamically favourable crystalline phase.

Figure 1.6 shows a sketched phase diagram of attractive colloids. As Di Michele explains [48], the region where thermodynamically preferred phase separation is favoured is delineated by the binodal line, which identifies, at a given temperature, the equilibrium densities of the two phases. The spinodal line determines where the homogeneous phase becomes unstable: any density fluctuation in that region leads to spinodal decomposition. If the mixture is quenched from a high temperature to $T > T_g$, spinodal decomposition starts, resulting in a complete separation of the two equilibrium phases. However, if the quench is performed to a final state with $T < T_g$, spinodal decomposition begins, but the rearrangements slow down when the density of the aggregates reaches the glass line and the phase separation is interrupted. The structures, if the overall density of the mixture is high enough, can form a gel which is permanent over the experimental time window. A gel is defined as a material made of a continuous liquid phase surrounding a space-spanning network made of colloids or cross-linked polymers which exhibits no flow and is able to sustain mechanical stress [48, 52]. However, if the cooling is slow enough or

the nanoparticles used are small enough, crystallisation can occur in the region between the binodal and the spinodal lines.

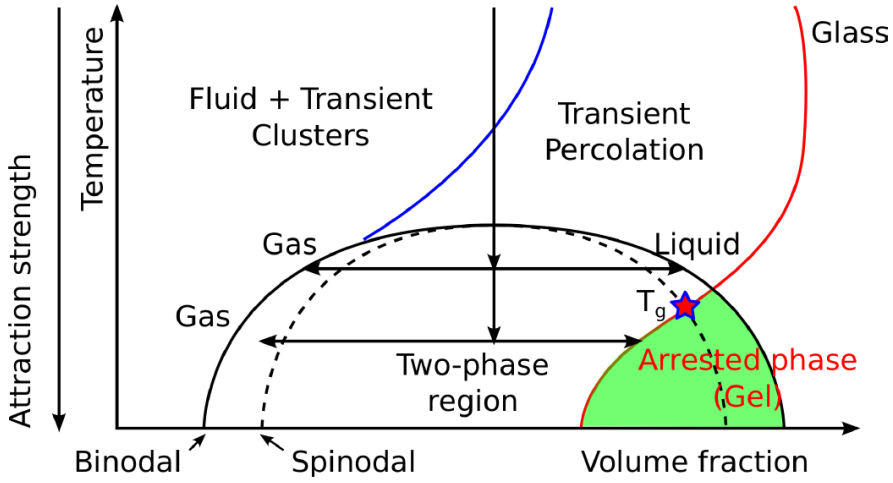

Figure 1.6. Sketched phase diagram of attractive colloids. Modified from ref. [48].

Our group demonstrated percolating colloidal gels made of DNACCs and later investigated a system made of two different sets of colloids (polystyrene beads, 0.5 micrometer in diameter, red and green fluorescent - R and G) which have attractive intra-species interactions and repulsive inter-species interactions [53, 54]. R colloids could only bind to other R colloids, while G could only bind to G (both species had the same T_m); R and G colloids were always repelled by electrostatic interactions under the experimental conditions used. This system was used to form two interpenetrating gels ('bigels') through arrested demixing and two-step aggregation. As such a sample is cooled from the gas state to below T_m, density fluctuations grow very rapidly due to the favourable colloidal interactions, similar to the case of spinodal decomposition in atomic systems, and phase separation begins. The colloids then become kinetically arrested due to selective DNA interactions and the two phases are compositionally pure as G-R interactions are repulsive [48]. Figure 1.7 c shows a typical confocal image of a demixed bigel with equal volume fractions of R and G colloids. Computational work indicates that a percolating gel forms above ~ 5% individual volume fraction of the colloidal phase [53]. Moreover, a bigel can sustain more strain than a gel at the same overall volume fractions [55].

Multistep aggregation can also form bigels: the DNA strands can be designed such that $T_{m,R} < T_{m,G}$; if a quench is performed to $T_{m,R} < T < T_{m,G}$, the G colloids aggregate

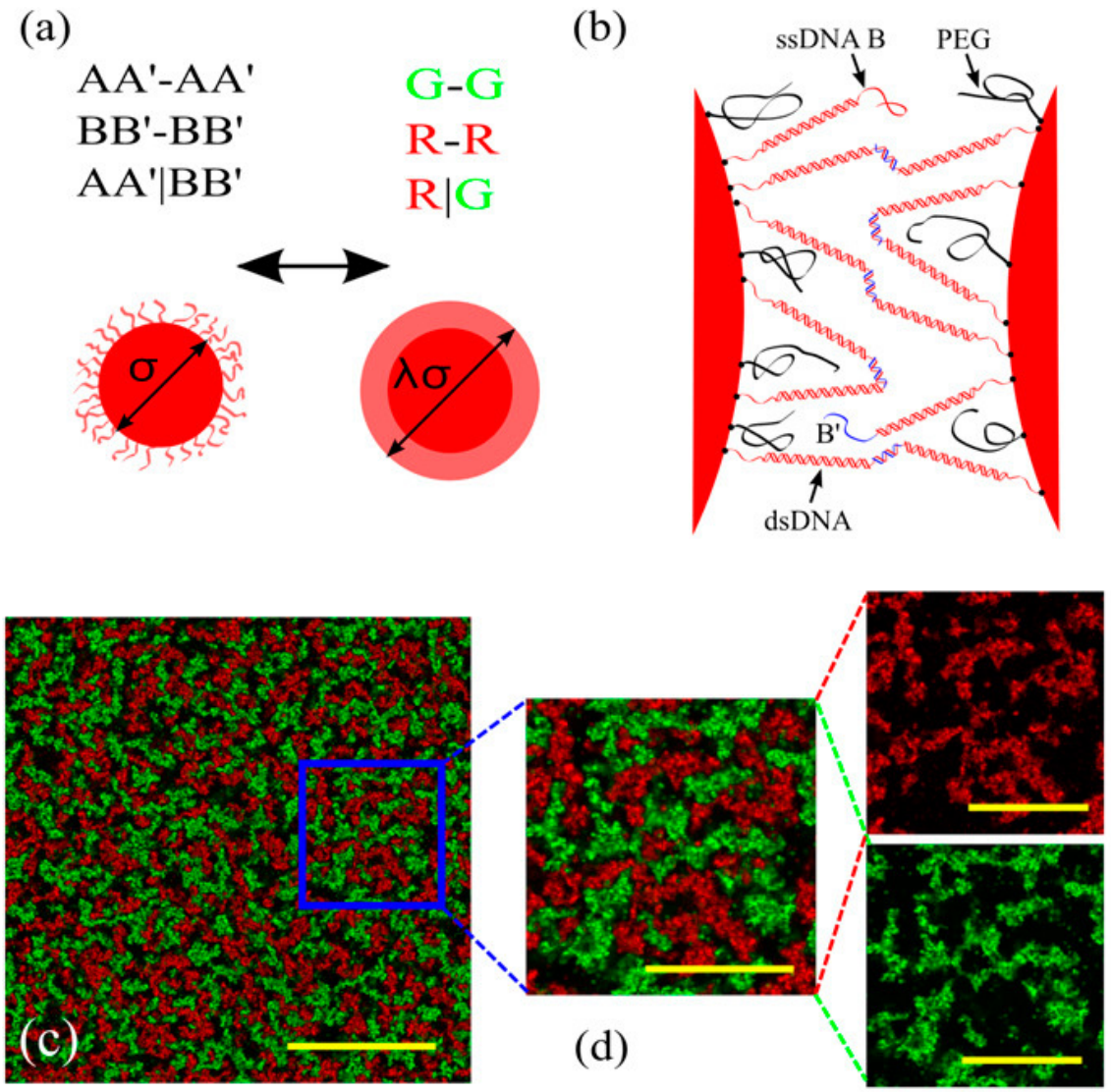

*Figure 1.7. Colloidal bigel system. (a) Interactions of the colloids in experiments (left, the DNA strand **A** is complementary to **A'**, **AA'** does not bind to BB') and the theoretical model (right). (b) A not-to-scale cartoon of two interacting R colloids. Red double helices indicate dsDNA spacers. (c) Confocal image of the demixed bigel, scale bar = 50 μm. (d) Zoomed in bigel, scale bar = 25 μm. Images taken from ref. [53].*

first while the R ones remain in the gaseous phase. Further cooling results in R colloids aggregating in the spaces left by the G gel. This sequential activation of forces allows to control the morphology of the bigel: after the G colloids aggregate, the R ones (R & G have the same volume fractions) only form discrete clusters rather than a percolating structure in some cases, depending on the volume fraction [56]. Another option is having a core-shell structure, where a gel of R colloids forms first (**AA'** DNA strands) and then the G colloids coat the R gel ($\mathbf{A_s}$ strands, complementary to a sub-sequence of **A'**) [57]. This could be used for triggered release in food and cosmetics applications, as the primary

gel could be made permanent and would act as a template surface for the coating that is thermally- or pH-activated. Furthermore, having the template transparent would provide better imaging possibilities.

1.3 Dissertation Outline and Aims

In this chapter I have presented background information on forces that govern the behaviour of colloids and how modifying the surfaces of colloidal particles, e.g., by grafting DNA to them, changes their interaction potentials. DNA in this case acts primarily as thermally-reversible 'intelligent glue': DNA coated colloids (DNACCs) selectively bind to other DNACCs only below a certain temperature.

The overarching aim of this dissertation is to explore the self-assembly of DNACCs into a variety of structures, exploiting their highly specific, tuneable and thermally reversible binding. The first goal is to create monodisperse colloidal particles and surface-functionalise them with DNA, thus creating our 'building blocks'. This is done in Chapter 3 that focuses on the synthesis of polystyrene and poly(heptafluorobutyl methacrylate) colloids through emulsion and dispersion polymerisation. The particles are subsequently functionalised by coating them with azide end-functionalised block copolymers and grafting DNA onto them via a click reaction.

In industrial formulations, colloidal particles often exist in a gelled or jammed state, often at significantly large volume fractions (> 5%). When creating model systems to explore the morphology of such structures, multiple-light scattering hindering the imaging of gel morphology can become an issue, especially if the system requires an aqueous continuous phase, e.g., when investigating bacterial transport through said structure. Chapter 4 solves the problem by using fluorinated particles developed in Chapter 3 as they have a low refractive index (n = 1.36) and therefore can be refractive index-matched in aqueous solutions. By appropriately designing the DNA coatings, the particles are made to undergo two-step self-assembly, with the 'core' gel structure forming first and a 'coating' condensing onto it, thus creating a core-shell bigel. Fluorescence optical microscopy imaging is used to extract morphological information employing structural analysis. Spatially homogeneous gels are achieved by using polystyrene particles as the 'scaffold' onto which the fluorinated colloids condense. Additionally, diffusion of tracer particles in the confinement of the gel structure is investigated using differential dynamic microscopy, showcasing the possibility of tracking a moving particle deep in the gel structure.

Many foods, cosmetics and pharmaceuticals frequently contain oil-in-water emulsions in their formulations. The goal of Chapter 5 is to create 'reconfigurable' fluids by coating oil droplets (ODs) with DNA, effectively turning them into functional 'soft colloids'. Ultrasonication, microfluidics and membrane emulsification are employed to produce ODs of different sizes and different oils, along with evaluating their stability over time using dynamic light scattering and optical microscopy. Three new systems are investigated: hierarchical 'raspberry' ODs made of sub-micron diameter ODs attached to large ODs via DNA; a thermally reversible gel of sub-micron ODs; and ODs grafted to a flat surface via DNA that can exhibit controlled release. All of this is achieved using the same coating principle – utilising azide end-functionalised block copolymers and 'clicking' DNA onto them. Moreover, using inexpensive Synperonic triblock copolymers allows us to scale up the protocol, making this an attractive system for industrial advances and applications.

Colloidal self-assembly is also used to form photonically active materials – if the features of the microstructure are comparable to the wavelength of the incoming light, the material can exhibit structural colour. 'Uncoated' 200 nm diameter fluorinated latex particles, used in the abovementioned chapters, due to their strong surface charge and low refractive index, are found form photonic crystals at concentrations of 20% v/v and above. Rather than showing iridescence, these materials display strong single colour reflectance along with high transmission, with the reflection colour varying with the particle concentration and thus the interparticle distance. Small-angle X-ray scattering measurements reveal close-packed structures and electromagnetic simulations confirm the strong dependence of colour on the lattice parameter.

Coming back to DNACCs, which are the main topic of this dissertation, Chapter 7 describes additional work on DNACCs self-assembly done in collaboration with others. The first part aims to explore how shape anisotropy changes the self-assembly of such colloids. Rod-sphere structures made from DNA-coated gold nanoparticles and fd viruses are investigated. While spherical systems, such as the ones explored in Chapter 4, display one characteristic length-scale, this rod-sphere system is found to exhibit two, indicating that the shape and stiffness of the fd viruses influence the overall gel structure of the system. The second part investigates magnetic field-assisted self-assembly of superparamagnetic DNACCs.

2 EXPERIMENTAL MATERIALS AND METHODS

2.1 Colloid Synthesis

The majority of our group's experiments on DNA-coated colloids had previously been done using commercially sourced particles. This had several drawbacks, mainly the cost and the inability to fine-tune the particles to our preferences. This dissertation mainly focuses on in-house produced polymeric colloids, allowing for control of many parameters, such as size, surface functional groups, DNA grafting densities and particle volume fraction.

2.1.1 Fluorinated Latex Particle Synthesis

Fluorinated latex (FL) colloids were typically synthesised via an emulsion polymerisation mechanism. 124 ml of deionised water was poured into a 250 ml round-bottom flask. 3.25 g (12 mmol) 2,2,3,3,4,4,4-heptafluorobutyl methacrylate (HFBMA, 97%, purchased from Alfa Aesar) was added together with 125 mg (0.43 mmol) sodium dodecyl sulphate (SDS, from Sigma-Aldrich) into a 250 ml round-bottom flask. The mixture was emulsified with a magnetic stirrer (600 rpm) under N_2 atmosphere for 1 hour. 68 mg (0.25 mmol) potassium persulfate (KPS, Sigma-Aldrich) was dissolved in 1 ml deionised water and added to the emulsified mixture. The KPS acted both as an initiator of the polymerisation and as stabilising surface groups of the final colloids. While being stirred at 800 rpm, the mixture was heated to 70 °C to initiate the polymerisation. After 12 h, the resulting colloidal dispersion of ~200 nm diameter particles was purified by dialysis and then kept refrigerated. Washing by centrifugation was not feasible as the unwashed FL colloids tended to aggregate at high spinning rates.

2.1.2 Polystyrene Particle Synthesis

Typically, 61.8 mg (0.30 mmol) (SVBS, Sigma-Aldrich) and 405 mg (1.50 mmol) KPS were added to 300 ml deionised water in a 500 ml round-bottom flask. The mixture was degassed and purged with nitrogen five times. Then it was heated to 70 °C while

vigorously stirred (> 1,000 rpm) with a magnetic stirrer. 15.6 g (150 mmol) of styrene (Sigma-Aldrich) was injected immediately afterwards. The reaction was quenched on ice after 24 h of polymerisation. The resulting ~200 nm diameter polystyrene (PS) particles were washed using deionised water by repeated centrifugation and kept refrigerated.

2.2 Particle Surface Functionalisation

One of the main challenges of particle surface modification is stability against aggregation. As this dissertation focuses on DNACCs, the additional charge from the DNA double helix has to be considered. As most of our colloidal particles had negatively charged surfaces, incremental salting was one option – this way the Debye screening length of the colloids was reduced and DNA could come closer to their surface. However, the salting had to be precisely controlled as the particles could then aggregate during the coating procedure. A different approach was chosen in the end, one based on a swelling-deswelling method developed by Suk Oh et al. [50]: the particles were first coated with a dense azide end-functionalised polyethylene glycol (PEG-N_3) brush and DNA was then attached to the azides on the free PEG-N_3 ends. The polymer layer provides steric stability without and takes the reaction between the DNA and the PEG functional ends away from the surface, thus reducing the amount of necessary salting.

2.2.1 Polymer Particle PEGylation

2.2.1.1 Diblock Copolymer End-functionalisation with N_3

Polystyrene-b-poly(ethylene glycol) diblock copolymer (PS-b-PEG, M_w(PS) = 1,300 g/mol, M_w(PEG) = 5,600 g/mol; purchased from Polymer Source) was typically first end-functionalised with N_3 groups as follows. 100 mg (0.015 mmol) of the diblock copolymer was dissolved in 2 ml dichloromethane (DCM, ≥ 99.8%; Sigma-Aldrich) in a 25 ml round-bottom flask. 42 µl (0.3 mmol) of triethylamine (TEA, ≥ 99.5%; Sigma-Aldrich) was then added to the solution. The flask was then cooled to 0 °C in an ice bath and 23.5 µl (0.3 mmol) of methanesulfonyl chloride (mesyl chloride - MsCl, ≥99.7%; Sigma-Aldrich) was then injected and the reaction continued overnight, while the temperature slowly increased to room temperature (Figure 2.1). Afterwards the solvent was evaporated in a rotary evaporator and the precipitate (PS-b-PEG-Ms) was dissolved in 2 ml methanol (MeOH) containing 3% HCl [50, 57]. The polymer was precipitated by adding 30 ml of diethyl ether (Sigma-Aldrich) and keeping the solution at -18 °C for 30 min. The precipitate was separated from the solvent by centrifugation. The washing was

repeated once more with MeOH and HCl, and 3 times with MeOH. The polymer was then dried under vacuum.

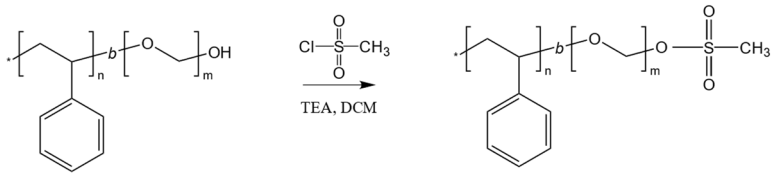

Figure 2.1. PS-b-PEG mesylation reaction scheme.

The mesylated dry polymer was then dissolved in 2 ml dimethyl formamide (DMF, Sigma-Aldrich) containing 10 mg (0.15 mmol) NaN_3 in a 25 ml round-bottom flask. The solution was stirred at 1,000 rpm at 70 °C for 24 h (Figure 2.2). The solvent was then evaporated as before and the washing with MeOH and ether was done 4 times. The PS-b-PEG-N_3 was then dried and kept frozen.

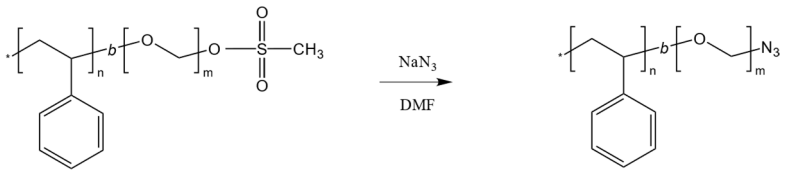

Figure 2.2. PS-b-PEG-Ms azide functionalisation reaction scheme.

2.2.1.2 Particle PEGylation via Swelling

Typically, 100 µl of 5% v/v 200 nm diameter PS particles were mixed with 100 µl deionised water containing 1 mg of PS-b-PEG-N3. 200 µl tetrahydrofuran (THF, Sigma-Aldrich) was added to swell the polymer particles, and the mixture was vigorously shaken for 30 min. In the case of fluorescent particles, 1 µl (1 mg/ml in THF) BODIPY fluorescent dye (ThermoFisher) was added to the THF prior to swelling. An excess of water was then added to the mixture to reduce the overall volume fraction of THF to below 10% and thus de-swell the particles. The mixture was heated to 60 °C for 30 min to evaporate the THF. The now-PEGylated colloidal particles were washed by centrifugation 3 to 5 times, suspended at the desired concentration and kept refrigerated.

The procedure was the same for FL particles, with a minor difference being the amount of THF added to swell them: it was 100 µl THF to 200 µl particles, making the overall THF v/v concentration 33% rather than 50%, so as to avoid FL particle dissolution.

2.2.2 DNA-coupling to PEGylated Particles Using a Strain-Promoted Alkyne-Azide Cycloaddition

The DNA sequences used in this dissertation were purchased from Integrated DNA Technologies: amine-5'-TTT TTT TTT TTT TTT GGT GCT GCG-3' (called **A**), amine-5'-TTT TTT TTT TTT TTT CGC AGC ACC-3' (**A'**: sticky end complementary to **A**), amine-5'-TTT TTT TTT TTT TTT ATC TAT CGT A-3' (**B**), and the complementary amine-5'-TTT TTT TTT TTT TTT TAC GAT AGA T-3' (**B'**).

It is important to note that single strands have directionality given by the phosphate group (5') being on one end and the sugar group (3') on the other. To form double stranded DNA, for a given sequence of bases, a complementary strand needs to have an appropriate sequence of bases, allowing for A-T and C-G bonds, and its backbone has to be antiparallel. In this dissertation, complementary DNA sequences are presented with the 5' and 3' ends on the same sides, starting with the reactive side (amine) and ending with the 'sticky' side. However, to better visualise how they would hybridise, the reader can write down the 'sticky' end of the complementary strand backwards. As an example, the 'sticky' end of **A** is 5'-GGT GCT GCG-3', whereas if we now start from 3', the 'sticky' end of **A'** is 3'-CCA CGA CGC-5'. Reading both of them from left to right, it is now clear that GGT is complementary to CCA and so on (note: the bases are grouped into groups of three for ease of presentation).

The stock DNA was dissolved in 10 mM phosphate buffer (PB, Sigma-Aldrich) at 1 mM concentration and kept frozen. Typically, 50 µl stock NH_2-DNA was mixed with 50 µl PB containing 200 mM NaCl, and 12 µl dimethyl sulfoxide (DMSO, Sigma-Aldrich), containing 25 mM dibenzocyclooctyne-sulfo-N-hydroxysuccinimidyl ester (DBCO-sulfo-NHS, Sigma-Aldrich) and reacted for 24 h with gentle shaking (Figure 2.3). The DBCO-DNA was purified using Illustra NAP-5 columns (GE), resulting in 1 ml 50 nM DBCO-DNA solution in PB. The DBCO-DNA was either immediately used or kept frozen.

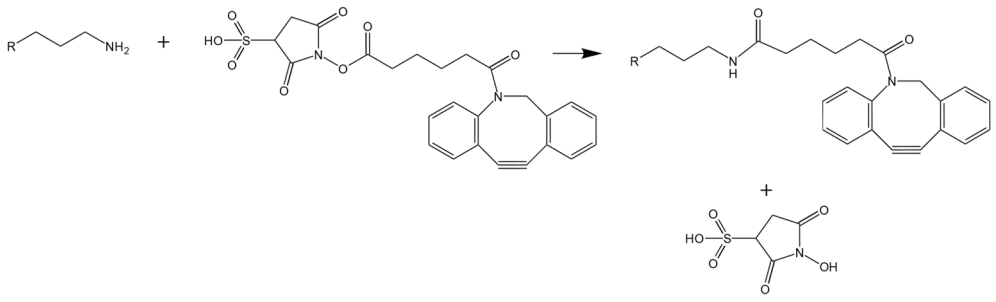

Figure 2.3. Aminated DNA reacts with DBCO-sulfo-NHS ester. R is the DNA.

Nominally 25 µl 5% v/v 200 nm diameter PEGylated particles were mixed with 475 µl PB and 500 µl 50 nM DBCO-DNA and reacted in a thermal shaker at 65 °C for 24 h. The DBCO would react with the N_3 groups on the PEGylated particles via a strain-promoted alkyne–azide cycloaddition (SPAAC, Figure 2.4). Incremental addition of NaCl solution in PB was done in some cases to increase the density of DNA oligomers on the particle surface: the overall NaCl concentration was increased by 100 mM every 4-6 h until it reached 300 mM.

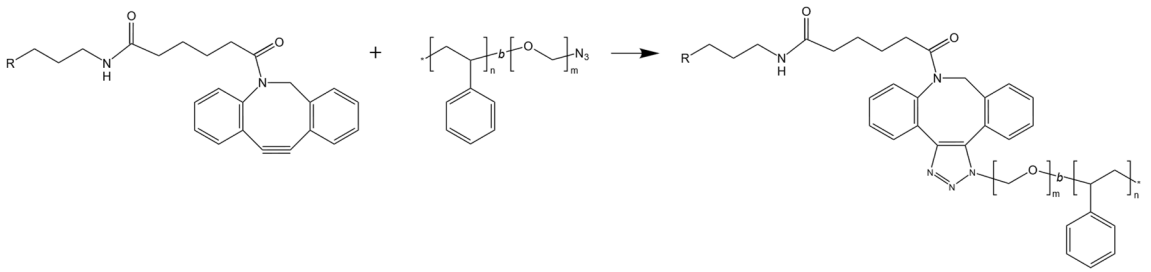

Figure 2.4. SPAAC mechanism between DBCO-DNA and PS-b-PEG-N_3.

The DNACCs were then washed by centrifugation, suspended in the desired buffer at the desired concentration and kept refrigerated.

2.3 Functional Oil Droplet Manufacture

A significant part of this thesis was spent on developing protocols for making azide-functionalised oil droplets (ODs) dispersed in aqueous solutions. DNA-functionalised ODs have a variety of experimental applications as soft colloids with mobile linkers on the surface.

2.3.1 Functional Surfactants

Synperonic F108 and F127 non-ionic surfactants were purchased from Sigma-Aldrich. Polystyrene-b-poly(ethylene glycol)-N_3 diblock copolymers (PS_{30}-b-PEG_{79}-N_3 and FL_{14}-PEG_{79}-N_3) were synthesised by our collaborators Dr Clément Mugemana and Prof Nico Bruns at the Adolphe Merkle Institute in Fribourg, Switzerland.

The Synperonic triblock copolymers were functionalised with azide groups using the same protocol as described in section 2.2.1.1, with some reactions using p-toluenesulfonyl chloride (tosyl chloride – TsCl, ≥99.0%; Sigma-Aldrich) instead of MsCl.

2.3.2 Microfluidics

2.3.2.1 Device Fabrication

Microfluidic channels with a height of 25 µm were fabricated in polydimethylsiloxane (PDMS; Dow Corning), using SU-8 permanent epoxy on silicon masters: a silicon wafer was spin-coated with 3-4 ml of SU-8 3025. The wafer was then 'soft baked' for 15 min at 100 °C. The photoresistant master (15 µm width channels) was applied to the wafer, cured with UV light for 30 s; the mask was baked again for 5 minutes at 100 °C ('post-exposure baking'). The photoresistant cover was removed and the non-cured parts of the epoxy were washed away using propylene glycol monomethyl ether acetate (PGMEA, Sigma-Aldrich). PDMS was combined with its curing agent and applied to the mask in a Petri dish. The dish was desiccated to remove any air trapped inside the PDMS. The devices were then 'baked' at 100 °C for 2 h, cut out and peeled off the wafer. Holes were punched for channel access and the devices were plasma bonded to glass slides to create sealed devices. Formed PDMS devices were then plasma treated for 500 seconds (DienerFemto) forming a hydrophilic surface coating. The channels were immediately filled with water to ensure they remained hydrophilic for the duration of the experimental procedure.

2.3.2.2 Droplet Formation

The oil phase (hexadecane (Sigma-Aldrich) or PDMS oil (silicone oil, 50 cSt, Sigma-Aldrich)) was flowed through the microfluidic device at 50 µl/h. The aqueous phase (deionised water containing 2% w/w functional surfactant of choice) was flowed at 250 µl/h. The formed droplets were kept at room temperature.

2.3.3 Membrane Emulsification

The emulsions were obtained by a membrane technique using a LDC-1 Dispersion Cell (Micropore Technologies Ltd, Loughborough, UK). 5 ml of the dispersed phase (either hexadecane or silicone oil) was injected through the membrane (20 µm pore size, 80 µm intra-pore distance) into 50 ml of deionised water containing 2% w/v PS-PEG-N_3 or F108-N_3 by means of a syringe pump (model Aladdin 1000, WPI, Sarasota, USA) with a flow rate of 0.5 ml/min. The agitator was driven by a 24V DC motor and the paddle rotation speed was set to 19.066 Hz (1144 rpm), corresponding to an applied voltage of 10 V. The emulsions were kept at room temperature.

2.3.4 Ultrasonic Emulsification

Typically, 1600 µl F108-N_3 (or PS-PEG-N_3) at 2% w/v in deionised water was mixed with 200 µl hexadecane and 200 µl deionised water in a glass vial. The mixture was prevortexed and ultrasonicated with a probe (Bandelin Sonopuls HD 2200) at 20% amplitude for 10 min in pulsed mode (0.5 s on, 0.5 s off). The resulting droplets were kept at room temperature.

2.3.5 DNA Coating

Generally, the azide-functionalised droplets were washed 4-5 times with 0.5% w/w Synperonic F108 dissolved in PB. For sub-micron sized drops, 100 µl of drops at 70% v/v were mixed with 25 nanomoles of DBCO-DNA in a total volume of 1 ml PB containing 0.5% w/w F108. The mixture was gently shaken at room temperature for 24 h, while raising the NaCl concentration to 100 mM incrementally over the first 6 h. The droplets were then washed 5 times with 0.5% w/w F108 in PB and kept at room temperature. For larger (5 µm and up) droplets, 10 times less DNA was used for the same volume of droplets.

2.4 Microscopy and Characterisation

2.4.1 Dynamic Light Scattering and Zeta-potential Measurement

By measuring the diffusivity and electrophoretic mobility of colloids, modern dynamic light scattering (DLS) instruments provide a simple way of obtaining the hydrodynamic diameter and zeta-potential of particles. In a typical DLS apparatus, a narrow, collimated laser beam is passed through the colloid sample and the resulting scattering pattern is measured by a point detector at a given scattering angle. The second order autocorrelation function then compares the scattering intensity $I(q,t)$ to itself after a time τ:

$$g^{(2)}(\tau) = \frac{\langle I(t)I(t+\tau)\rangle}{\langle I(t)\rangle^2}. \quad (2.1)$$

The intensity-autocorrelation function decorrelates exponentially with increasing τ, assuming a monodisperse dilute colloidal suspension. The diffusivity of the colloids is then calculated from the rate of the decay of $g^{(2)}(\tau)$. That in turn is related to the average apparent hydrodynamic radius of the colloidal particles in the suspension via the Stokes-Einstein equation.

A key indicator of the stability of a colloidal suspension is the zeta-potential, ζ [17]. It is defined as the electric potential at the no-slip plane, i.e., it is the potential difference between the dispersion medium and the tightly-bound stationary layer of liquid attached to the colloid (Figure 2.5). In a DLS-zeta apparatus, the zeta-potential of a colloidal suspension is obtained by measuring the particles' velocity v in an AC electric field E. v is extracted from the Doppler shift between two interfering laser beams due to the colloidal motion in the applied electric field. Assuming a small Debye screening length, the electrophoretic mobility of the colloids is related to the zeta-potential via the Smoluchowski equation [58]:

$$\mu_e = \frac{v}{E} = \frac{\varepsilon_r \epsilon_0 \zeta}{\eta}, \tag{2.2}$$

where μ_e is the electrophoretic mobility, ε_r is the dielectric constant of the dispersion medium, ϵ_0 is the electric permittivity of free space and η is the viscosity of the medium.

In this thesis, model Z and model ZSP Zetasizer machines from Malvern were used to measure zeta-potentials and sizes of various colloidal particles.

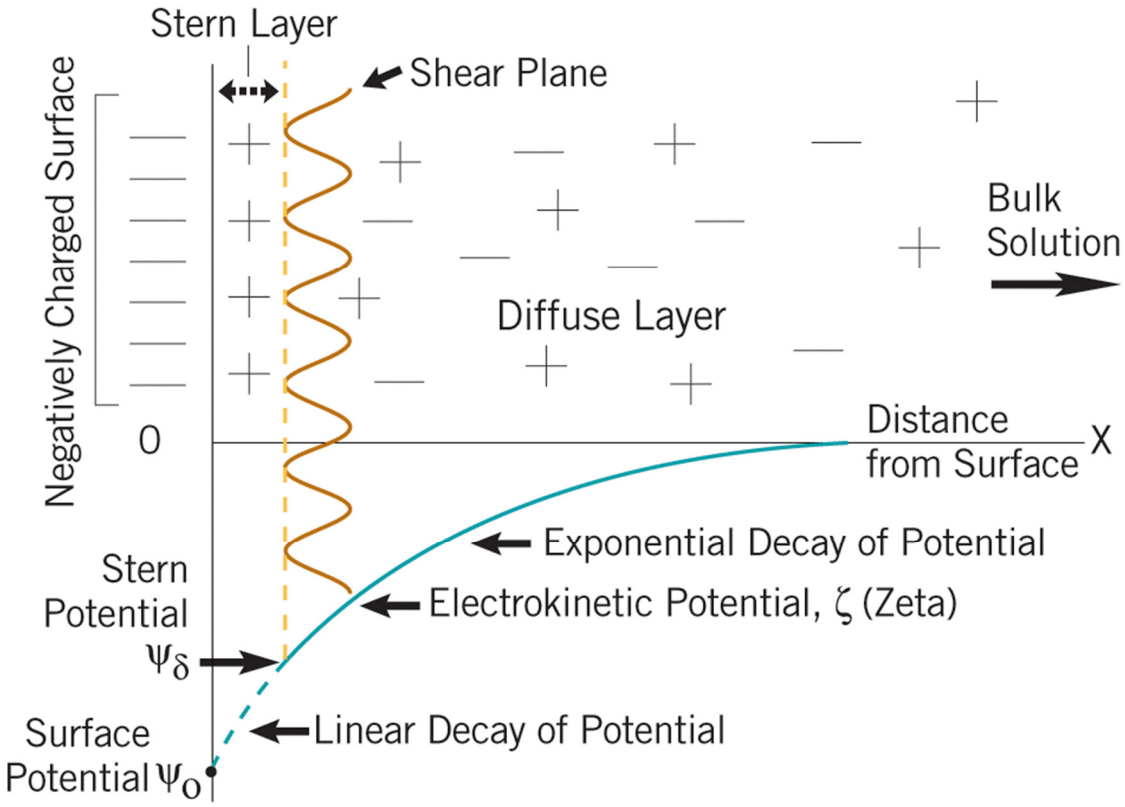

Figure 2.5. Sketch of the zeta-potential. Taken from ref. [17].

2.4.2 Small-angle X-ray Scattering

Small-angle X-ray scattering (SAXS) is a small-angle scattering technique by which nanoscale density differences in a sample can be quantified. In a typical SAXS setup, a monochromatic beam of X-rays is brought to a sample from which some of the X-rays scatter, with most of them simply going through it without interaction. The scattered X-rays form a scattering pattern detected at a detector situated behind the sample perpendicular to the direction of the initial beam.

SAXS measurements were carried out at the ID2 Beamline of the European Synchrotron Radiation Facility (ESRF) in Grenoble, France and at the B21 station of the Diamond light source, UK. The 2D spectra measured at the ESRF were obtained using X-rays with a wavelength of 0.1 nm and a beam size of 50 μm × 20 μm on the sample. The sample to detector distance was 10 m and the detector used was a Rayonix MX170. The setup at Diamond used the same wavelength X-rays but a beam size of 1 mm × 1 mm, a sample to detector distance of 4 m and a Pilatus 300 K detector. All spectra were normalised against the background and an empty cell.

2.4.3 UV-Vis and Fourier Transform Infrared Spectroscopy

The absorption properties of DNA free in solution was measured using two different ultraviolet-visible (UV-Vis) light spectrometers (Cary 300 Bio, Agilent Technologies). Since ssDNA has a 37% higher extinction coefficient than dsDNA at 260 nm, the relative amounts can be measured using UV-Vis spectroscopy, producing the classic s-shaped 'melt curves' of absorption vs temperature [59]. Typically, ssDNA and its complementary strand (**A** and **A'**, **B** and **B'**) were used in equimolar ratio in PB at various salinities in quartz cuvettes.

To quantify the concentration of dissolved DNA, a different spectrophotometer was used (Nanodrop 2000 UV-Vis, ThermoScientific). It provided several advantages over the Cary 300 Bio, namely the speed of data acquisition (minutes) and low sample volumes (1-2 μl). Typically, a 2 μl drop of a known DNA sequence dissolved in PB was measured for absorbance at 260 nm and the DNA concentration was then calculated from the extinction coefficient of that particular strand.

Fourier transform infrared spectroscopy (FTIR) is a technique used to collect an infrared spectrum of absorption or emission of a sample with different sampling methods depending on the sample measured (transmission, attenuated total reflectance (ATR) and

grazing angle) [60]. ATR-FTIR (Cary 600 series, Agilent Technologies; Figure 2.6) was used in this dissertation to measure the FTIR spectra (absorbance vs wavelength) of our di- and triblock copolymers (powder) and colloidal particles (powder) to check for end and surface functionality, respectively.

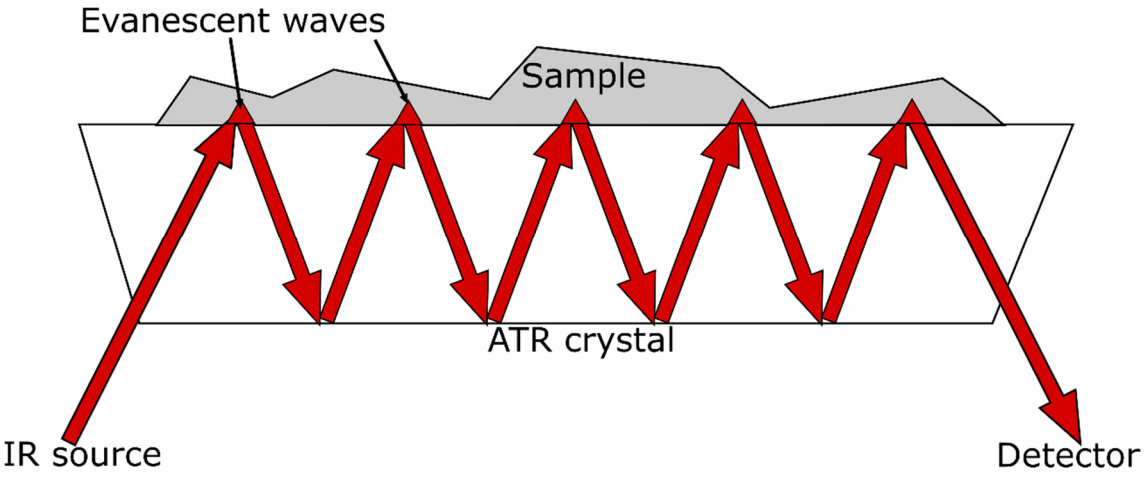

Figure 2.6. Cartoon depicting a typical ATR-FTIR setup.

2.4.4 Reflectivity Measurements

The reflection measurements were taken using a reflection probe bundle equipped with different LED light sources and a spectrometer. Illumination and collection were done at normal angle. The green and red angles were illuminated with a fibre-coupled white LED (Thorlabs MCWHF2) and the blue sample was illuminated with a cyan LED emitting at 490 nm (Thorlabs M490F3). The spectra were measured using a Thorlabs CCS 100 spectrometer. Reference measurements were taken using a Thorlabs BB1-E02 dielectric mirror.

2.4.5 Fluorescence-based Assays

Fluorescence-based assays are a powerful tool in quantifying the surface density of functional groups on colloidal particles [50, 61]. Fluorescent probes with functional ends are reacted to a species on the surface of colloids in a suspension, the particles are sedimented by centrifugation and the fluorescence of the supernatant is measured.

As the majority of our functional particles had azide groups on the surface, a good choice for the fluorescent probe was dibenzocyclooctyne-Cy5 (DBCO-Cy5, SigmaAldrich), as the DBCO end of the dye would react with the azides on the colloids in the same way as DBCO-DNA. Typically, 2.5 µl of 5% v/v 200 nm diameter PEGylated particles were reacted with 1 nanomole of DBCO-Cy5 in a total volume of 1 ml of Tris-EDTA buffer

(TE, pH = 8.0; SigmaAldrich) at 65 °C overnight (24 h) in thermal shakers. The particles were then sedimented and 100 µl of the supernatant was added to 900 µl TE in a plastic cuvette. The fluorescence emission intensity (650 nm excitation, 666 nm emission) of the supernatant sample was then measured in a fluorimeter (Cary Eclipse, Agilent Technologies) and compared to the fluorescence of a series of samples with known concentrations of the dye ('the standard') in TE.

In the case of DNA coverage assays, DNA-coated particles were reacted to complementary DNA end-functionalised with a Cy5 fluorophore in TE buffer and the fluorescence was quantified as described above.

2.4.6 Scanning and Transmission Electron Microscopy

The electron microscope used in this work was an S-5500 from Hitachi. Both scanning and transmission electron microscopy (SEM and TEM) were done on colloidal particles. In SEM, the electron beam is rastered across the sample, whereas in TEM it illuminates the whole sample at once. Detectors collect electrons (scattered by, transmitted through or emitted by the sample) at various heights below and above the sample. Electron microscopy offers higher resolution than conventional optical microscopy, however, it is slower and requires specific sample preparation.

2.4.7 Optical Microscopy

Optical microscopy is a powerful and versatile tool in many fields. Different optical components (lenses, apertures, filters, light sources) are used for a variety of applications.

The resolution of conventional optical microscopy is governed by the Abbe diffraction limit (~ 200 nm in the *x*-*y* plane, and ~ 500 nm in the *z*-direction) [62]. In this work, brightfield, epifluorescence and scanning laser confocal microscopy techniques were used to image individual colloidal particles (> 200 nm diameter), colloidal gels and oil droplets.

Brightfield and epifluorescence imaging was done using a Nikon Ti Eclipse inverted microscope equipped with a CMOS sensor CCD camera (Point Grey Grasshopper3, model GS3-U3-23S6M-C, equipped with a Sony IMX174 sensor). A list of objectives (mainly Nikon Plan Fluor E 40x NA 0.75, 40x Plan Apo Lambda NA 0.95, Nikon Plan Apo 60x NA 1.20 water immersion) and filters (TXRED, GFP) were used. For colloidal gels and ODs, where temperature control was necessary, a custom-made Peltier block with a PID controller were used; XML scripts automated the control and imaging.

Leica TCS SP5 equipped with a 63x NA 1.2 oil immersion objective was used for confocal microscopy with the appropriate lasers and filters for different fluorescent dyes. A confocal microscope introduces a pinhole aperture in the beam path of the emitted light so that out of focus light can be filtered out, which decreases noise in the *z*-direction. For colloidal gel experiments, a laser would 'scan' the sample in the x-y plane, forming a 2-D image. The sample was then moved in the *z*-direction to collect a stack of sequential 2-D images.

2.5 Image Analysis

2.5.1 Chord Analysis

Chord analysis is a tool to characterise length-scale distributions of biphasic or multiphasic systems, first proposed in 1968 [63]. In later work, P. Levitz and D. Tchoubar expanded on this technique and how its results could be interpreted for different media [64]. The chord distribution for a particular phase, for instance, observed in a confocal microscopy image, describes the probability of having that phase at a certain thickness in some arbitrary direction.

Confocal microscopy images of colloidal gels were analysed using a custom Mathematica programme that took raw image files (Figure 2.7 a). First, the images were processed using a Gaussian blur (Mathematica in-built function, blurred to the microscopy resolution limit) to remove the noise. Then the blurred images were binarized using Otsu's algorithm [64]. The resulting images had regions containing the colloidal gel (Figure 2.7 b, white) and regions representing the colloid free aqueous solution (Figure 2.7 b), black). Chord distributions were obtained by drawing straight lines (exaggerated line shown in Figure 2.7 b) with a thickness of one pixel through the binarized images both vertically and horizontally; this was sufficient assuming the sample was isotropic. The lengths r of the chords passing through either gel or the fluid phase were measured and plotted in a semi-logarithmic histogram of the normalised frequencies $f(r)$ with which the given lengths appeared (Figure 2.7 c). As the distributions appeared linear on a log-linear scale, they were fitted with exponential functions $f(r) \sim \exp\left\{-\frac{r}{\lambda_{\text{phase}}}\right\}$, where λ_{phase} was the e-folding length of the corresponding distribution. For the colloid-rich phase, $\lambda_{\text{colloids}}$ is a good measure of the persistence length of the material [65]. Both $\lambda_{\text{colloids}}$ and λ_{pores} were considered to be the characteristic length-scales of the phases in the colloidal gel.

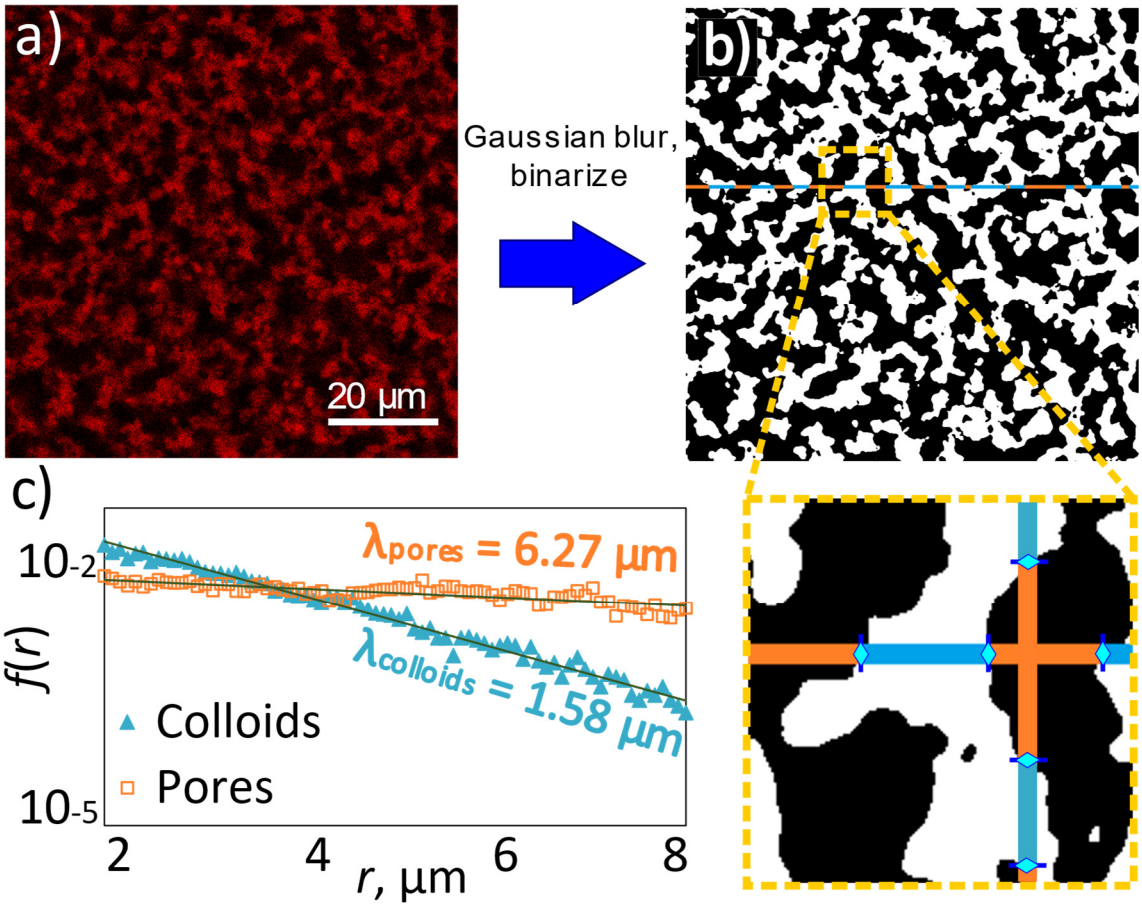

Figure 2.7. Cartoon explaining chord analysis. a) Raw image of a colloidal gel (red = colloidal phase, black = fluid phase). b) The same image after applying a Gaussian blur and binarizing. c) Normalised chord probability distribution f(r) vs chord length r (log-linear plot) with their exponential fits (solid lines) obtained from image b).

2.5.2 Structure Factor Analysis

In order to monitor the evolution and structure of a biphasic system, one can use structure factor analysis of microscopy images. For a colloidal concentration $c(x,y)$, the structure factor is given by

$$S(q) = \frac{\langle|\tilde{C}(q_x,q_y|^2\rangle}{|f(q)|^2}, \tag{2.3}$$

where $\tilde{C}$ denotes the 2D Fourier transform of $c(x,y)$, and $\langle \dots \rangle$ denotes the radial average. The form factor $f(q)$ is the Fourier transform of the shape of a single colloid. It was assumed that $c(x,y)$ was proportional to $i(x,y)$, the intensity of the image. Therefore, $S(q)$ could be measured in arbitrary units, when $\tilde{C}$ was replaced with $\tilde{I}$. The form factor $f(q)$ was estimated by taking the Fourier transform of the epifluorescence

microscopy image of the sample in the gaseous phase such that the structure factor could be expressed as

$$S(q) = \frac{\langle |\tilde{I}(q_x,q_y,t|^2 \rangle}{|f(q),t=0|^2}. \quad (2.4)$$

This was done in MATLAB with a custom script written by S. H. Nathan and R. R. Unwin, modified by the present author.

2.5.3 Differential Dynamic Microscopy

Differential dynamic microscopy (DDM) is a method of extracting dynamic information from a sequential series of optical microscope images [10]. It has several advantages over DLS, mainly that it works with denser samples [66], a broader range of particle sizes (even below the diffraction limit) [67, 68], is able to access a wider range of the scattering wavevector's q values [69] and requires no specialised equipment other than a microscope with a camera and a computer.

In DDM, bright field or fluorescence microscopy images separated by a given time lag are subtracted such that only the dynamic information due to colloid motion remains (assuming a constant illumination and no drift, Figure 2.8). Fourier transforming these difference images for varying time lags and correlating them provides the characteristic relaxation times for the system, $\tau = (Dq^2)^{-1}$, as function of the scattering wavevector q. The detailed calculations are given in ref. [69].

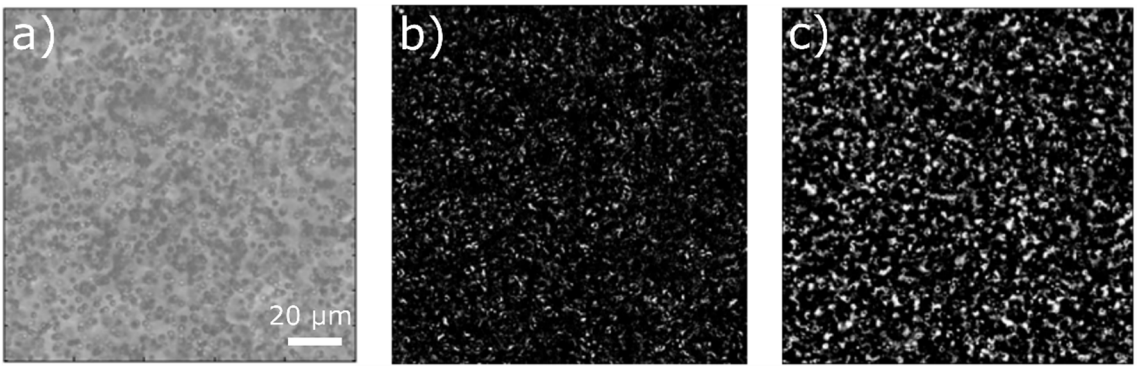

Figure 2.8. Microscopy images in DDM. a) 527 nm colloids in water at 1% v/v. b) The difference of two images separated by 75 ms. c) The difference of two images separated by 5 s. Modified image taken from ref [69].

DDM was used to measure the diffusivity of tracer particles trapped in the interstices of a refractive index-matched colloidal gel using a MATLAB programme developed by S. H. Nathan. Several one-minute-long fluorescence movies were taken by focusing at

different heights in the sample (Nikon Ti Eclipse microscope, 1024x1024 frame size, 60 frames per second). The movies were analysed and the apparent average diffusion constants D were extracted for each height by plotting the relaxation times $\tau(q)$ versus the scattering wavevector q.

3 COLLOID SYNTHESIS AND FUNCTIONALISATION

Research on functional polymer particles has grown significantly in the past few decades [70, 71]. Polymer colloids are important in many fields of technology such as in paints and coatings, ceramics, cosmetics, biotechnology (biosensing, drug delivery and bioseparation) and optoelectronics [72–77]. Functional particles bear a number of important features ranging from large specific surface areas, small sizes, high mobility to tuneable composition, surface properties and morphology [70]. Spherical latex particles have been the focus of said research mainly due to the ease of synthesis. Classical chemical polymerisation techniques (emulsion, dispersion, mini-emulsion, surfactant-free emulsion using a range of solvents) and more esoteric physical approaches (solvent evaporation, supercritical fluids) are used in making polymer particles [75, 78–86]. Functionality can be introduced through the modification of shape or by grafting ligands to the surface of a particle. DNA, as detailed in Chapter 1.2, is a great surface modifier due to its tunable and thermally reversible interactions.

This chapter focuses on developing protocols to manufacture surface-functionalised polymer (polystyrene, fluorinated latex) particles in size ranges of 50-1000 nm, making them perfect candidates for DNA-coated colloid self-assembly experiments detailed in later chapters.

3.1 Fluorinated Latex Colloids

2,2,3,3,4,4,4-heptafluorobutyl methacrylate, the fluorinated methacrylate monomer (HFBMA), was first used by Koenderink et al. [87] to synthesise fluorinated latex (FL) colloidal particles with a low refractive index ($n_{\mathrm{FL}} \approx 1.37$), making them making them attractive for studies on dense colloidal systems in aqueous media. Emulsion polymerisation and seeded growth were used to produce FL particles in the range of 50-700 nm, mostly by tuning the amount of monomer present in the reaction vessel. Subsequent work introduced more control over particle size by using microemulsion polymerisation, however, no attempts at surface functionalisation were made [88].

3.1.1 Synthesis

We first decided to manufacture FL particles in different sizes to better understand the synthesis and the factors affecting the particle size. Rather than playing with the starting concentration of the monomer(s), size control of the fluorinated latex (FL) particles was first achieved by varying the amount of the surfactant (sodium dodecyl sulphate – SDS) in the reaction vessel. This approach was called method #1. Emulsion polymerisation was employed as it used fewer reactants. Typically, the synthesis was done following the protocol described in Chapter 2.1.1 and varying the SDS concentration (0 – 0.2 wt%). The reaction was stopped after 12 h. The resultant suspension was then purified via dialysis and the colloids analysed. Particle sizes were determined by dynamic light scattering (DLS) and scanning electron microscopy (SEM). The DLS diameter of the colloidal particles was found to decrease with the increasing amount of SDS present in the reaction (Figure 3.1).

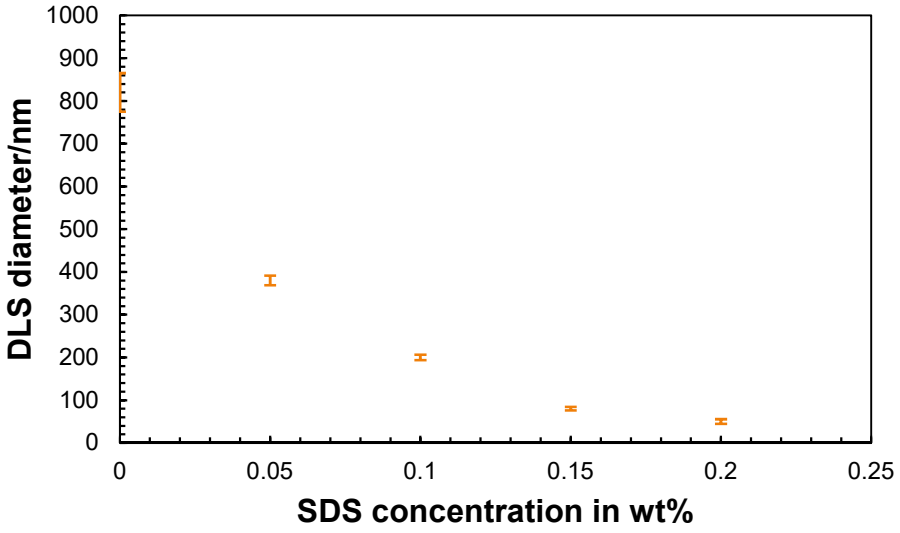

Figure 3.1. DLS diameters of FL particles made by emulsion polymerisation, using method #1. The amount of SDS present during emulsion polymerisation of 1.3 g HFBMA in 50 ml water controls the diameter of the resulting FL particles.

The FL colloids all had polydispersity indices (PDI, defined as the normalised second cumulant of the fit to the intensity correlation function in DLS), below 0.1, indicating a small size distribution in our colloidal suspensions. SEM imaging confirmed this, with the majority of colloids appearing uniform, with a small number of smaller particles (Figure 3.2; note that the particle sizes obtained from SEM images were smaller that the hydrodynamic diameters obtained from DLS measurements). The smaller diameters with

more ionic surfactant during synthesis is expected as the SDS can then stabilise a larger surface area, making the particles smaller, assuming the amount of monomer is the same.

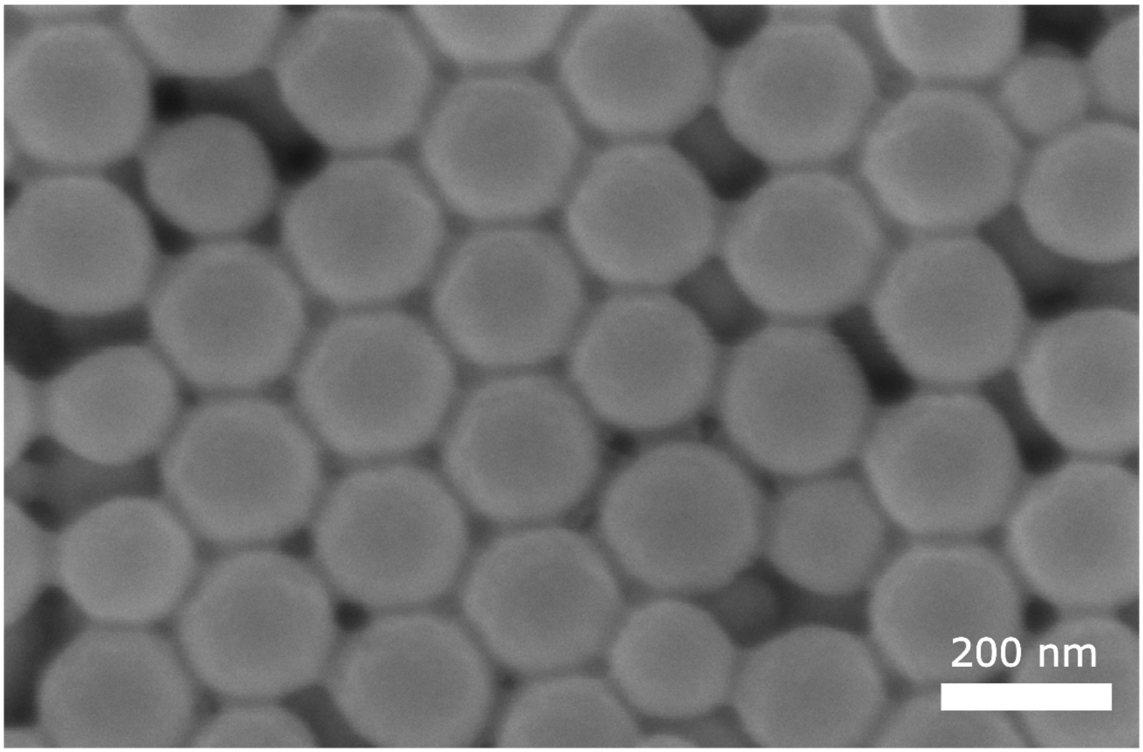

Figure 3.2. SEM image of ~200 nm diameter FL particles.

Using method #1 with stirring speeds of 300-600 rpm during the reaction process, we observed some aggregation after the synthesis was halted. More reliable results were achieved by increasing the stirring to 1000 rpm and keeping the SDS concentration constant at 0.015% w/w – size control was achieved through varying the monomer concentration, focusing on 80-200 nm diameter range (Figure 3.3). This approach was called method #2.

This again is explained by the same surface area argument – as the amount of surfactant in the emulsion stays constant with increasing amount of monomer, the resulting particles become larger in order to have a stable surface.

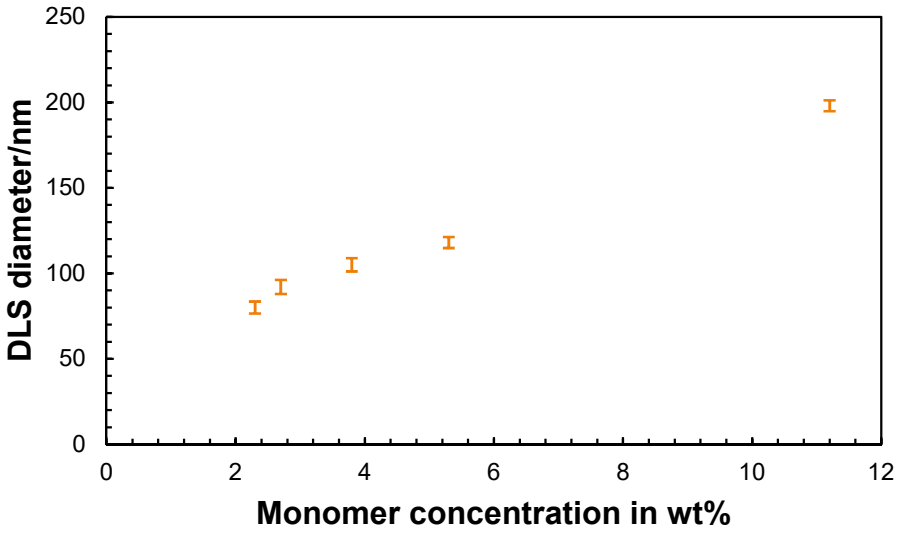

Figure 3.3. DLS diameters measured for FL particles made by emulsion polymerisation using method #2. The SDS concentration was kept fixed at 0.015% w/w.

Now this method resulted in no sediments or aggregates after the reaction was done and yielded monodisperse particles (PDIs < 0.1). 200 nm particles obtained using method #2 are shown in Figure 3.4, demonstrating that due to their low refractive index their aqueous solutions can be index-matched by adding the appropriate amount of sucrose.

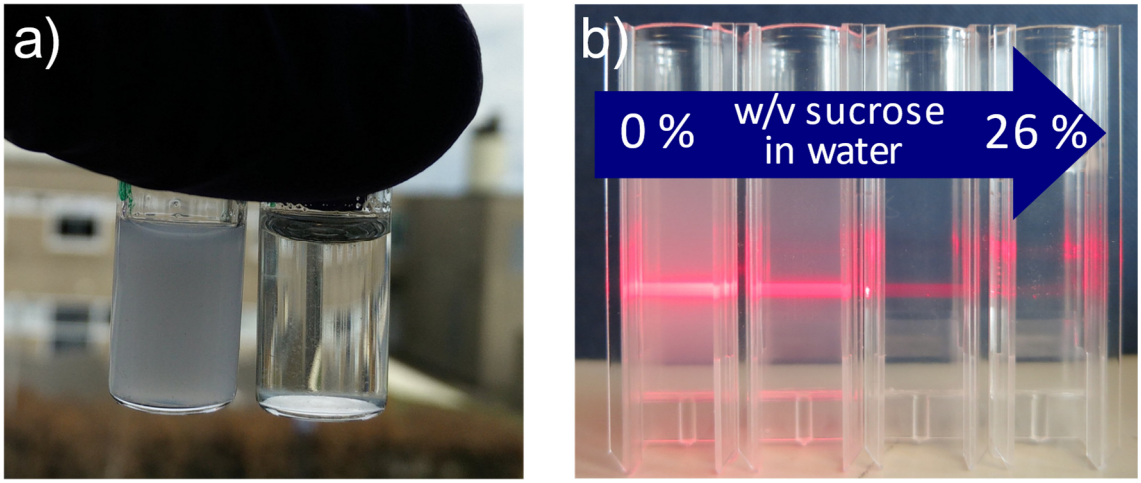

Figure 3.4. Refractive index-matching FL particles in water with sucrose. a) 200 nm FL particles at 2% v/v in water (left) and in water containing 26% w/v sucrose (right). b) the same FL particles in water (left cuvette) and sucrose solution in water. The laser illuminates the suspension from the right.

3.1.2 Functionalisation: Aminated Particles

In our first attempt at functionalisation, we used the biotin-avidin lock-and-key mechanism to attach DNA to the FL colloids. For this we used polylysine-g[3.5]–polyethylene glycol–biotin (PLL-PEG-biotin), a comb-like polymer with a positively charged lysine backbone that readily adsorbs to negatively charged surfaces. To each 3.5 lysine repeat units, a PEG chain is attached. These PEG chain ends carry a covalently bonded biotin group. In the commercially available PLL-PEG, either 30% or 50% of all PEG chains are biotinylated. An excess of PLL-PEG-biotin was mixed with unfunctionalised FL colloids (820 nm diameter) in phosphate buffer (PB, 10 mM, pH = 7.4) and incubated for 1 h while being stirred. The particles were then centrifuged and washed several times, and their zeta-potential was measured. It became close to 0, showing that all surface charges had been neutralised and the colloids had been coated with the biotinylated polymer. First adding streptavidin, which has four binding sites for biotin, to the FL colloid suspension, then washing them to remove unreacted streptavidin and only then adding biotinylated DNA harboured several problems: streptavidin could already bind two colloids irreversibly, DNA could bind to free streptavidin forming quadruplets and PLL-PEG-biotin could theoretically come off the colloids if the buffer conditions changed.

Another good approach was to use a co-monomer, which already had a functional group. For this, 2-aminoethyl methacrylate hydrochloride (SigmaAldrich) was chosen as it easily polymerises with HFBMA and would also stay in the aqueous phase of the emulsion during synthesis as it is hydrophilic, thereby polymerising primarily on the surface of the emulsion droplets. Hence, we followed a slightly modified FL particle synthesis: 1.3 g HFBMA was emulsified together with 33 mg of aminoethyl methacrylate hydrochloride in 50 ml of deionised water at 600 rpm at 70 °C under nitrogen atmosphere. Polymerisation was started with 27 mg of KPS and the reaction continued for 24 h before being quenched on ice. The resulting 1100 nm diameter particles (FL-NH_2) were purified by dialysis. FTIR analysis of the dry particles confirmed the presence of primary amines, so surface functionalisation with DNA was attempted.

The DNA conjugation protocol was adapted from ref [89] and the work of Ruff et al. [90]. In the first step, the FL-NH_2 colloids were reacted with sulfosuccinimidyl 4-(N-maleimidomethyl)cyclohexane-1-carboxylate (sulfo-SMCC, SigmaAldrich) in phosphate buffer (PB, pH 7.4, see Figure 3.5 a). Sulfo-SMCC contains N-hydroxysuccinimide (an NHS ester) and a sulfhydryl reactive maleimide group: NHS

esters react with primary amines at pH 7-9 to form stable amide bonds, while maleimides react with sulfhydryl groups at pH 6.5-7.5 to form stable thioether bonds [89]. At the same time thiolated DNA was reacted with 1,4-Dithiothreitol (DTT, SigmaAldrich) in PB to cleave the disulfide bridge: the oligomers came from the vendor with the disulfide linkage intact to minimise the potential for oxidation. After cleaving, the DNA was purified by size chromatography in resin columns, while the colloids were washed by centrifugation. Then the DBCO-DNA was reacted with the colloidal particles in PB (Figure 3.5 b). Incremental salting was used to screen the charges on the particle surface and therefore help pack more DNA strands on said surface: the NaCl concentration was increased to 500 mM over 1 h and the colloids were then left to react for 12-16 h. Two batches of these colloidal particles were prepared, one with **A** ssDNA, the other with its complementary strand **A'** (Figure 3.6). The DNA was chosen to only have single-stranded spacers and a 9 base sticky end (Figure 3.6), with a confirmed melting temperature (on 500 nm diameter colloidal particles) of just over 50 °C [53]. After washing, the two batches were mixed in an equimolar ratio at a total concentration of 5% v/v in phosphate buffered saline (PBS: 10 mM PB, pH 8.0, containing 50 mM NaCl to facilitate DNA hybridisation).

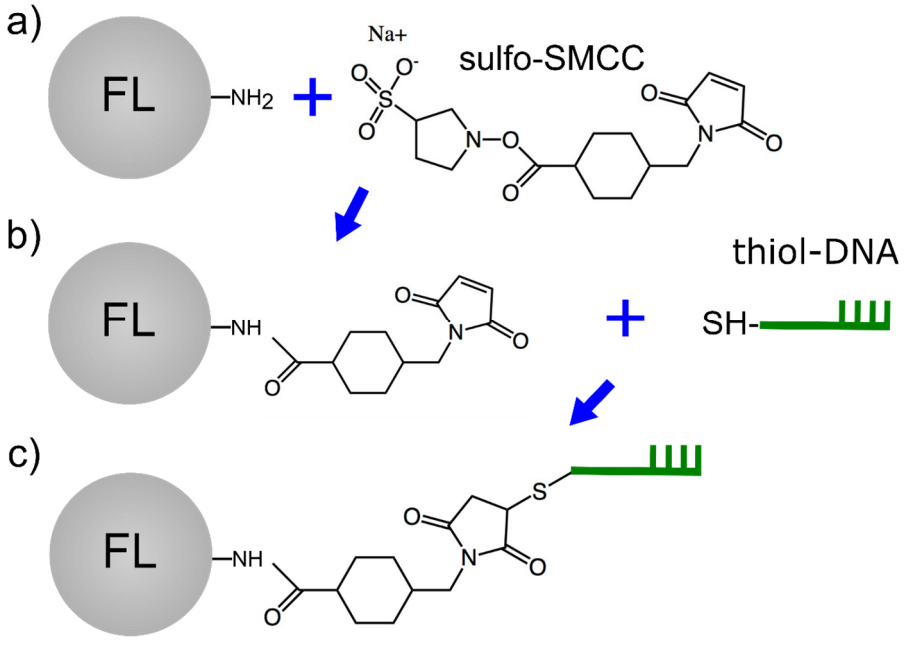

Figure 3.5. Cartoon showing aminated particle coating with DNA using sulfo-SMCC. a) The ester part of sulfo-SMCC reacts to the amines on the particle surface. b) Sulfhydryl-functionalised DNA reacts to the maleimides now present on the particle surface. c) DNA on the particle surface.

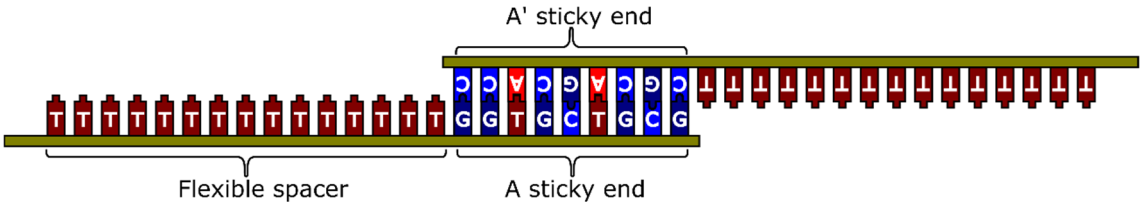

*Figure 3.6. Cartoon of **A** and **A'** DNA strands with hybridised sticky ends. A, T, C and G are the bases.*

Immediately after mixing the complementary strand samples, aggregation was seen in the tube (Figure 3.7, right). Aggregates were visible in the capillary tube, with the sample ready for microscopy (Figure 3.7, left). Optical microscopy revealed thermally responsive aggregates: as the sample was slowly heated and imaged, a sharp dissociation of the aggregates was observed at $T = 49$ °C, slightly below the expected melting temperature. Moreover, the free particles then sank to the bottom of the sample chamber due to their size and density (1100 nm diameter, while $\rho_{HFBMA} = 1.345$ g/cm^3). Indeed, such particles should not even be called colloids. Nevertheless, the aggregation due to DNA hybridisation was thermally reversible and the particles could aggregate-dissociate at least 3 times, however, some of them formed permanent aggregates which would not dissociate upon heating.

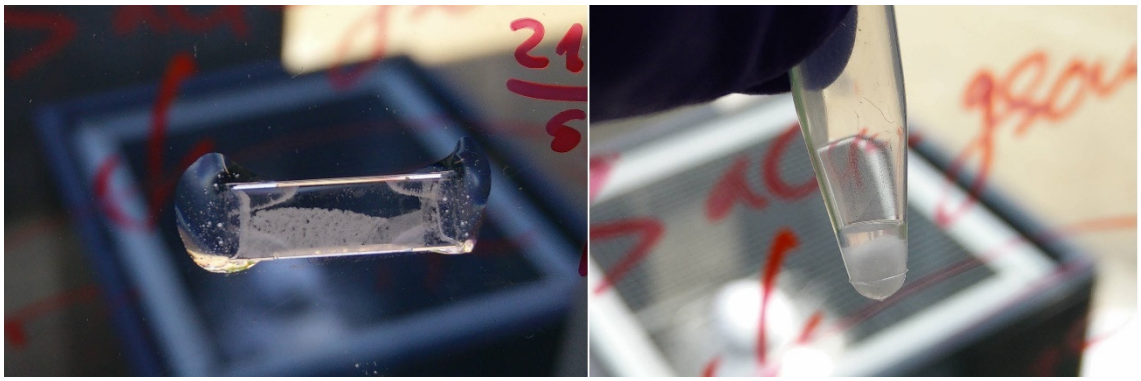

Figure 3.7. 1100 nm diameter FL particle aggregation through DNA visible by the naked eye. Left: a 5% v/v FL particle aggregates in a capillary. Right: the same sample in a tube.

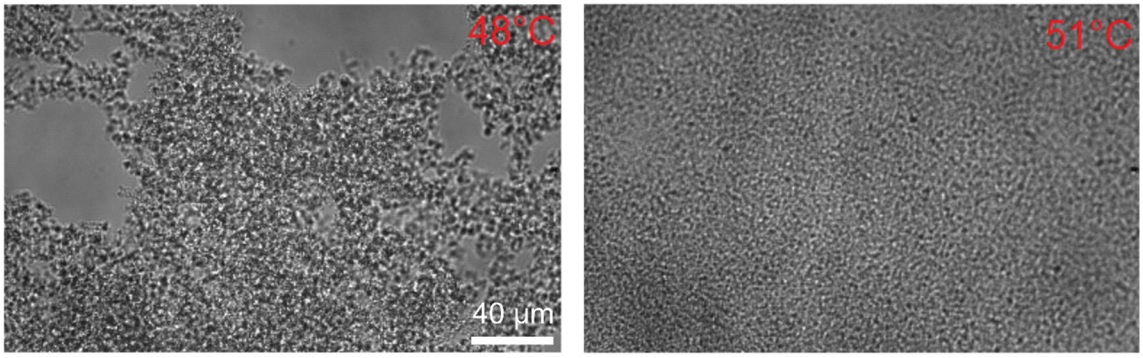

Figure 3.8. Optical microscopy images of 1100 nm diameter FL particle system.

While this functionalisation method did result in DNA-coated FL particles, improvement was needed as the partial irreversibility of the aggregation/melting process suggested the presence of non-specific binding. Indeed, the low melting temperature was an indication of a low particle surface coverage with DNA, which was confirmed by fluorescence-based assay results: the 1100 nm diameter particles had ~10,000 DNA strands per particle (so one binder would occupy roughly 380 nm^2), a sufficient number to induce DNA-mediated aggregation, but possibly not high enough to prevent non-specific aggregation through van der Waals forces.

A few solutions could have improved this system, mainly the use of double-stranded DNA spacers to provide additional steric and electrostatic stability, and the use of smaller particles.

3.1.3 Functionalisation: Amphiphilic Block Copolymers and Swelling-deswelling

In 2015 Oh et al. [50] demonstrated a way to functionalise polystyrene (PS) particles with a high density DNA coating of 223,000 strands on one 1 µm diameter colloid, corresponding to 14 nm^2 of area for one binder on the particle surface. This was achieved by using an amphiphilic diblock copolymer, polystyrene-b-poly(ethylene glycol) (PS-b-PEG), with the hydrophobic PS block physically trapped inside the particle, while the hydrophilic PEG part was sticking out. The diblock was first functionalised with azide groups to allow for DNA attachment through a click reaction after the linker was on the particle. To get the polymer onto the surface of the colloids, the particles were swollen with tetrahydrofuran (THF) in the presence of PS-b-PEG, allowing for the PS end of the diblock copolymer to be adsorbed to the particle surface at first and then incorporated into the particle when swollen. The samples were deswollen by reducing the THF volume fraction and eventually evaporating the THF, with the particles now having the PS ends

of the diblocks inside them, leaving the PEG ends sticking out. DNA was then attached to the free azide-functionalised PEG end son the surface of the particles through a strain-promoted alkyne–azide cycloaddition (SPAAC). The SPAAC reaction occurs over a day, but it does not require copper as a catalyst, which could damage DNA [91].

This protocol was adapted to coat the FL particles. Three commercially available block copolymers were used: $PS_{(13)}$-b-$PEG_{(127)}$, Synperonic F108 (poly(ethylene glycol)-b-poly(propylene glycol)-poly(ethylene glycol), $PEG_{(133)}$-b-$PPO_{(50)}$-b-$PEG_{(133)}$) and Synperonic F127 ($PEG_{(100)}$-b-$PPO_{(65)}$-b-$PEG_{(100)}$). F108 and F127 were significantly cheaper, but had been reported to result in lower coating densities on PS particles [92]. The triblocks also have a significant molecular weight distribution, so the number of repeat units is the average [93]. In addition, two more diblocks were synthesised for us by Dr Clément Mugemana and Prof Nico Bruns at the Adolphe Merkle Institute: $PS_{(30)}$-b-$PEG_{(79)}$-N_3 and poly(heptafluorobutyl methacrylate)$_{(14)}$-b-poly(ethylene glycol)$_{(79)}$-N_3 ($FL_{(14)}$-b-$PEG_{(79)}$-N_3) (see Appendices). The first three polymers were functionalised with azide groups through mesylation and subsequent azide substitution, as described in detail in Chapter 2.2.1.1 and Chapter 2.3.1. An outline is shown in Figure 3.9. The presence of the azides at the PEG ends was confirmed by ATR-FTIR spectroscopy performed on dry polymer samples. An example FTIR spectrum is given in Figure 3.10. The absorption peak at 2100 cm^{-1} indicates the presence of azides [94].

200 nm diameter FL particles (FL200) were chosen for functionalisation experiments due to their convenient size: they would stay dispersed without sedimentation for weeks (true colloids) and yet they were not too small so as to be completely invisible using optical microscopy.

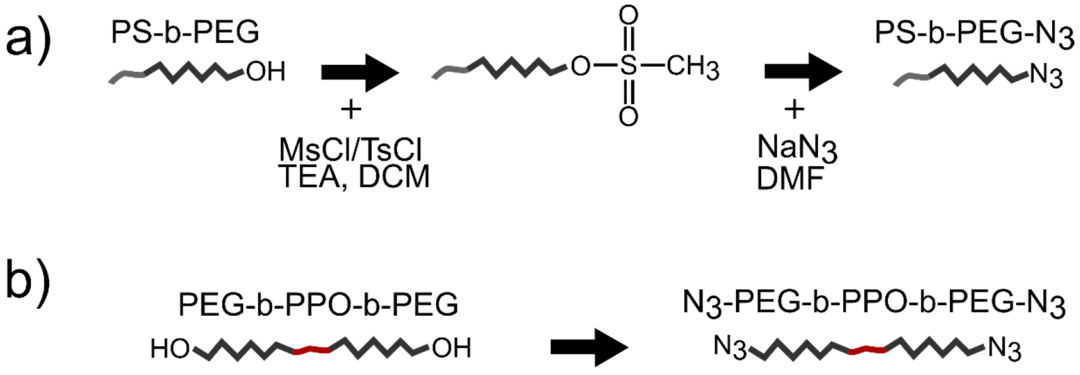

Figure 3.9. Cartoon showing block copolymer functionalisation with N_3. a) Diblock functionalisation. b) Corresponding triblock functionalisation.

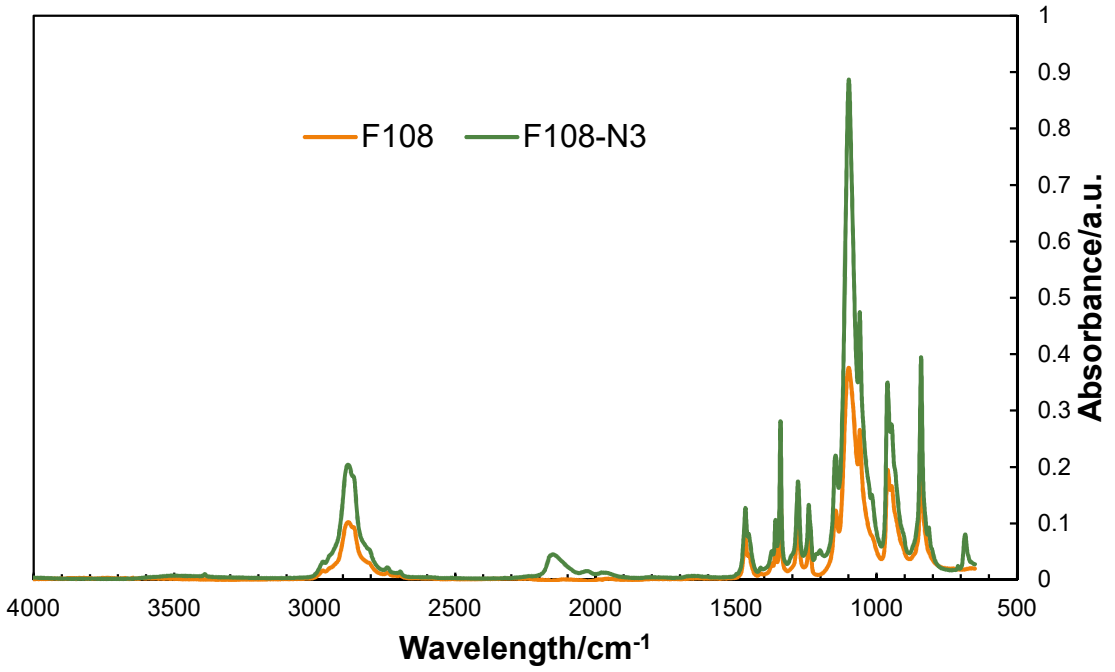

Figure 3.10. ATR-FTIR spectroscopy result of F108 and F108-N_3 polymer samples.

The swelling behaviour of 200 nm large FL particles, dubbed FL200 for the remainder of this dissertation, was investigated without the presence of block copolymers. 1% v/v aqueous dispersions of FL particles were swollen with different volume fractions of THF, up to 50%, shaken for 30 minutes and deswollen by adding deionised water to the solution and evaporating the THF at 60 °C. Subsequently their size was determined by DLS. THF fractions above ~35% v/v were found to result in particle dissolution.

Subsequently, 4 block copolymers were tested with FL200 particles by swelling-deswelling them at 20% and 33% v/v THF (full protocols in Chapter 2.2.1.2). Figure 3.11 a) shows the outline of the swelling protocol when using a diblock copolymer. First, the particles were dispersed in water containing the diblock/triblock, which started adsorbing to the particles' surface. Then THF was added to swell the particles and allow the hydrophobic ends of the surfactants to diffuse into the particles. After adding water and deswelling the particles, the resulting colloids had high density PEG brushes.

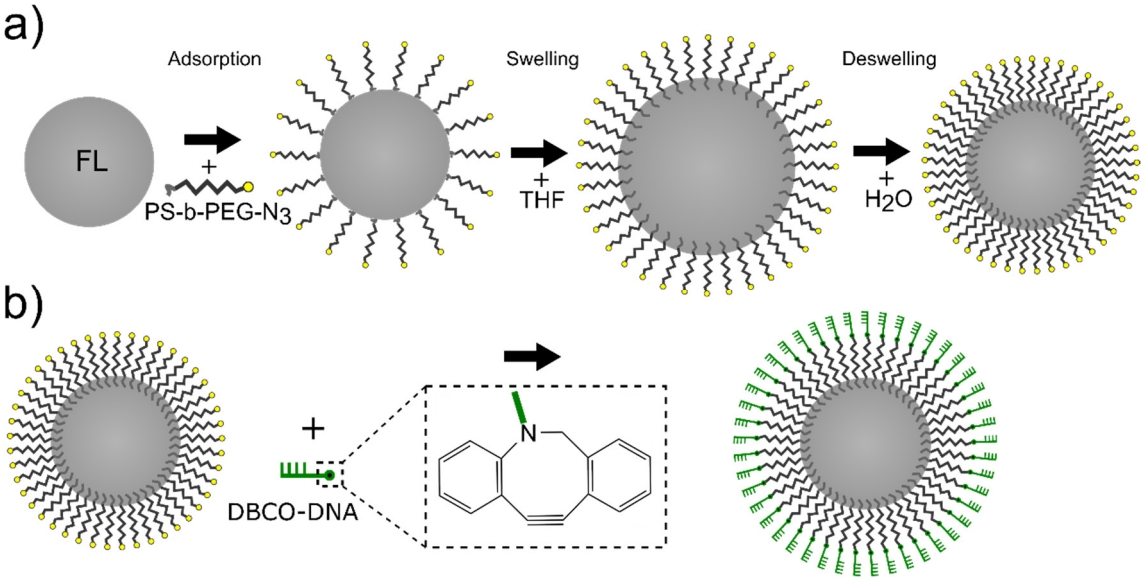

Figure 3.11. Cartoon illustrating FL200 particle coating with DNA via swelling-deswelling. a) PEGylation via swelling-deswelling. b) DNA coating via SPAAC.

After washing the PEGylated particles, fluorescence assays were done to quantify the PEG surface coating density of the colloids (full assay protocol in Chapter 2.4.5): Cy5-DBCO dye was reacted to the azides present on the PEG ends on the particles and the fluorescense was compared to a standard curve to extract quantitative information on the PEG surface density. Figure 3.12 compares the area per one binder - the smaller the area, the higher the coating density. The diblock copolymers are denoted by their hydrophobic block length (PS13, FL14), while the triblocks are referred to by their commercial names (F108, F127).

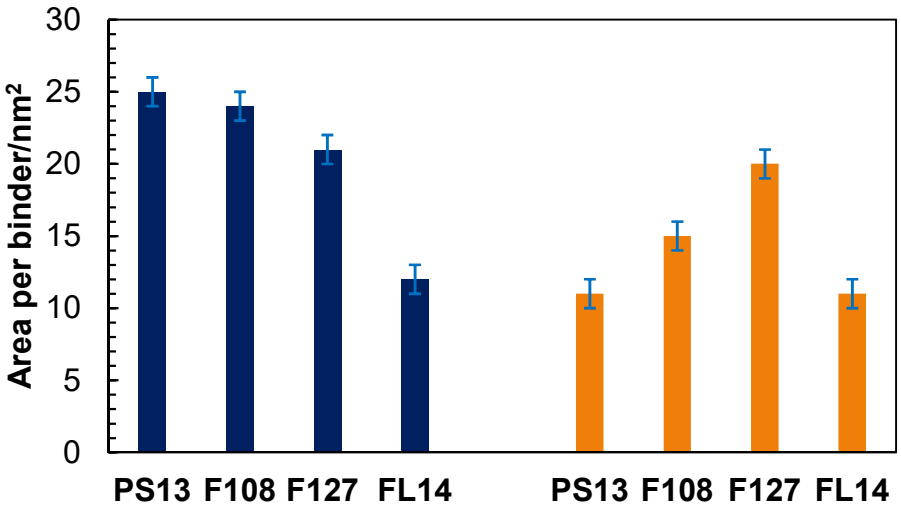

Figure 3.12. Block copolymer coating density on FL200 particles. Left, blue: 20% v/v THF during swelling. Right, orange: 33% THF during swelling.

Diblock copolymers (PS13, FL14) led to slightly higher PEG densities than the those achieved with the triblocks (F108, F127); in addition, 33% v/v THF allowed for even better coverage, with PS13 and FL14 coating density matching that or being slightly higher than that of Oh et al. [50].

DNA coating was then undertaken on the PEGylated FL200 particle samples (33% v/v THF swelling). The colloids were reacted with **A** and **A'** DBCO-DNA via a SPAAC, as described in Chapter 2.2.2 (see Figure 3.11 b). DLS and zeta-potential measurements allowed for simple monitoring of the success of the reaction after each step and were taken in the same 10 mM PB to make a good comparison possible.

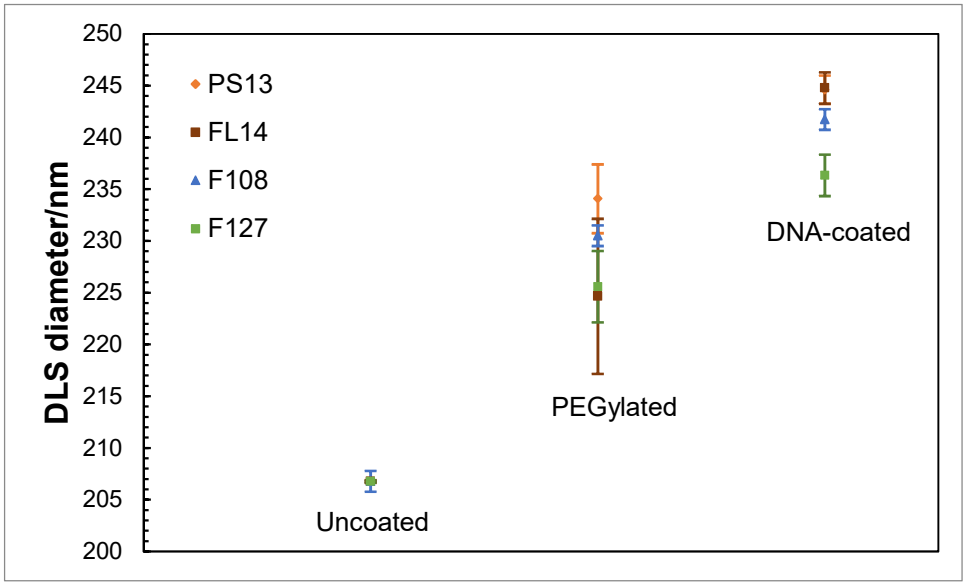

Figure 3.13. DLS diameters of FL200 particles at three stages of DNA coating. All measurements taken in 10 mM PB.

Assuming we use the same solvent, the polymer chains on the surface can exist in two conformations, 'mushroom' or 'brush', depending on the grafting density. Grafting density σ is the number of chains per unit area on the surface of a particle: $\sigma = \frac{1}{D^2}$, where D is the distance between two grafted ligands. The Flory dimension is given by $R_F \approx aN^{3/5}\left(\frac{v}{a^3}\right)^{1/5}$, where a is the Kuhn length of the polymer, N is the number of Kuhn segments and v is the excluded volume for one segment [50]. In the 'mushroom' regime, $D > R_F$, and the polymer chains lie far apart from each other and are unstretched. If $D < R_F$, the chains are in the 'brush' configuration and the polymers stretch out due to excluded volume interactions. The Kuhn length of PEG is 0.76 nm [95, 96], N varies from 39 to 65, and $\left(\frac{v}{a^3}\right)^{1/5} \approx \left(\frac{d}{a}\right)^{1/5} \approx 0.8$ nm, where d is the width of one PEG chain and is

taken to be 0.2 nm [50]. Therefore, R_F varies from 5.5 nm to 7.4 nm, meanwhile D varies from 3.2 nm to 5 nm. Even in the worst coating case, the PEG chains should be in the 'brush' configuration. The average height of the brush can then be calculated by applying the Flory theory for a polymer in a good solvent, which is the case for PEG in water [97, 98]:$\langle h \rangle \approx \left(\frac{1}{2}\sigma a^5\right)^{1/3} N$, which gives a 10 to 15 nm height range for the PEG on the surface. This explains why the PEGylated particles increased in diameter by about 25 nm on average, compared to the uncoated ones (Figure 3.13).

The DNA-coated particles displayed a moderate increase in their hydrodynamic radius owing to the relatively short 24 base-pair DNA strands used. Single-stranded DNA (ssDNA) has a persistence length of ~1 nm [99], which corresponds to about 3 base-pairs; this corresponds to about 4-5 nm length in the 'brush' case. Indeed, an average increase in the hydrodynamic radius of ~ 8-10 nm was seen when comparing the DNA-coated particles to the PEGylated ones, confirming the presence of a DNA brush.

Zeta-potentials of FL200 particles were also measured at all stages of coating (Figure 3.14). Uncoated particles were negatively charged (~ -80 mV in 10 mM PB) due to the polar potassium persulfate groups residing on the particle surface. PEGylated particles showed a zeta-potential much closer to zero, as the slip plane, where the potential was measured, had shifted away from the particle surface due to the presence of the PEG chains. ssDNA has a negatively charged backbone, therefore, the less negative zeta-potential at the DNA grafting points (ends of PEG chains) increased the coating density, with the help of incremental salting. The presence of DNA was once again confirmed by zeta-potential measurements of the DNA-coated FL200 particles, now showing potentials of ~ -35 mV for the triblock-DNA coatings and ~ -50 mV for the diblock-DNA coatings, down from -3 mV to -10 mV of the PEGylated particles.

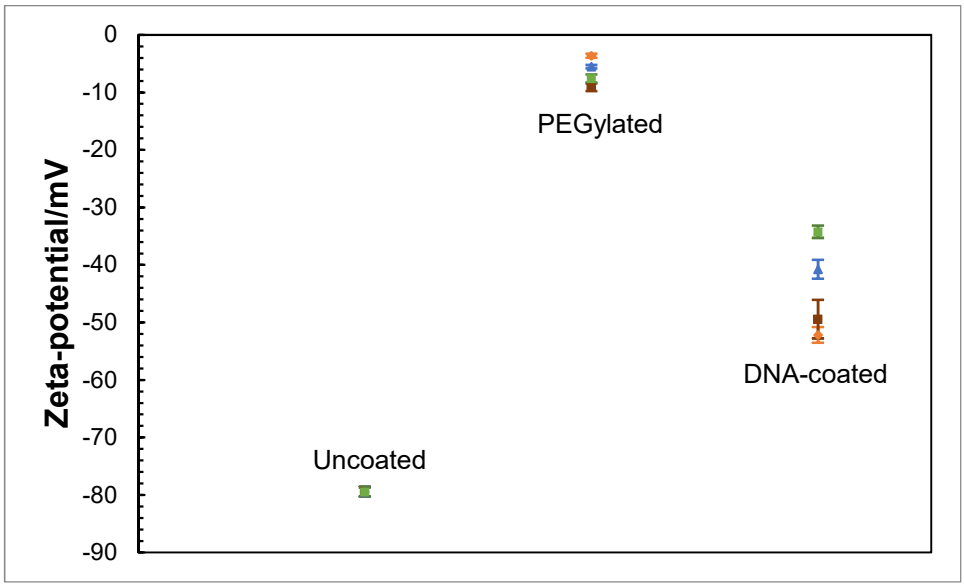

Figure 3.14. Zeta-potentials of FL200 particles at three stages of DNA coating. All measurements taken in 10 mM PB.

The final step was to test DNA-induced particle aggregation. For that, FL200 particles were PEGylated with PS13 diblock copolymer, split into two batches, one coated with **A** and the other with **A'** DNA (the sequence shown in Figure 3.6), respectively. The two batches were mixed in a tube in Tris-EDTA buffer (TE, 10 mM, pH = 8.0, containing 50 mM NaCl) and imaged in a sealed capillary (Figure 3.15). A Peltier device with a PID controller allowed for temperature control. The volume fraction of the colloids in the sample was ~10%.

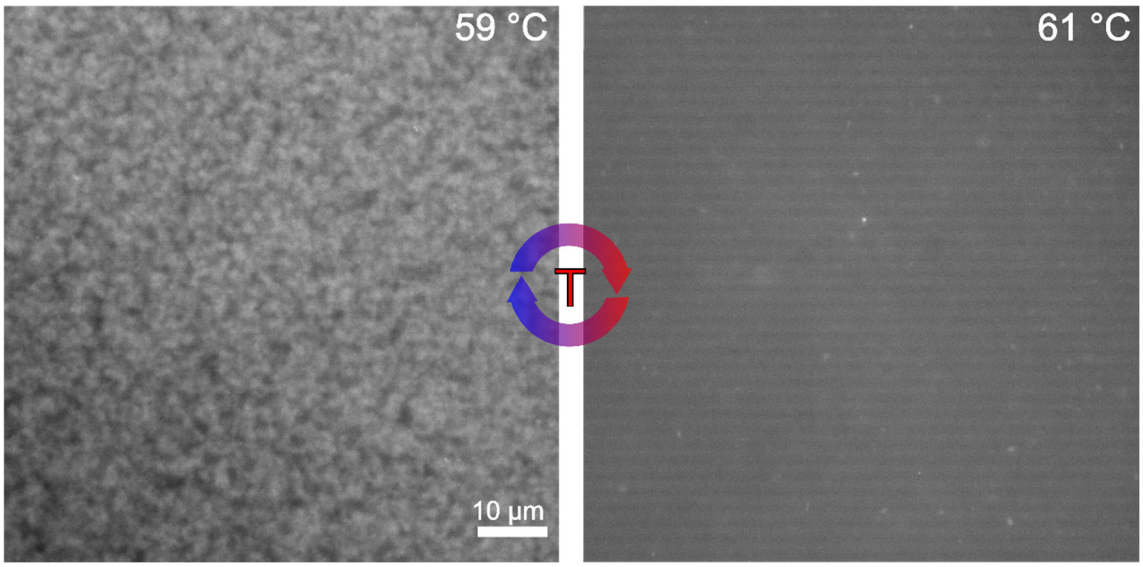

Figure 3.15. Epifluorescence optical microscopy images of an FL200 10% v/v gel sample below and above its melting temperature.

As the sample had been fluorescently labelled with a BODIPY dye during swelling (see Chapter 2.2), epifluorescence microscopy was done. Aggregates were seen at low temperatures, but once the sample reached ~60 °C, a sharp 'melting' was observed, whereby the DNA strands broke the hydrogen bonds between the double helices in the span of 1 °C, allowing the particles to enter the gas phase (Figure 3.15 right). This collective melting behaviour was explained in Chapter 1.2.2 (also see Figure 1.5). Upon cooling, aggregation of the particles was seen. T_{m}, the melting temperature, was determined to be 60 °C; moreover, the system could be thermally cycled many times.

3.2 Polystyrene Colloids

While the FL particles were well suited for refractive index-matching, their density ($\rho_{\mathrm{HFBMA}} = 1.345 \frac{\mathrm{g}}{\mathrm{cm}^3}$) meant that in aqueous solutions density-matching was near impossible. For systems not requiring index-matching, polystyrene (PS) particles are a good choice, their synthesis being well-documented and the cost of production an order of magnitude lower than of their FL counterparts [71, 86, 100, 101].

3.2.1 Synthesis

PS colloids with a diameter range of ~80-500 nm were synthesised using a charge-stabilised polymerisation method (either emulsion or dispersion), in which two monomers were used: the first was styrene, the second was a modified styrene molecule with a charged group: sodium 4-vinylbenzenesulfonate (SVBS). Typically, a radical initiator and SVBS were dissolved in water or a water/ethanol mixture and heated to 70 °C under nitrogen atmosphere (full protocol in 2.1.2). Styrene was then quickly added to the mixture and polymerisation was carried out for 24 h. As the KPS was heated, it degraded, generating radicals, which then triggered the polymerisation of the styrene monomers – a typical radical polymerisation reaction; that is why the styrene had to be added quickly once the KPS solution was heated.

Size control was achieved through the variation of the amount of KPS or SVBS (and then using ethanol/water mixture as the solvent). As determined by DLS and SEM, 80 nm, 200 nm, 420 nm and 800 nm diameter PS colloids were synthesised. The 200 nm PS particles (PS200) were of the highest interest due to their exceptional monodispersity (DLS PDI < 0.05; SEM image in Figure 3.16) and their size matching that of our FL200 colloids.

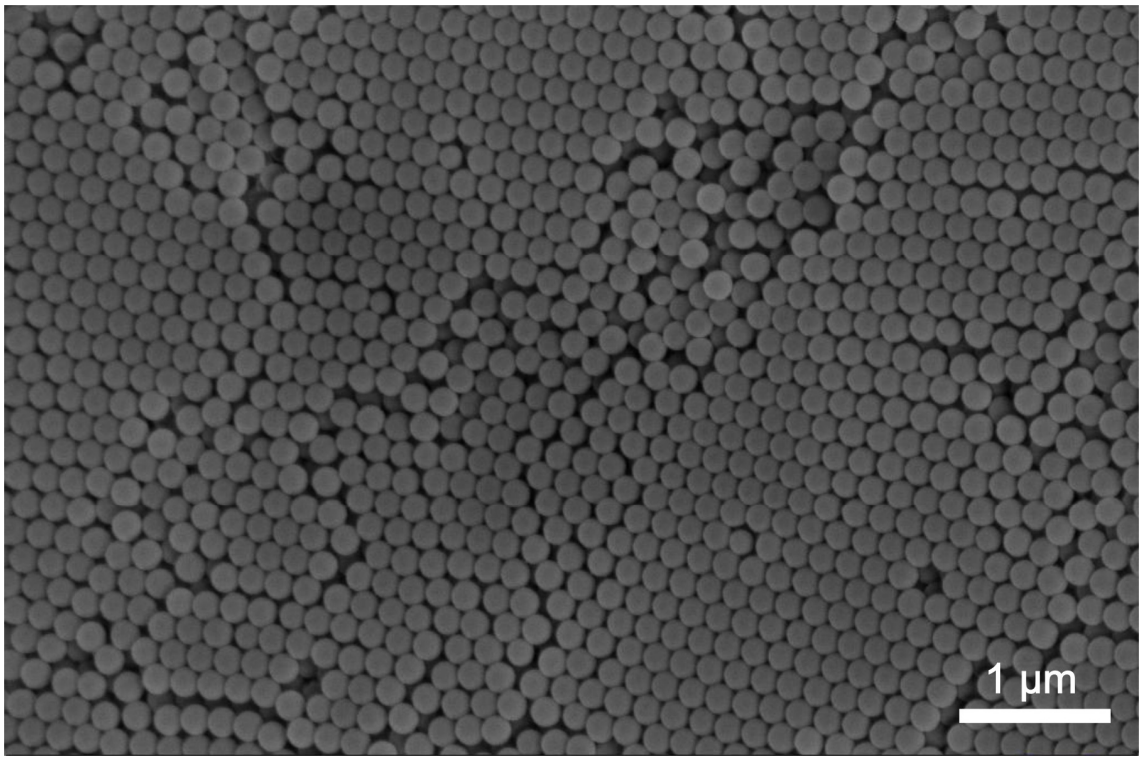

Figure 3.16 SEM image of PS200 colloids.

3.2.2 Functionalisation: Swelling-deswelling

As swelling-deswelling had proved to achieve high coating densities, the same strategy was employed in coating the PS particles. Rather than using 20% and 33% v/v of THF during the swelling, 50% was used, as it had been found to be the optimal fraction by Oh et al. [50]. FL14 was changed to PS30, with the idea that the polystyrene hydrophobic end would allow for a better coating than the fluorinated polymer one. As before, the particles were PEGylated and then reacted to Cy5-DBCO dye, with the full protocols described in Chapters 2.2 and 2.4.5. The fluorescence assay results are shown in Figure 3.17. Comparable coating densities were seen across all block copolymers. F108 x2 refers to double the concentration of the triblock during swelling; higher osmotic pressure should force more triblock molecules onto the particle surface. This however had a marginal effect on the coating density, going from ~ 11 nm^2/ligand (usual concentration of F108 during swelling) to ~ 10 nm^2/ligand (twice the concentration of F108); in absolute numbers, this corresponds to 11,500 and 12,500 strands per 200 nm diameter particle, respectively.

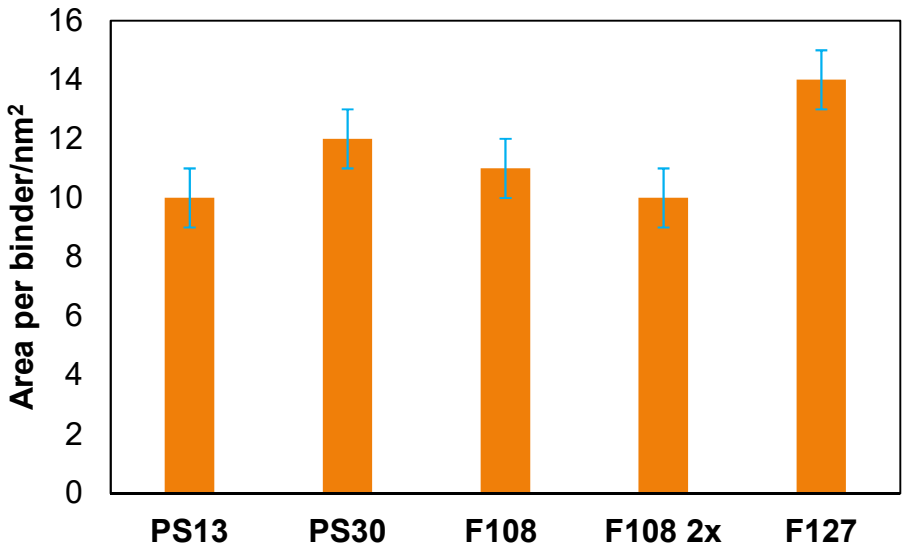

Figure 3.17. Block copolymer density on PS200 particles.

As before, DLS and zeta-potential measurements were done to monitor the coating process. Figure 3.18 shows the same trend in PS particle hydrodynamic diameter increase as was seen with the FL colloids. The PEGylated particles increased in diameter by ~ 25 nm, while the DNA-coated ones saw a further increase of ~ 10 nm, as expected.

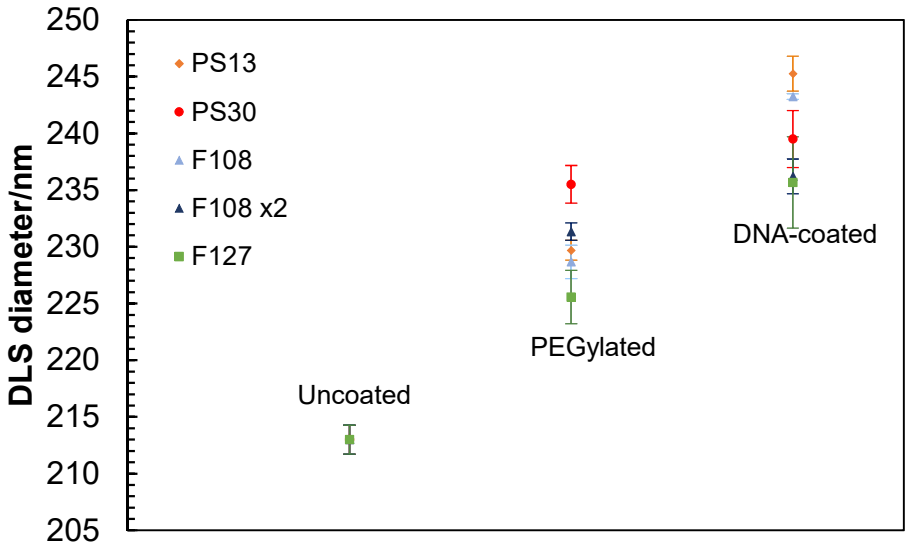

Figure 3.18. DLS diameters of PS200 particles at three stages of DNA coating. All measurements taken in 10 mM PB.

Zeta-potentials of PS200 colloids are shown in Figure 3.19. The uncoated colloids showed excellent stability in 10 mM phosphate buffer, owing to a high negative surface potential of ~ -80 mV. Predictably, the zeta-potential was close to zero for the PEGylated particles, while the DNA-coated ones regained some charge from the negatively-charged

backbones of the oligomers. Interestingly, the diblock-coated particles exhibited higher negative potentials, reaching -50 mV, compared to ~ -25 mV of triblocks, despite the fact that all coatings had similar surface azide densities.

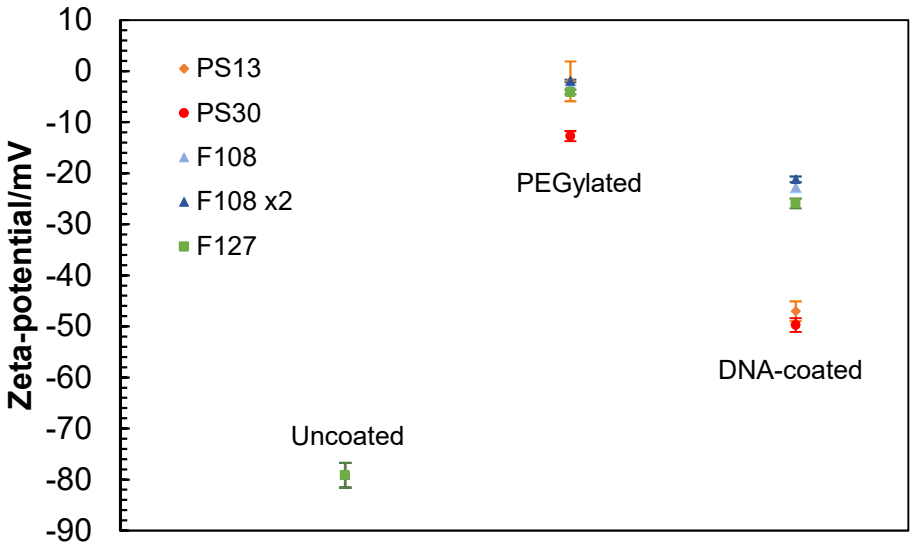

Figure 3.19. Zeta-potentials of FL200 particles at three stages of DNA coating. All measurements taken in 10 mM PB.

The last step, as with the FL200 gel, was to test DNA-induced particle aggregation. For consistency, only PS13-coated particles are shown below (Figure 3.20), although different block copolymers had produced very similar results in optical microscopy. The PS200-PS13 particles were again split into two batches and reacted to **A** and **A'** DNA. The two batches were then mixed, sealed in a capillary and imaged in the same conditions as the FL200 sample. The melting temperature was found to be about the same, however, the gel, upon cooling (the same 0.5 °C/min cooling rate from above the melting temperature), looked coarser than the FL200 gel. The primary reason behind this is believed to be sedimentation as the FL200 particles are much denser than their polystyrene counterparts. This topic will be further explored in Chapters 4 and 7.1. Another reason is light scattering as the PS particles have a much higher refractive index (~1.57). As seen with the FL200 sample, the PS200 gel could also be thermally cycled many times, showing the robustness of the coating.

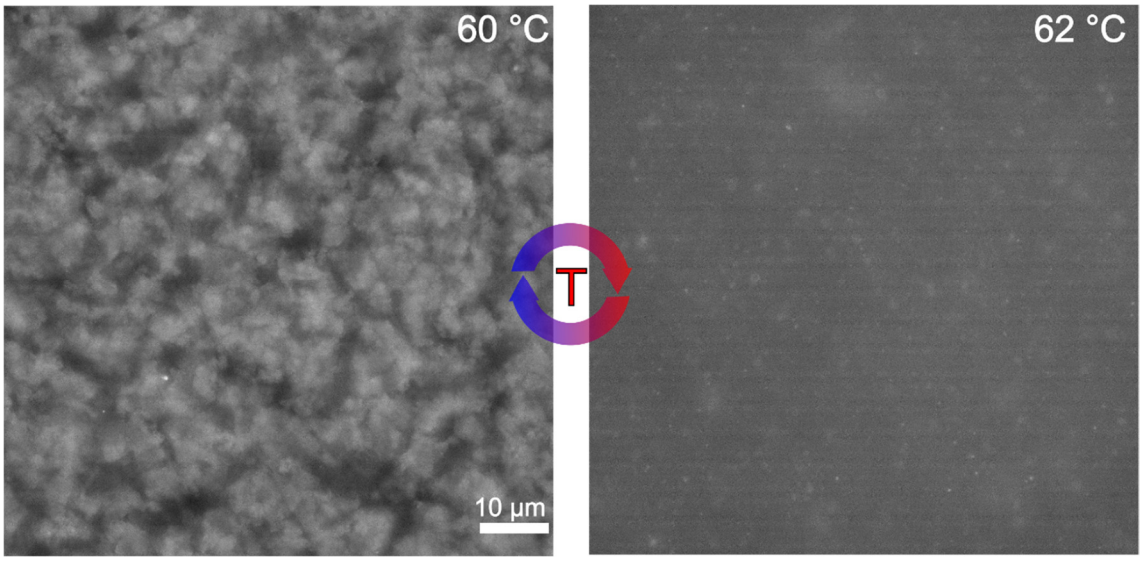

Figure 3.20. Epifluorescence optical microscopy images of a PS200 10% v/v gel sample below and above its melting temperature.

3.3 Conclusions

This chapter has laid out the foundation for making DNA-functionalised polymer particles, namely polystyrene and fluorinated latex colloids. The colloids were synthesised in-house by emulsion polymerisation, with the particle size controlled by a few parameters, mostly the relative amounts of reagents used. The particles were subsequently functionalised with DNA; this was achieved by first coating the colloids with either diblock or triblock copolymers through a swelling-deswelling process, and then reacting DBCO-functionalised DNA to the azide end-functionalised PEG chains then present on the particles. Different block copolymers in the end had similar azide coating densities on particle surfaces, mostly varying from ~10 nm^2/ligand to 15 nm^2/ligand (~12,500 and 8,400 ligands per 200 nm diameter particle, respectively).

Chapter 4 utilises the same particles, coated with PS13 diblock copolymer for consistency, albeit with more complex coatings, to induce two-step gelation. Chapter 5 utilises both diblock and triblock azide end-functionalised copolymers to convey functionality to oil droplets – a type of 'soft' colloids.

4 Dense Optically Transparent Colloidal Gels

Colloids with appropriately designed surface functionalities can readily self-assemble into a range of structures, including crystals, glasses and gels [43, 49, 51, 102–106]. DNACCs are of particular importance due to their controllability, selectivity and thermal reversibility of the bonds between two complementary single-stranded sticky ends [107]. Most colloidal particles used in research are metallic [43], silica-based [108] or polymeric [51]. Typical polymers include polystyrene (PS) and poly(methyl methacrylate) (PMMA). They are abundantly used due to the ease of synthesis and a variety of possible surface groups. However, at volume fractions over a few percent, the solutions of such particles become cloudy due to multiple-light scattering, making optical probing deep inside the bulk phase difficult. This is particularly problematic in aqueous solutions, in which the refractive index difference between water and the colloidal material is large. Index matching using organic solvents is one solution, another is using small angle X-ray or neutron scattering [109–111]. However, some applications require an aqueous fluid phase, such as the study of microbial transport dynamics through porous media [112, 113], water purification [114], or the solidification process of colloidal latex particles in drying films used in environmentally-friendly paints [115].

This chapter presents work on fluorinated latex (FL) particles that were functionalised with DNA via block-copolymers using a swelling–deswelling process to make high-volume-fraction colloidal gels, which turned completely transparent in sucrose–water solutions, enabling imaging deep inside the structure. Moreover, the specific binding-energy of DNA was exploited to construct mixed (FL and PS) core–shell (FL–PS and PS-FL) colloidal gels and perform structural studies in order to assess the characteristic length-scale of the gel as function of height in the partially sedimented gels. Fluorescently labelled PS particles were then used to demonstrate that their diffusivity could be traced

deep inside the transparent FL-particle gel and associated to the confinement posed by the varying pore sizes.

The text of this chapter is adapted from the manuscript in reference [116] written by the present author and E. Eiser. The work on particle synthesis was done together with Y. Lan, DDM tracking was done together with D. Joshi; all other experimental and computational tasks were performed solely by the present author.

4.1 One Component Gels

200 nm diameter FL particles (poly(HFBMA)) were chosen for gelation experiments due to their low polydispersity and excellent uncoated stability (see Chapter 3). After establishing a relatively straightforward synthesis, we chose the swelling-deswelling method of DNA-functionalisation due to its scalability, universality and large surface coating densities [50]. **A** and **A'** DNA strands were used (see Chapter 3.1.2). Double-stranded spacers were not necessary as the particles had been PEGylated with a high surface density polymer brush during the first step of the coating, ensuring good steric stability and thus eliminating the need for a longer, more rigid spacer. DBCO-DNA was then attached to the azide end-functionalised PEG using a SPAAC mechanism (full details in Chapter 2.2 and Chapter 3.1.3, summary in Figure 4.1).

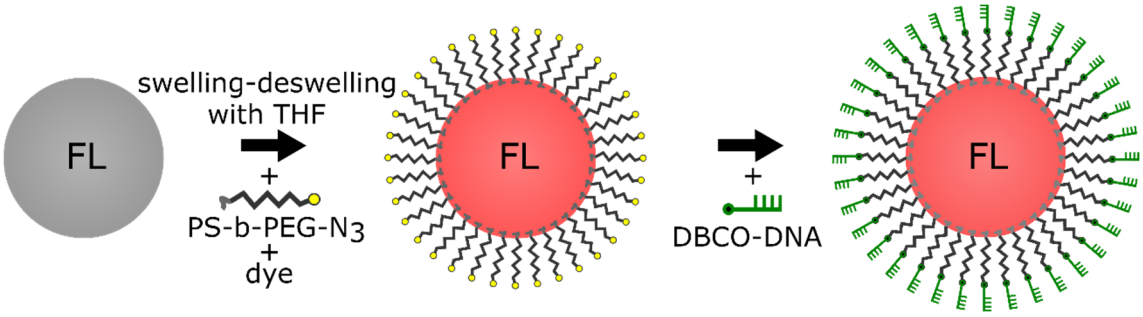

Figure 4.1. Cartoon outlining FL particle coating with DNA.

200 nm PS particles were coated using the same two-step protocol but with a slight alteration to the amount of THF used during the swelling (Chapter 2.2) and with a different dye (green fluorescence rather than red).

Samples were made of two types of particles in equimolar ratios: ones coated with **A** and the others with **A'** – the complementary strand to **A**. The particles were mixed in a tube in Tris-EDTA buffer (TE, 10 mM, pH = 8.0, containing 50 mM NaCl, 12% w/w sucrose for density-matching) to facilitate the DNA hybridisation. The FL particle samples contained 22% w/w sucrose in TE to refractive index-match the colloids. The addition of

sucrose did not alter the melting temperature [41]. The samples were loaded into sealed glass capillaries and heated to 70 °C, well above the **AA'** melt temperature, until they reached their equilibrium colloidal-gas phase, and then cooled slowly – 0.5 °C/min – to room temperature (RT), deep inside the 2-phase region. These slow cooling rates resulted in highly reproducible gel structures generated by arrested spinodal decomposition [117]. The same structural characteristics of these gels were seen over many melting-cooling cycles.

Confocal microscopy *z*-stacks were then taken at RT, sampling structural changes with respect to the height z of the x-y plane in the sample. Chord analysis was done on the samples (Chapter 2.5.1) to extract information on the 3D structure and separation mechanism of these gels. The results for 10% v/v samples are shown in Figure 4.2 a, where exponential functions with characteristic decay lengths λ_{phase} were fitted to the length distributions of the chords in log-linear plots. As the chord distributions behaved exponentially, the conclusion was that the aggregates were the result of spinodal decomposition rather than diffusion limited aggregation (whereby the distributions follow a negative power law and the aggregates have a fractal surface) [63, 64, 118, 119]. These length-scales were then plotted against the height in the sample z, with $z = 0$ being the bottom of the sample chamber (Figure 4.2 b). It is important to elaborate the experimental set up a bit further at this point: all of the samples were injected into rectangular glass capillaries ('sample chambers') which were then sealed, glued to microscopy slides and imaged in an inverted optical microscope. Note that because it was almost impossible to align the samples perfectly horizontally in the microscope, λ_{phase} values were plotted for $z \geq 2$ μm.

The first difference between the FL and PS gels was apparent - it was not possible to image the PS samples deeper than $z \approx 14$ μm due to multiple-light scattering and adsorption stemming from the difference in refractive indices between water and PS ($n_{\mathrm{PS}} \approx 1.56, n_{\mathrm{water+12\%\,sucrose}} \approx 1.35$), while the FL samples could be imaged up to z ≈ 70 μm.

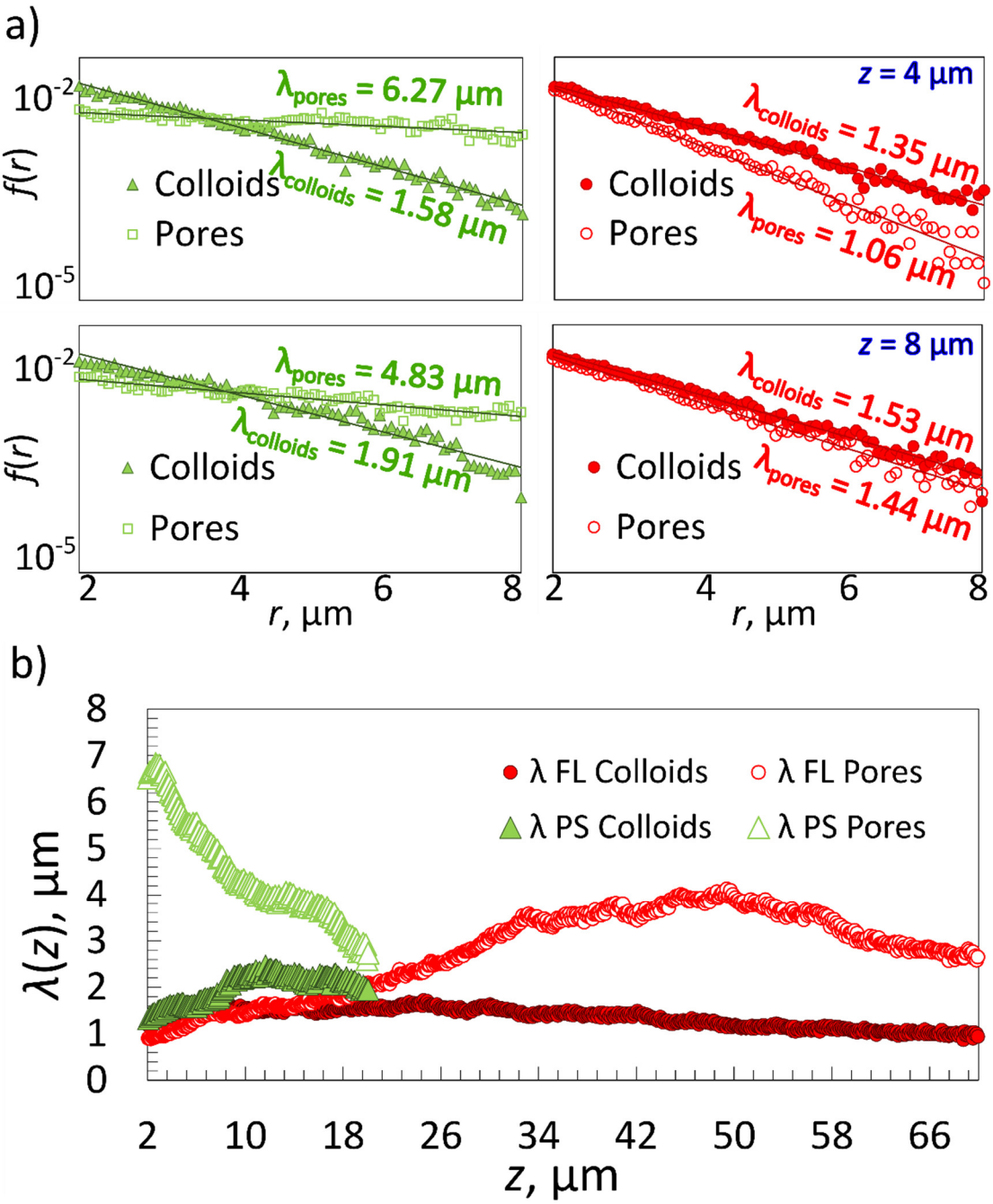

Figure 4.2. Chord analysis results for one-component FL and PS gels. Chord length distributions of a density matched 10% v/v PS-gel (green fluorescent; left) and an FL-gel (red fluorescent; right) at a given height z in the sample. b) Characteristic length-scale λ as a function of imaging depth z of 10% v/v colloidal gels, containing either PS or FL particles. Part of this figure appears in ref. [116] *and was created by the present author.*

Comparing the two percolating gels further, it was seen that the PS-sample in a density matched medium displayed a smaller decay length of the gel-phase than the fluid-phase (pores) at z = 8 µm, in agreement with previous experiments performed on 500 nm diameter PS colloids [53]. In fact, due to the density matching, one would expect to

observe the same decay lengths for gels and pores for all heights. However, it appears that the gel-structure became 'less dense' with increasing height. This could be rationalized by two factors: it remained difficult to perfectly density-match the sample, in particular once the macroscopically large gel had formed and the size of the clusters had become much larger than the colloids themselves. To elaborate further, the reader should understand how density matching was achieved. DNA-coated 200 nm diameter PS particles were suspended in phosphate buffer (PB) containing dissolved sucrose and spun at 20,000 g for 30 min. The samples were then visually inspected – if there was any sedimentation or creaming, the sucrose concentration was adjusted and the process repeated again. Once there was no visible stratification after spinning, they were deemed density matched. However, since in the gelation experiments the particles would aggregate upon activating the DNA-mediated attraction, the effective particle size was the size of a cluster of colloids, which was ~10 times larger than the size of one colloidal particle, making the clusters much more sensitive to small fluid-colloid density mismatches. The second reason was that at this height in such a strongly scattering sample the fluorescence detected in reflection becomes weaker, hence the gel phase was darker and increasingly larger errors were made.

In contrast, the refractive index matched FL-particle gel could be visualized up to 70 μm deep into the sample. This is illustrated in Figure 4.3 where both gels contained the same amount of dye. In the PS image, the gel was a lot more blurred and dark compared to the FL sample at the same height.

However, because of the density difference between the FL particles and the buffer solution, strong sedimentation effects on the gel structure were observed. This was reflected in the equal decay lengths for fluid and gel regions at z = 8 μm, that suggested a local volume fraction occupied by the colloidal gel was roughly 40%, despite the overall value being only 10%. This was also noticed in the decay length of the gel structure that became increasingly non-exponential at larger r (not shown here). This effect will be discussed further in the following sections. In addition, the average pore size was steadily increasing until around z = 50 μm where it started to decrease, possibly due to scattering – perfect refractive index matching for a broad spectrum is impossible to achieve as it depends on the wavelength of light. Moreover, the FL colloids were not completely optically homogeneous [87].

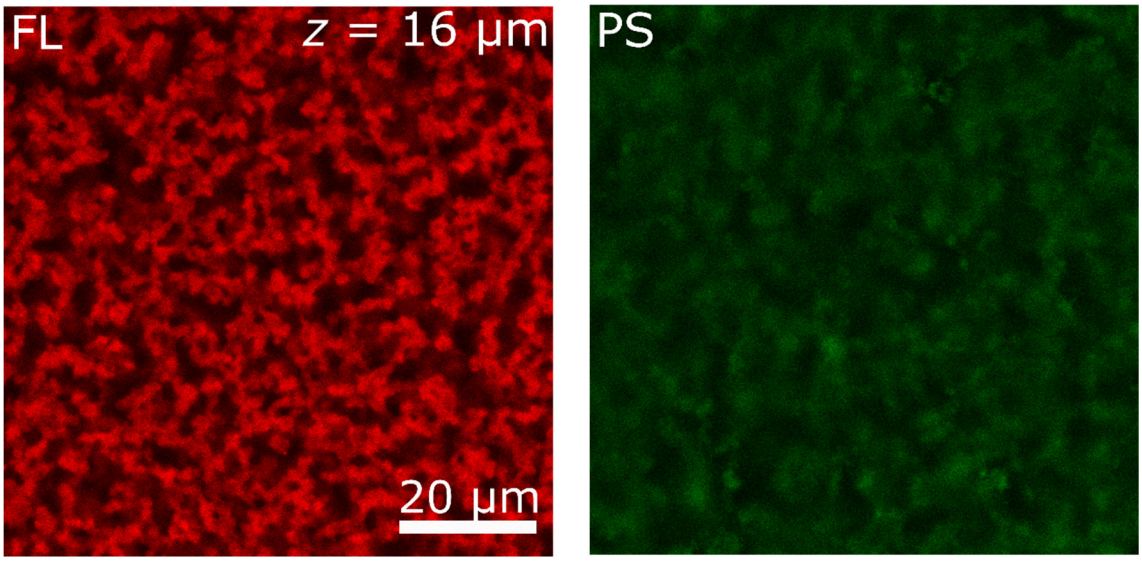

Figure 4.3. Confocal microscopy images of one component FL and PS gels at 10% v/v.

4.2 Core-shell Gels

In this part, multi-step kinetic self-assembly of bi-material colloidal gels was investigated. Using DNA strands with the same T spacer but different sticky ends with a lower T_m (**B** and **B'**, non-complementary to **A** or **A'**), it was possible to have a 'core' gel form first through **AA'** interaction and then a secondary gel condense onto it through **BB'** interaction.

4.2.1 FL as the Core Gel

The fluorinated core-gel colloids were made of two batches, one functionalised with **A**/**B** and the other with **A'**/**B**, using equimolar ratios of **A** to **B** and **A'** to **B**, respectively. The intra-species attraction between the fluorinated core colloids was purely due to **A** and **A'** hybridisation, while equally sized **B'**-coated PS particles could hybridise to the FL-core gel at lower temperatures (Figure 4.4).

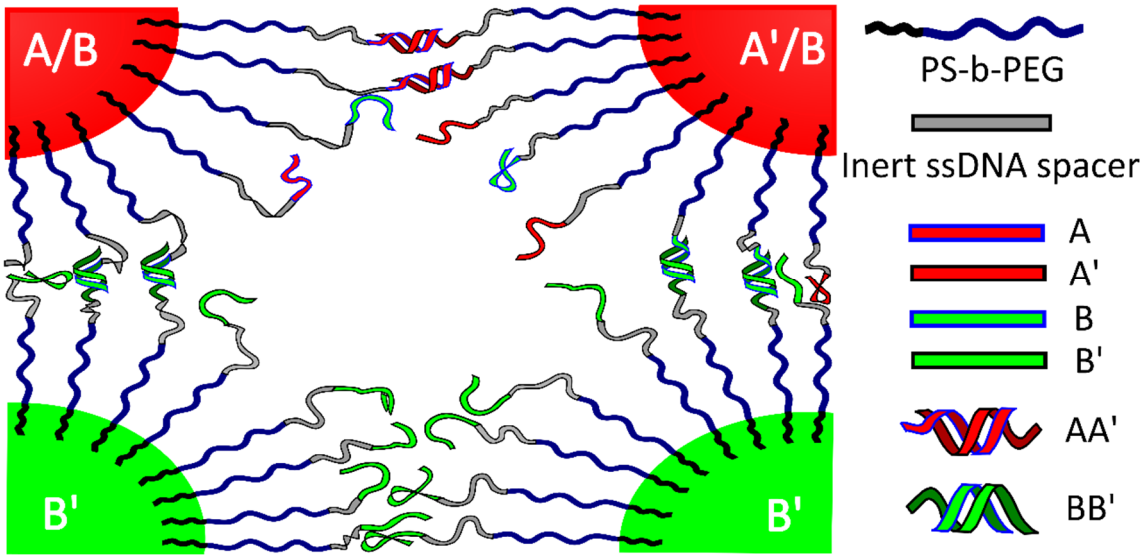

Figure 4.4. Cartoon explaining FL and PS particle coatings in core-shell gels. Red FL particles form a primary core gel first and green PS particles hybridise to the red gel at a lower temperature. A modified version of this figure appears in ref. [116] *and was created by the present author.*

For a one-to-one mixture of **A/B** and **A'/B** coated FL particles, the melting temperature was $T_{\mathrm{m}}(\mathrm{FL_{core}}) \approx 58$ °C. The **BB'** binding was tested using two batches of PS particles coated with **B'** and **B**, respectively: $T_{\mathrm{m}}(\mathrm{PS_{shell}}) \approx 45$ °C. Figure 4.5 b and c shows epifluorescence microscopy images of a core–shell sample, where the core consisted of 5% v/v (2.5% **A/B** and 2.5% **A'/B**) FL particles and 5% v/v PS (**B'**) particles. Hence, the total colloid volume fraction was 10%, well within the percolation limit [53]. After heating the sample to $T = 65$ °C, allowing the colloids to mix in the colloidal-gas phase, the sample was cooled below $T_{\mathrm{m}}(\mathrm{FL_{core}})$, triggering the hybridisation between the red fluorescent FL-particles. A percolating primary gel formed within a temperature range of 1–2 °C, in agreement with previous colloidal gelation experiments [107, 120]. The PS colloids remained in a gas phase, visible as green fluorescence occupying the regions depleted of FL particles (Figure 4.5 c middle). Further cooling below $T_{\mathrm{m}}(\mathrm{PS_{shell}})$

condensation of these green-fluorescent PS particles onto the primary gel was observed (Figure 4.5 c right).

Figure 4.5. Images of a FL_{core}-PS_{shell} colloidal bigel during cooling. a) Cartoon showing the binary FL–PS colloid mixture in the gas phase above $T_m(FL_{core})$ (left), slightly below $T_m(FL_{core})$ (middle) and below $T_m(PS_{shell})$ (right). Images created in Maya by Y. Lan.

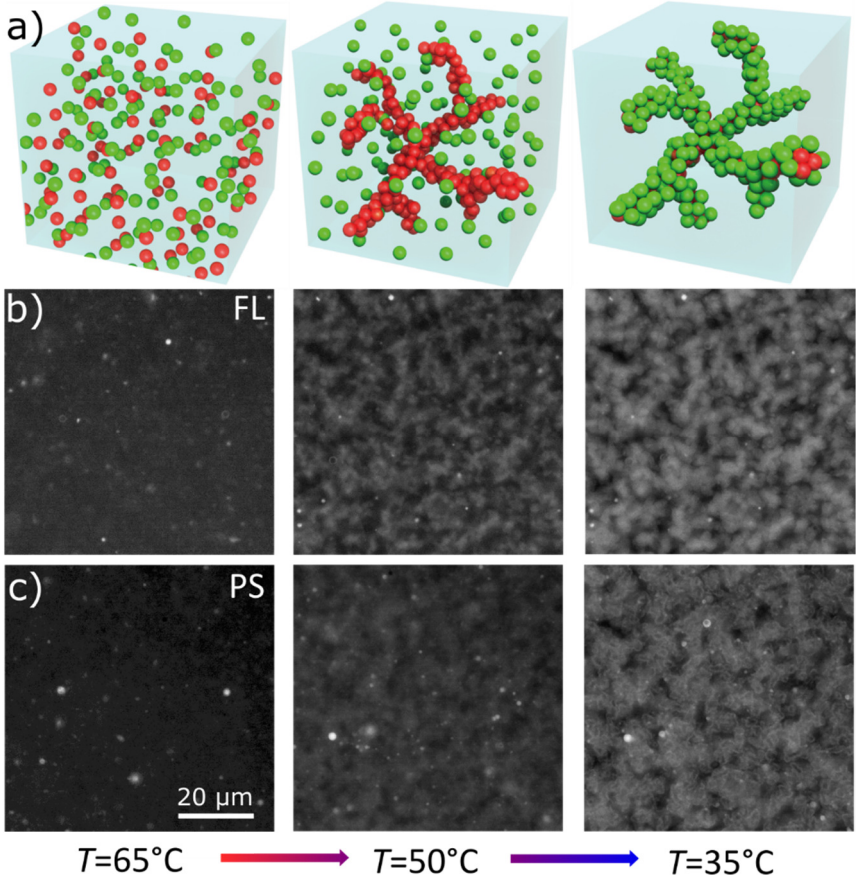

b) and c) Epifluorescence microscope images of FL_{core} (red-labelled, middle) and PS_{shell} (green-labelled, bottom) colloids at different stages of cooling. Figure appears in ref. [116] *and was created by the present author.*

Confocal microscopy z-stacks were then taken for this system in both fluorescence channels. Characteristic length-scales $\lambda(z)$ for the different components in the sample are shown in

Figure 4.6 (bottom). $\lambda(z)$ for the empty space and the gel were determined for the two fluorescence channels separately. A finer but denser structure for the $\mathrm{FL_{core}}$ gel at the bottom of the sample than at the top was seen, as observed in the single FL-gels, which is due to the higher density of the FL particles ($\rho_{HFBMA} = 1.345 \frac{\mathrm{g}}{\mathrm{cm}^3}, \rho_{styrene} =$

1.05 $\frac{g}{cm^3}$). In the gas phase, both PS and FL particles were homogeneously distributed,

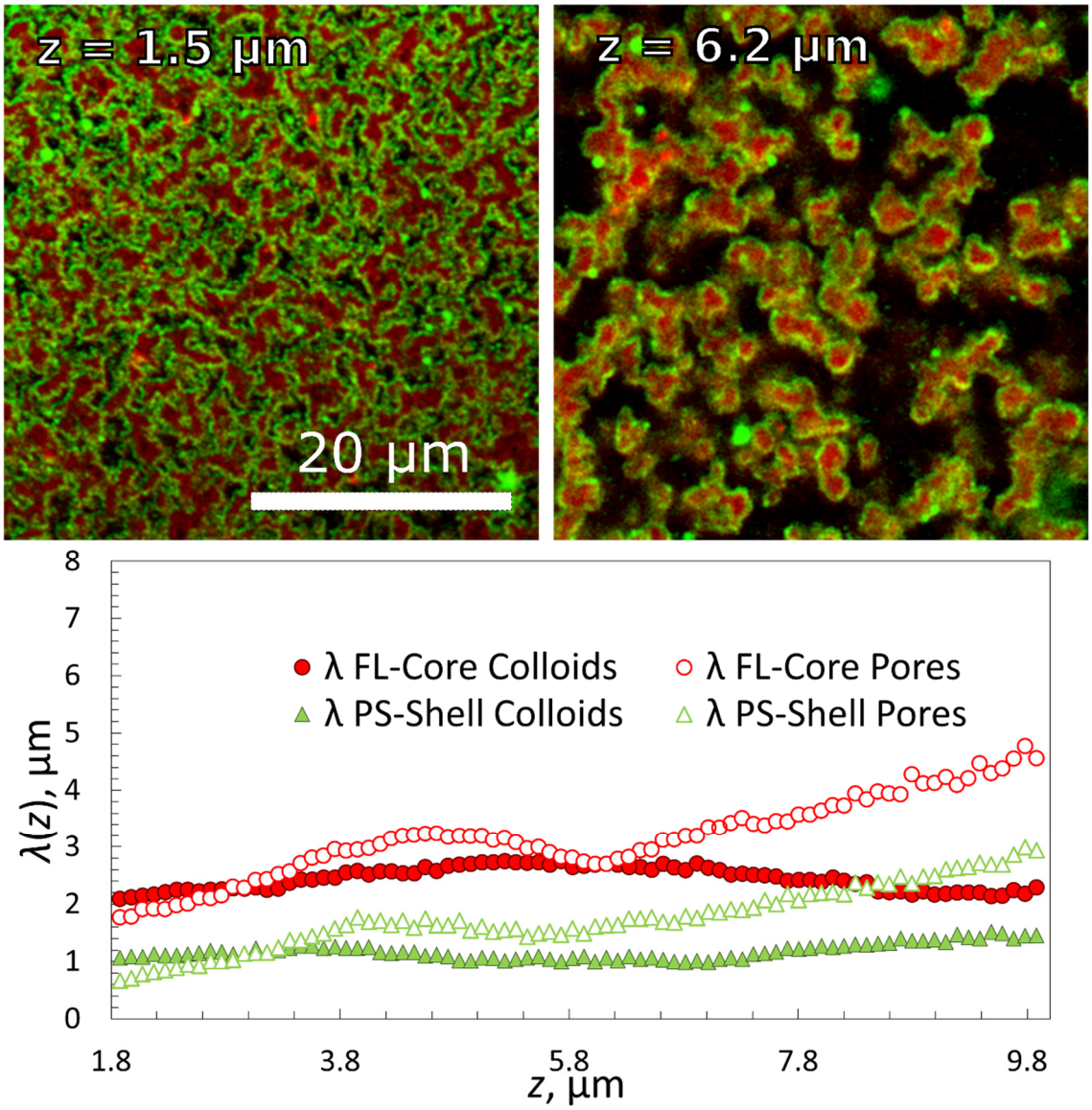

Figure 4.6. FL_{core}-PS_{shell} bigel in confocal microscopy. Top: overlaid confocal fluorescence images for two different heights of a 1:1 mixture of primary gel forming FL and coating PS particles with a total volume fraction of 10%. Bottom: characteristic length-scale, $\lambda(z)$, versus height z in the sample, extracted from chord analysis of the corresponding fluorescent images of the FL (red) and PS (green) system. Figure appears in ref. [116] *and was created by the present author.*

both having a similar gravimetric height of tens of microns. When quenched into the 2-phase region, small clusters formed immediately due to DNA hybridisation: spinodal decomposition happened. Increasingly larger clusters effectively felt a stronger gravitational pull than the individual particles and started sedimenting.

No full compression of the gel structure due to gravity was observed because the DNA bonds between clusters were strong enough to hold much of the open gel network. Evidently the thickness of the coating (solid green triangles in Figure 4.6 bottom) remained 1 μm throughout the sample, as the PS particles did not form clusters by themselves. Note that the PS-coating should be one particle thick [56], which would be 200 nm. However, this was below the diffraction limit of our setup. Nevertheless an apparent thickness of 1 μm was seen. This could have been due to both the limiting optical resolution and a possible 'surface-roughness' of the primary gel. Respectively, the sizes of the 'empty' pores were increasing with increasing height *z*.

4.2.2 PS as the Core Gel

In order to overcome the sedimentation effects, we inverted the system by reversing the DNA coating scheme such that the PS colloids formed the primary gel first (via **A/B** and **A'/B** coatings). Following the gelation of the PS core, condensation of the FL-particle coating took place, as the fluorinated particles had been functionalised with **B'** DNA. Epifluorescence images at different temperatures are shown in Figure 4.7.

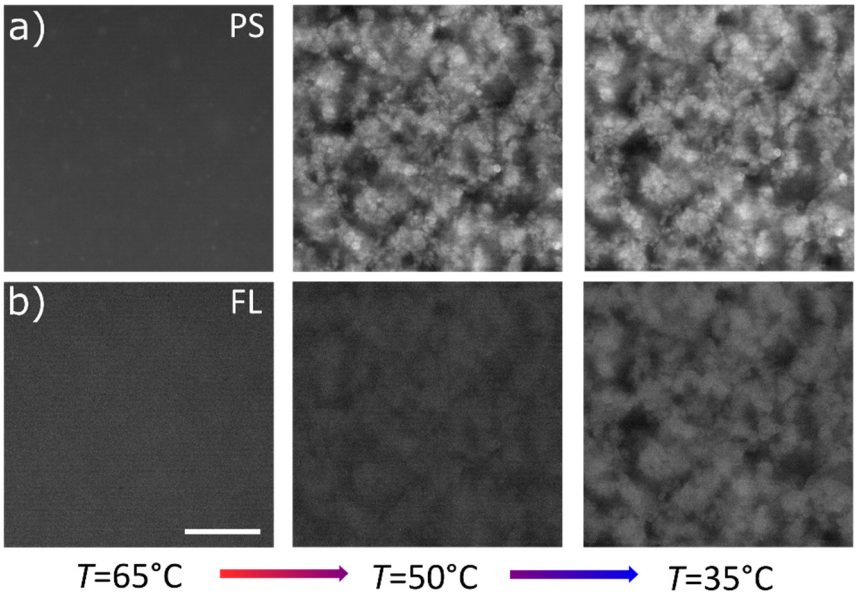

Figure 4.7. Epifluorescence microscopy images of a PS_{core}-FL_{shell} colloidal bigel during cooling. Figure appears in ref. [116] *and was created by the present author.*

The volume fractions were kept the same as in the previous sample: 5% v/v PS particles (2.5% **A/B** and 2.5% **A'/B**) and 5% v/v FL shell particles (**B'**), but in this case the PS particles had been density matched using 12% sucrose and also the fluorescence labels had been swapped so that the core remained red and the shell green. Confocal imaging

revealed that λ_{core} was now constant throughout the height of the structure as expected (Figure 4.8).

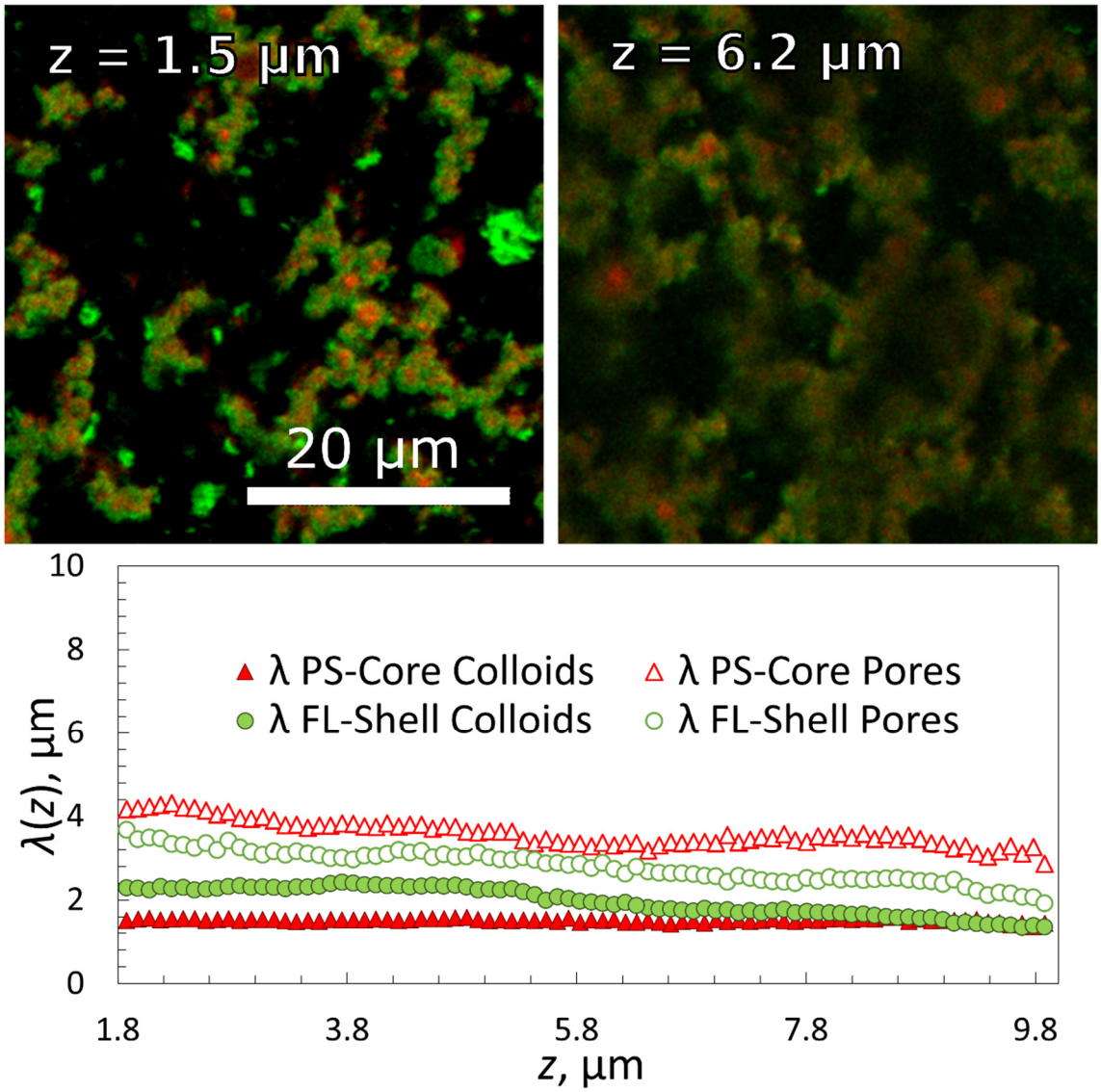

Figure 4.8. PS_{core}-FL_{shell} bigel in confocal microscopy. Top: overlaid confocal fluorescence images for two different heights of a 1:1 mixture of primary gel forming PS and coating FL particles with a total volume fraction of 10%. Bottom: characteristic length-scale, $\lambda(z)$, versus height z in the sample, extracted from chord analysis of the corresponding fluorescent images of the PS (red) and FL (green) system. Figure appears in ref. [116] *and was created by the present author.*

However, the coating thickness appeared to be larger – the green shell particles were covering most of the red particles in the sliced images, indicating an even higher 'interfacial roughness' of the primary structure. Interestingly, our group had shown in simulation studies and experiments that a complete coverage of the primary gel by a monolayer of 'condensed' colloids required a 1:1 colloid mixture as used in this study.

This explained the lack of any unbound colloids in solution at room temperature. But the difference in the apparent thickness of the coating remains to be studied in further detail in future. This result demonstrated the ability to form 3D gel networks with homogenous pore structure even though two very different types of colloidal materials were used. In particular, using the 'lighter' PS colloids as scaffolding material, it was still possible to distribute the more 'heavy' fluorinated particles evenly throughout the system, circumventing strong variations in the gel structure due to gravity.

4.3 Diffusion in a Gel Network

The diffusivity of free PS particles in the FL gel was also investigated at different heights above the sample-container surface, hence for different characteristic pore-sizes λ. The 420 nm diameter PS particles (labelled with green fluorescence) were coated with a non-complementary DNA brush with a 69 base-pair long double-stranded DNA as a spacer with no sticky overhang using the same swelling–deswelling method. The rod-like double stranded DNA has a persistence length of about 50 nm corresponding to 150 base pairs. Hence the steric layer was roughly 20 nm thick, giving the tracer particles an effective diameter of about 440 nm. The coating ensured the particles did not stick to the FL gel. These particles were used as tracers for diffusivity measurements with DDM. The FL gel (red-fluorescent) was prepared as before, with one heating–cooling cycle done before taking videos at room temperature. All samples contained 0.01% v/v tracer particles and 50 mM NaCl in TE buffer with 22% w/w sucrose, ensuring almost perfect refractive index-matching. The fluorescently labelled gel was characterised as before using confocal microscopy and chord analysis. Multiple one-minute videos were taken in green fluorescent mode of the tracer beads in all samples at different heights starting from the bottom of the sample chamber and analysed in MATLAB. From the decay time $\tau(q)$ versus the scattering wavevector q plots (Figure 4.9) the diffusivities of the tracer particles were extracted using the relation $\tau = (Dq^2)^{-1}$, where D is the diffusion constant. The theoretical result for the 440 nm large particles free in solution ($D_{\mathrm{free,theo}} = 4.5 \times 10^{13}\ \mathrm{m^2/s}$, taking into account the viscosity increase due to the dissolved sucrose) was close to the measured values (Figure 4.9 a). However, when dispersed in a 10% v/v FL gel, DDM measurements taken 10 μm above the bottom surface of the sample showed a clear reduction in the apparent diffusivity ($D_{\mathrm{app}} = 2.2 \times 10^{13}\ \mathrm{m^2/s}$) and a slight deviation from the q^{-2} behaviour. The relaxation times $\tau(q)$ of freely diffusing tracer particles (no gel) were fitted with a q^{-2} behaviour, while DDM measurements for

10 and 20 µm above the lower support surfaces could only be fitted with a slightly lower exponent, typically 1.6–1.8.

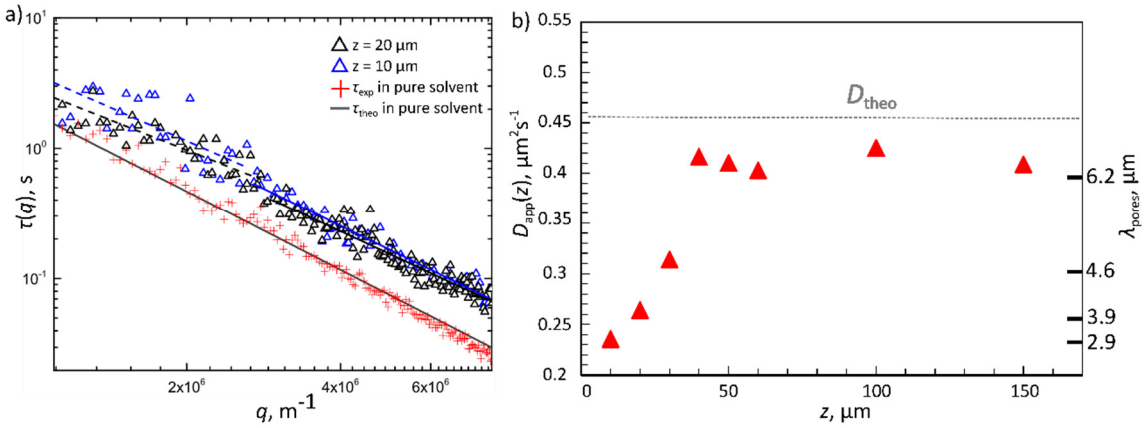

Figure 4.9. Diffusivity of tracers inside FL gel pores. Decay time $\tau(q)$ as a function of the scattering vector q extracted from DDM analysis for 420 nm PS tracers in a 10% FL gel in 22% sucrose solution at different heights z and their corresponding fits (solid and dashed lines). The theoretical value is given by the relation $\tau = (Dq^2)^{-1}$ (grey line). b) Apparent diffusion coefficient $D_{app}(z)$ of the tracers versus the height z in the sample. The measured $D_{app}(z)$ are also plotted with the corresponding FL gel pore sizes λ_{pores} at different heights. Figure appears in modified form in ref. [116] *and was created by the present author.*

This was in agreement with both theoretical predictions [121] and recent experimental studies by Cervantes-Martínez et al. [122] in which the diffusion of a single particle confined inside a water droplet suspended in oil was measured as function of droplet size. Deviations from bulk diffusion due to long-ranged hydrodynamic interactions with the confining walls were observed in their system as well. These hydrodynamic interactions became increasingly apparent as the confinement – in this case, the average pore size – became smaller. Figure 4.9 b shows the apparent diffusion coefficient for different heights z away from the bottom surface, together with the corresponding characteristic pore sizes λ_{pores} measured in the same sample. At z = 40 µm, the apparent diffusion coefficient reached values similar to that of the freely diffusing tracer particle. At this height λ = 6.2 µm, hence the average pore sizes are about 15 times larger than the diameter of the tracer particles, in good agreement with the theoretical predictions [121, 122]. Finally, it is interesting that D_{app} almost but not quite reached the free diffusion coefficient, supporting that the FL-network appears evenly dense in the range of z = 40–150 µm, and that even at this mild confinement the tracer particles still feel the confining environment.

4.4 Conclusions and Outlook

This study demonstrated the ability to create optically transparent dense colloidal gels by functionalizing fluorinated latex (FL) particles with DNA using an adapted swelling–deswelling method. Using sucrose to refractive index-match our fluorinated colloids in aqueous media enabled imaging such gels made of 200 nm diameter particles at 10% volume fraction up to ~70 μm deep into the sample, compared to only ~15 μm for similarly sized polystyrene (PS) particle gels. In order to overcome the fact that the FL particles have much higher density than the solution leading to sedimentation affecting the resulting gel structure, the lighter PS colloids were employed as a primary gel 'scaffold' onto which the FL particles could be condensed. Thus it was possible to make spatially homogeneous colloidal gels. The final part of this project demonstrated the ability to track PS-tracer beads inside a refractive index-matched FL gel, obtaining diffusivity data using Differential Dynamic Microscopy.

5 DNA-COATED FUNCTIONAL OIL DROPLETS

Many industrial soft materials, such as paints, foods and pharmaceutical products often contain oil-in-water (O/W) emulsions at the core of their formulations [123]. Emulsions are also used as templates for advanced materials fabrication [124, 125]. If the surfactant or particle employed to stabilise the interface between water and oil is responsive to external stimuli such as temperature, pH or light, O/W emulsions can effectively be used as reconfigurable fluids while the oil droplets can be thought of as 'soft colloids' [126–128]. The unique property of oil droplets with surfactants on the surface is their natural 'patchiness' due to the mobility of the linkers on the interface, which in turn allows for programmed sequential self-assembly of the building blocks [129]. Much like with hard colloidal particles, DNA has been used to functionalise such soft surfaces; by choosing a suitable combination of surfactants and ligands, DNA-coated O/W emulsions [130–132] and vesicles [133, 134] have been made.

However, up until now, DNA-functionalised emulsion droplets have had relatively low coating densities and the yields have been expensive to scale up. This chapter presents work on a general O/W DNA-coating method using functional non-ionic amphiphilic block copolymers, both diblock (PS-b-PEG) and triblock (Synperonic PEG-b-PPO-b-PEG). The surfactants were functionalised with azides, much like the ones used for hard colloids, however, using commercially available and relatively inexpensive Synperonic triblock copolymers allowed for large quantities of droplets being manufactured. Different production methods, including ultrasonication, microfluidics and membrane emulsification were used with different oils (hexadecane and silicone oil) to produce functional droplets in various size ranges (200-1000 nm, ~20 μm and > 50 μm), exemplifying the generality of the protocol. This work demonstrates thermally reversible sub-micron emulsion gels, hierarchical 'raspberry' droplets and controlled droplet release from a flat DNA-coated surface. The emulsion stability and polydispersity were evaluated using DLS and optical microscopy. The generality and simplicity of the method opens up new applications in soft matter, biotechnological research and industrial advances.

The text of this chapter is adapted from the manuscript in reference [135] written by A. Caciagli, E. Eiser and the present author. Microfluidics experiments were performed together with A. Levin and A. Caciagli, all other experimental parts were done together with A. Cagiagli.

5.1 Oil Droplet Coating

Recent work in our group on functional oil droplets (ODs) by D. Joshi et al. [132] served as an inspiration for many initial experiments performed on this new class of ODs. The original protocol for coating ODs with DNA involved using a microfluidic T-junction device to form sodium dodecyl sulphate (SDS)-stabilised silicone oil (50 cSt) droplets, then attaching a linker molecule, polylysine-g[3.5]–polyethylene glycol–biotin (PLL-PEG-biotin), to the negatively charged surface of the ODs through electrostatics. After this step, the droplets had biotin at the ends of the PEG chains sticking out of their surface, and biotinylated DNA could be attached to them through streptavidin, a host molecule for biotin, which would add two more steps to the coating protocol. While being a reliable coating method, it suffered from sensitivity to pH and salinity of the buffer (PLL-PEG-bio adsorption to the SDS being a purely electrostatic interaction), comparably low coating densities due to the size of the linker molecules ($M_{w(biotin)}$ = 244.31 g/mol $M_{w(streptavidin)}$ = 55,000 g/mol) and a relatively cumbersome coating procedure involving many steps.

Another option would have been to use cholesterol anchors [129, 131], however, the materials proved to be very expensive, and it was decided to apply the knowledge gained from coating hard colloidal spheres with di-block copolymers to coating ODs. Di- and tri-block copolymers with hydrophilic chain(s) of poly(ethylene) glycol (PEG) were therefore employed as non-ionic surfactants, stabilising the droplets. These classes of surfactants offered some advantages over ionic surfactants such as sodium dodecyl sulphate (SDS): they were less sensitive to the presence of electrolytes [136], allowed for easier formulations due to the ability to systematically tune the emulsifiers' polarity [136] and offered enhanced emulsion stability to the interfacial film between approaching droplets, preventing their coalescence [136]. Moreover, these non-ionic block copolymers showed a much higher chemical stability.

Both diblock ($PS_{(30)}$-b-$PEG_{(79)}$-N_3, synthesised by C. Mugemana and N. Bruns, see Appendices) and triblock (N_3-PEG-PPO-PEG-N_3 (Synperonic F108-N_3), functionalised with azides in-house, see Chapter 2.3.1) were employed in this study, emphasizing the

generality of the protocol. The choice between the former and the latter depended on the desired emulsion properties such as size distribution, stability, DNA strand density on the surface and cost of production, but was irrelevant to the success of the protocol. The DBCO-DNA strands used in this work were the same as in Chapter 4 (**A** and **A'** oligomers).

The procedure for droplet formation and functionalisation is sketched in Figure 5.1. First, the azide-functionalised block copolymer (Figure 5.1 a) was dispersed in deionised water - emulsification was achieved according to one of the three chosen strategies detailed later in this text. In the resulting droplets the hydrophobic block of the polymer acted as an anchor in the oil phase, while the hydrophilic PEG-N_3 segment stretched into the water phase forming a sterically stabilising dense brush (Figure 5.1 c, d). Finally, the single DBCO-DNA strands were attached to the N_3 ends of the block copolymers via a strain-promoted alkyne-azide click reaction (SPAAC) (Figure 5.1 d). The success of this functionalisation strategy was demonstrated by confocal microscopy on emulsion droplets for which the DBCO-DNA strands were replaced by fluorescently labelled DBCO-Cy5 (Figure 5.1 f).

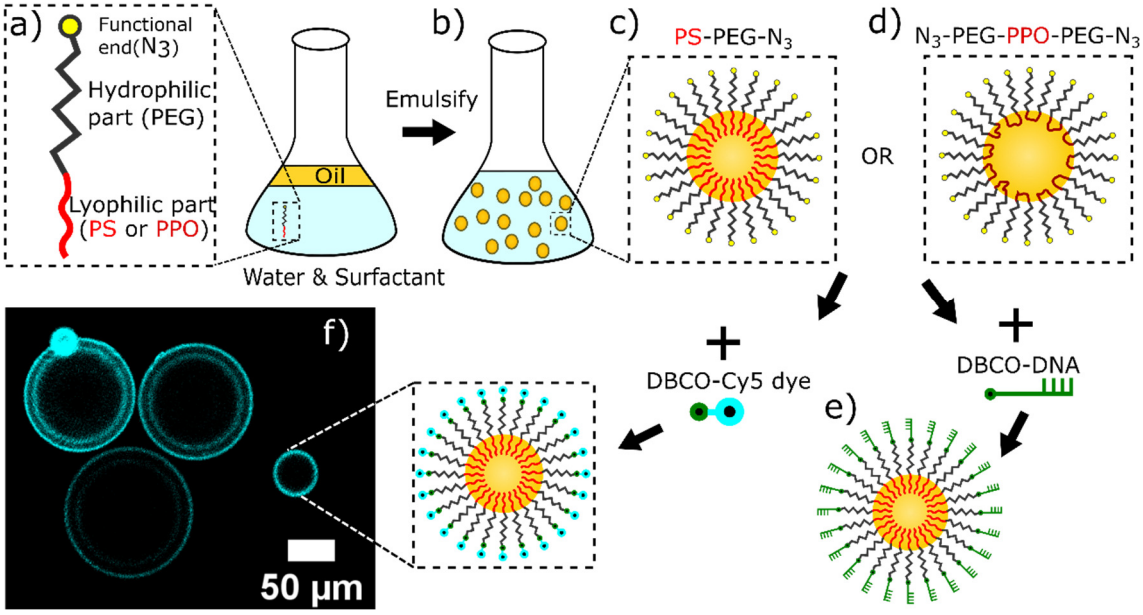

Figure 5.1. Cartoon detailing functional OD production. a) Amphiphilic non-ionic surfactant. b) Emulsification. c) OD coated with PS-PEG-N_3. d) OD coated with N_3-PEG-PPO-PEG-N_3. e) DNA-coated OD. f) Confocal microscopy image of Cy-5 dye-coated ODs. Modified figure appears in ref. [135] and was created by the present author.

At this point the reader should have noticed that the droplets in Figure 5.1 f) exhibited two fluorescence rings rather than one. We believe that this was an optical effect rather

than a result of a double emulsion – as the droplets were at the top of the sample change, the fluorescence is thought to have been reflected by the glass wall and refocused by the droplets themselves. The first point in support of this statement is that the droplets did not show any sign of having a 'shell' in brightfield microscopy. The second point is that the rings only appeared at a certain point of focus for a droplet of a given size and not throughout the droplet, as what would happen if the azides were present on both sides of the interface.

Coming back to DNA, as this functionalisation method had proven to reliably produce high-density DNA coatings on hard colloids, owing to a small grafting point and the high yield of the SPAAC reaction, the OD azide coating density was also checked. Fluorescence assays were performed on silicone oil droplets, produced in a microfluidic device ($PS_{(30)}$-b-$PEG_{(79)}$-N_3 coating), were reacted with a DBCO-Cy5 fluorescent dye overnight (more details on assays in Chapter 2.4.5). The droplets were left to float to the top of the tube under gravity, while the underlying buffer's fluorescence was then compared to a series of standard fluorescence solutions. As the size and the volume fraction of the droplets were known, an estimate of the surface coverage was obtained to be ~70,000 azide ends per μm^2, a sevenfold increase over the streptavidin-coated droplets of Joshi et al. [132].

5.2 Emulsification Methods

The emulsion droplets were produced by three different emulsification methods: membrane emulsification [137, 138], microfluidics and ultrasonication [139]. The first two methods produce macro-emulsions, with the droplet size being larger than 1 μm, differing in volume throughputs [140, 141], while the third produces typically nano-emulsions (droplet size on the order of a few hundred nanometers) [142, 143]. Together they span a wide range of emulsion characteristics and sizes, which constitutes a good benchmark for the generality of this protocol. For each method, two combinations of oil and surfactant were chosen: hexadecane with a custom $PS_{(30)}$-b-$PEG_{(79)}$-N_3 diblock copolymer, and silicone oil with a commercial triblock copolymer (N_3-PEG-PPO-PEG-N_3: Synperonic F108-N_3). Figure 5.2 summarises the methods.

The membrane emulsifier produced a slightly polydisperse emulsion according to the method's typical yield [137]. A lower polydispersity was achieved using the F108/silicone oil combination. Rather than an effect of the surfactant, this improved monodispersity was due to the higher viscosity ratio between dispersed and continuous

phase, which decreased the supply of the dispersed phase during droplet formation, resulting in smaller droplets [144, 145]. The droplets were stable against coalescence for months, with a slight broadening of the size distribution over time due to Ostwald ripening [146], a process whereby the dispersed phase diffuses between droplets through the dispersion medium as a consequence of chemical potential gradients (see Figure 5.3 and Appendices).

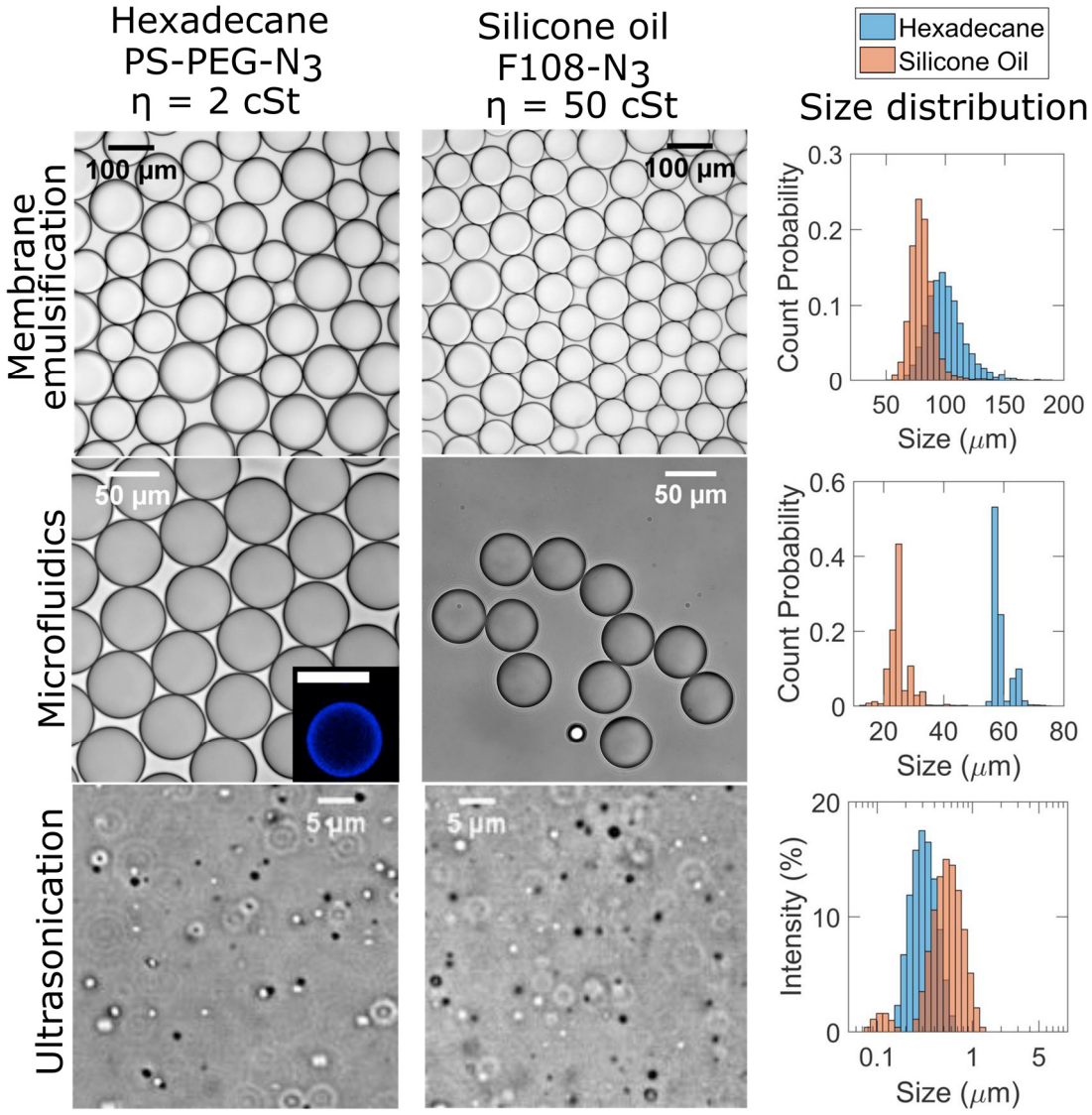

Figure 5.2. Comparison of functional droplets produced by different emulsification methods. The images were obtained by brightfield optical microscopy. The inset in the hexadecane column, microfluidics row was obtained by confocal microscopy. The size distributions for membrane emulsification and microfluidics were obtained by image analysis, whereas that for ultrasonication was obtained by DLS. Figure appears in modified form in ref. [135] and was created by the present author.

In particular, smaller droplets exhibit a higher Laplace pressure and therefore a higher chemical potential. The overall Gibbs free energy of the system lowers as the small droplets dissolve in favour of the larger ones, shifting the size distribution to larger values over time. The diffusion occurs due to the finite solubility of the one liquid phase in another and can be slowed or stopped if the dispersed phase, here the oil, is composed of a compound insoluble in the continuous phase.

Droplets produced by microfluidics were very monodisperse with polydispersity index (PDI) of less than ~10% (Appendices). The diblock copolymer/hexadecane combination produced larger droplets, possibly due to the lower viscosity ratio between the dispersed and continuous phases, and of slightly better quality, due to faster kinetics of surfactant adsorption at the interface. The fast kinetics can be explain by two effects: first, the adsorption is faster for lower viscosity ratios between the dispersed and continuous phase, which favours the hexadecane system; second, although triblock copolymers have a greater interfacial anchoring strength than diblock copolymers of the same geometry, their diffusion is slower due to their larger size [147]. This again favoured the hexadecane system. For both systems, however, droplet stability was very good and provided a longer life time and resistance to coalescence at higher temperatures (Figure 5.3, Appendices).

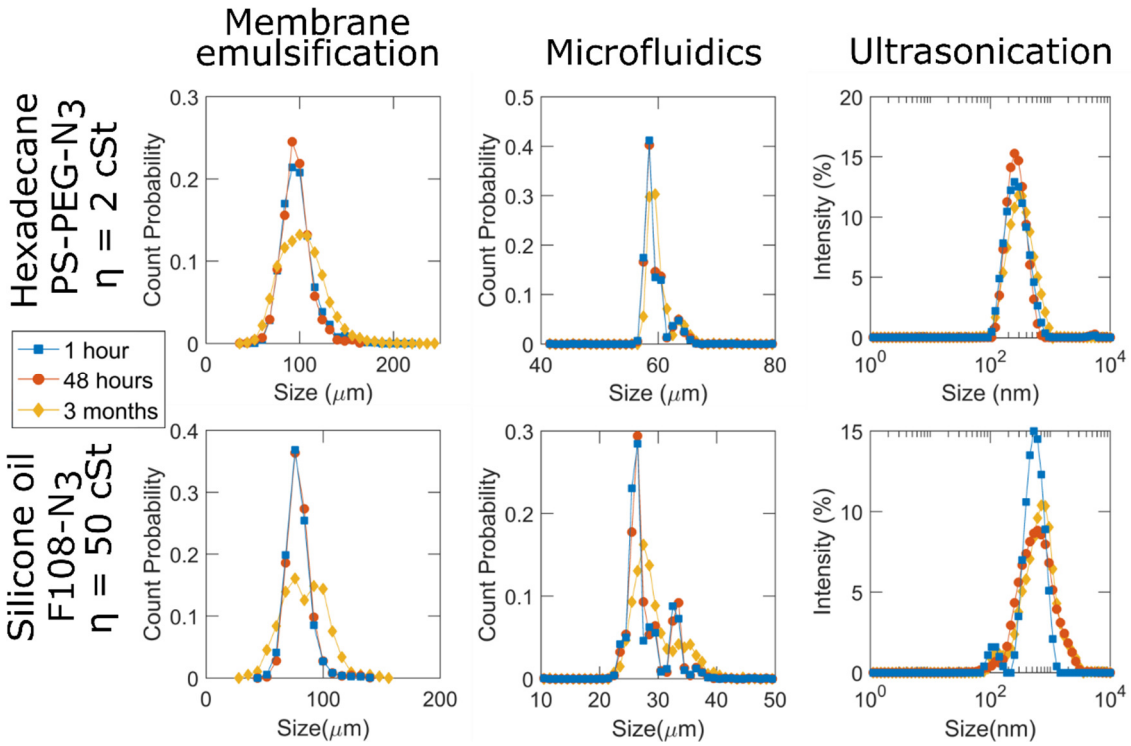

Figure 5.3. Oil droplet stability over time: size distributions. Figure appears in modified form in ref. [135] and was created by A. Caciagli.

The ultrasonication emulsification strategy produced a more polydisperse nano-emulsion, which is typical for the method [143]. While it was not attempted, future work might achieve a more narrow size distribution after fine-tuning the overall procedure [148, 149]. The diblock copolymer/hexadecane combination again yielded superior quality droplets (smaller and more monodisperse), which can be explained using the same arguments given in the microfluidics case. As was the case for the membrane emulsification droplets, these emulsions showed a slight broadening of the size distribution over time due to Ostwald ripening (Figure 5.3).

In summary, for all the three emulsification methods studied, the emulsions showed excellent stability against coalescence. Membrane emulsification and ultrasonication droplets showed a slight broadening of the size distribution due to Ostwald ripening over long shelf times, though the rate was relatively slow. While both oil/surfactant combinations produced excellent droplet quality, the diblock/hexadecane combination gave a better PDI: this was explained by a more favourable surfactant/oil interaction (silicone oils are known to require silicone surfactant for the best performance [150]).

5.3 Functional ODs

To show the possibility of using the ODs as microscale building blocks, three different experiments were performed. In the first one, 'raspberry droplets' were constructed. The 60 μm large 'core' silicone oil droplets were prepared in a membrane emulsifier (Chapter 2.3.3) and stabilised by **A**-PEG-PPO-PEG-**A** (F108-**A**) DNA (the same DNA strands as in Chapter 4, coating protocol in Chapter 2.3.5). The small droplets were made with the ultrasonic probe and functionalised with the complementary **A'** DNA (hexadecane PS-PEG-**A'**); the latter had a range of sizes from about 200 nm to 5 μm. A small amount of BODIPY 505/515 fluorescent dye was added to these hexadecane droplets to make them fluorescent. After mixing the two populations of droplets in PBS (50 mM NaCl) in a flat capillary and incubating the samples at room temperature for 15 minutes (well below the melting temperature for the **AA'** bond, see Chapter 4), optical microscopy was performed (Figure 5.4).

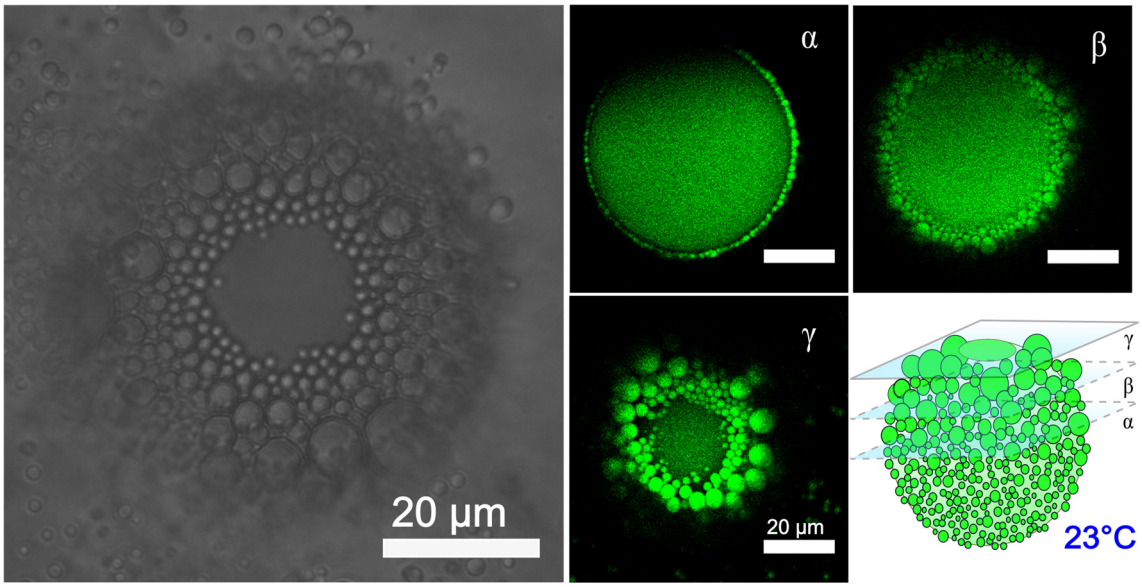

*Figure 5.4. 'Raspberry droplets'. Left: optical microscopy image of 'small' ultrasonically produced hexadecane PS-PEG-**A'** droplets connected to 'big' membrane-emulsified silicone oil F108-**A** drops. Right: the same system imaged by confocal scanning fluorescence microscopy at different heights, as shown bottom-right. Figure appears in modified form in ref. [135] and was created by the present author.*

The microscopy revealed raspberry-like composite droplets, with the small drops anchored to the large ones owing to the **AA'** DNA hybridisation. Utilising the specific **AA'** DNA binding prevented the small and large droplets from binding to each other at all temperatures between 5 °C and 90 °C, as **AA** or **A'A'** bonds were forbidden -the same system was used in Chapter 4. More droplets were found at the top of the big drops due to buoyant forces caused by hexadecane's density (770 kg/m³) that is lower than that of the aqueous buffer solution. Moreover, it was seen that although the dense PEG-DNA-PEG sandwich between the small and large ODs prevented the droplets from coalescing, the initially fluorophore-free large OD became slightly fluorescently active as well. This suggests that the hydrophobic BODIPY dye was able to diffuse across the surfactant barrier, possibly due to the osmotic-pressure driven Ostwald ripening.

In the second experiment, two batches of ultrasonicated hexadecane droplets (one stabilised via PS-PEG-**A** DNA and the other via PS-PEG-**A'** DNA) were mixed in a flat capillary at a total oil concentration of 5% v/v and then imaged. The sample was heated to 70 °C, above the melt temperature of the **AA'** bond ($T_m \approx 65$ °C), held there for 15 minutes and then cooled down to the two-phase region in which the complementary DNA strands started to bind. A cooling rate of 1 °C/min was used to ensure equilibrium DNA hybridisation. The resulting droplet aggregates, shown in Figure 5.5 a centre, resemble

those of gels made of DNA-coated colloids of similarly sized hard polystyrene particles (Figure 5.5 a right, see Chapter 3 for coating details), however, these colloidal gels displayed a lower melting temperature of ~ 60 °C. To understand this difference in T_m one should consider the fact that the melting transition of colloids densely coated with complementary ssDNA is as sharp as 1-2 °C (see Chapter 1.2.2). This is because several **AA'** pairs can form in the contact region and therefore T_m increases logarithmically with the increasing total number of possible hydrogen bonds that can form between the ssDNA pairs and the transition sharpens as well (see Figure 1.5). Hence a possible reason for the difference in T_m between colloidal gels and emulsion droplets is the mobility of the ssDNA on the OD interface that allows for an even tighter rearrangement of DNA in the contact region once two droplets meet. Furthermore, the gain in binding energy also allows the soft ODs to flatten, thus leading to a slightly increased effective size of the contact patch and therefore a higher binding strength – this increase is only limited by the cost to deform the interface [131].

Note that the binding energy of a single **AA'** pair is about 16 $k_B T$. Hard polystyrene colloids do not allow for surface deformation and DNA strands attached to their surface are not mobile. These 'emulsion gels' were completely thermally reversible over 5 heating-cooling cycles, showing a narrow melting region of ΔT ~ 2 °C and a sharp melt temperature, similar to the PS colloidal gel. Remarkably, no measurable coalescence was observed.

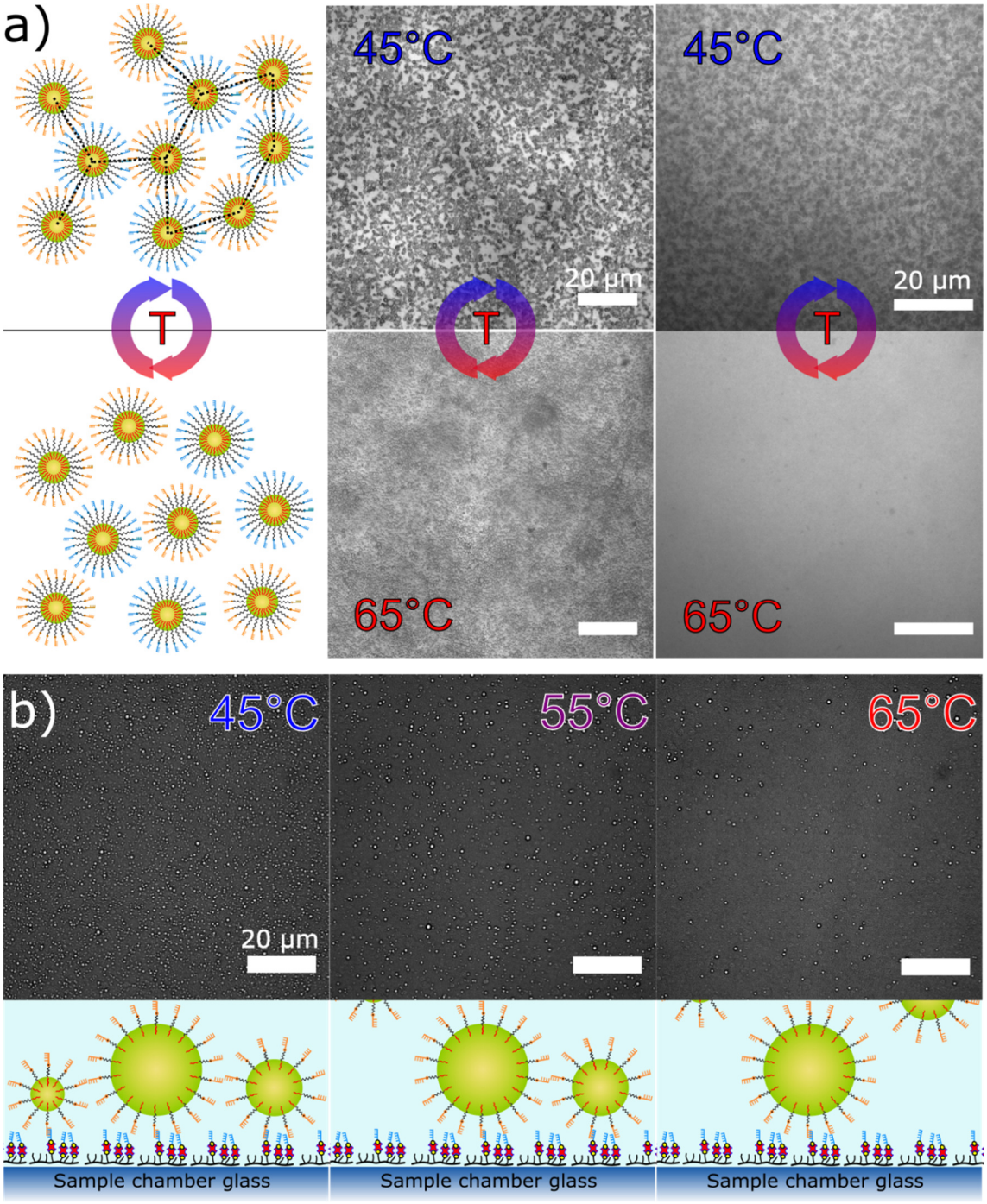

*Figure 5.5. Droplet gels and thermally activated release from a flat surface. a), left: a cartoon of a gel below and a gas above T_m. a), centre: a thermal cycle of ultrasonicated droplets (half with PS-PEG-**A**, half with PS-PEG-**A'**) showing an emulsion gel behaving as in the cartoon. a), right: corresponding measurement of 420 nm large PS colloids, half coated with F108-**A** and the other with F108-**A'** DNA. b) Optical microscopy image of a flat, **A** DNA coated glass surface to which ultrasonicated hexadecane droplets with PS-PEG-**A'** DNA were hybridised at T = 45 °C. With increasing T the droplets melted off progressively, with the smaller droplets being released first. Figure appears in modified form in ref. [135] and was created by E. Eiser and the present author.*

The third experiment demonstrated that the same hexadecane droplets could be DNA-anchored to a flat surface and then released in a controlled manner. As a number of chemical and pharmaceutical compounds are soluble in oil but insoluble in water, this system is a good model for those applications. There the surface of a flat capillary was first coated with **A** DNA using a grafting method via the comb-polymer PLL-PEG-biotin, described by T. Yanagishima et al. [151]. The positively charged poly(lysine) backbone adsorbed to the plasma-treated negatively charged glass surface (Figure 5.5 b bottom). Streptavidin was then used to bind biotinylated **A** DNA to PLL-PEG-biotin on the surface. After flushing the capillary 5 times with pure buffer solution, it was injected with a solution containing 1% v/v PS-PEG **A'**-functionalised ultrasonically-produced hexadecane droplets at room temperature. The sample was then heated to 70 °C, inverted and cooled down to coat the bottom surface with droplets such that imaging with an inverted optical microscope was possible. Imaging the sample showed how the buoyant ODs detached and rose upon heating (Figure 5.5 b). Although a clear release of the ODs from the surface was observed, the melting region was larger than that for hard-colloidal gels because of the much larger size-distribution of the ODs: The smaller ODs were released first as their effective contact area with the flat support surface was smaller, which is visible in the microscope images. In addition, the surface coverage of DNA of the flat capillary was estimated to be a lot lower than that of the ODs, contributing to a broadened melting transition.

5.4 Conclusions and Outlook

This work demonstrated a simple method to make oil-in-water emulsion droplets functionalised with DNA. The method is applicable to virtually all emulsification strategies since the functionalisation is carried directly on the surfactant. Furthermore, it is suitable for any non-ionic surfactant containing a hydrophilic PEO chain and any oil that can be emulsified by this class of surfactants (or a mixture containing at least one of them), making it very scalable. The self-organization properties conferred by the specific, DNA-mediated interaction were demonstrated by creating hierarchical droplet structures ("raspberry droplets") and a thermo-responsive emulsion gel. Moreover, our DNA-functionalised OD formulation showed a simple surface-controlled release system.

These properties open new routes toward the realisation of hierarchic self-assembly of micro-reactors that can be loaded with various chemical or other compounds such as nanoparticles and polymers [152, 153]. Such compartmentalised formulations are of great

interest in prolonging the shelf-life of emulsions relevant in pharmaceuticals and foods. In contrast to patchy colloidal particles with static linkers, the mobile linkers on emulsion droplets ensure progress toward the thermodynamic equilibrium of the self-assembly process without the need to anneal the colloids at a very narrow temperature range [154]. The scalability and simplicity of the protocol enables batch production of colloidal particles with specific valency and represent a huge step towards the bulk realisation of "colloidal molecules" [155]. Through careful design of the DNA-mediated interactions between droplets, emulsion gels with exotic properties could be realised such as fluids which harden upon heating or emulsions with tuneable porous morphologies conferring novel optical properties [156, 157]. In addition, the possibility to exert a direct control over the droplet/droplet interactions (thus tuning the "effective" friction between objects) makes these functional ODs appealing for the study of granular materials. Coupling the compartmentalisation capability of emulsions with the sensitivity to environmental stimuli such as temperature, this system could be used as a highly efficient microreactor or as an advanced drug and cargo delivery system, with broad applications in soft matter, medical and biotechnological research.

6 Fluorinated Latex Particle Photonic Crystals

Structural colour is the term used when the apparent colour of an object is produced due to light interacting with the object's microstructure. The features of said microstructure should be comparable to the wavelength of the incoming light: most biological structural colour arises due to coherent scattering by micro- or nanostructures with a corresponding variation in refractive index [158]. Such structures are very common in nature, and rely on a variety of mechanisms, including incoherent scattering, coherent scattering by crystalline structures and photonic glasses, and thin film interference. Opals, peacock feathers and butterfly wings are all examples of colour arising due to nanostructure rather than pigment.

Colloidal particles have been shown to self-assemble into crystalline structures [50, 51, 159, 160]. These crystals have enabled studying the underlying physics behind the self-assembly process and also allowed for designing systems with controllable optical, mechanical and electronic properties [161–163].

'Hard' spheres – particles with short range weak interparticle interactions – can form face-centred cubic (FCC), hexagonal close-packed (HCP), or random hexagonal close-packed crystal structures [110, 164]. On the other hand, 'soft' spheres that possess long range interparticle interactions can form FCC, body-centred cubic (BCC) and other lattices depending on the strength of the interparticle potential [165, 166]. Attaching long polymers to nanoparticles can also 'soften' the hard spheres [167].

The type lattice as well as the size and refractive index contrast against the continuous background of the colloids govern the optical features of these photonic crystals. It was previously shown that close-packed lattices such as FCC could not open a full bandgap regardless of the refractive indices of the medium and colloids [168]. This means that colloids ordered in an FCC lattice do not have an omnidirectional optical stop band; nevertheless, strong reflections can be observed at certain angles [169]. The refractive

index difference, Δn , between the colloid and the surrounding medium is another essential parameter when designing a photonic crystal. According to Finlayson et al., the strength of the reflection in photonic crystals is expected to have a Δn^2 dependence due to Fresnel reflections, but the distortions in the lattice structure and the size distribution of the colloids change this dependence to a linear one [170]. Moreover, for $\Delta n = 0.05$, the reflectance from the solid colloidal photonic crystals is < 10%, accompanied by a strong angle dependence, as also shown by Lai et al. [171]. Therefore, satisfying the transmission and reflection requirements over a broad angle at the same time is a significant challenge.

This chapter proposes designing liquid photonic crystals made of fluorinated latex (FL) particles to realise high transparency and strong reflection at the same time. FL particles (Chapter 3.1, Chapter 4) are the perfect choice: they have a low refractive index (1.36-1.37), their diameter is ~200 nm accompanied by very low size distribution (~1%) and strong negative zeta-potential reaching -82 mV. This work shows that these charged colloids formed almost transparent Wigner crystals and glassy structures in water with tuneable interparticle distances. These photonic crystals exhibited narrow-band blue, green, and red reflections depending on the concentration of the colloids. The results were further compared with electromagnetic simulations and confirmed that the 3D photonic crystals were capable of reflecting the light at certain wavelengths very strongly despite the really low refractive index difference. The absence of angle dependent reflection colour indicates that these samples contained multiple domains of photonic crystals having similar lattice constants providing a relatively narrow reflection bandwidth.

The results of this chapter were the outcome of a collaborative effort of T. Erdem, T. J. O'Neill, A. Caciagli, E. Eiser and the present author. T. Erdem and A. Caciagli performed the electromagnetic simulations, T. J. O'Neill, P. Xu, P. Boesecke and E. Eiser did the SAXS measurements while the rest of the experimental procedures were done by T. Erdem, T. J. O'Neill and the present author. The manuscript that is based on this chapter has been submitted to *Materials Horizons* [172] and is available on arxiv::1808.06260 (2018).

6.1 Particle Synthesis and Characterisation

The fluorinated latex (FL) particles were synthesised using emulsion polymerisation (Chapter 2.1.1 and Chapter 3). They had a hydrodynamic diameter of ~ 193 nm as measured by DLS, with a polydispersity index of 1.6 %, while from SEM measurements we found a much reduced diameter of (160 ± 25 nm) and a particle-to-particle distance

of (166 ± 0.7) nm (Figure 6.1 a inset). Although a size reduction in electron microscopy is expected due to DLS measuring the hydrodynamic size, the difference of the calculated size based on these two methods was so large that while drying these particles may have been strongly shrinking and deforming. In fact, FL particles, as confirmed by Koenderink et al. [87], do deform under electron microscopy and aggregate upon contact.

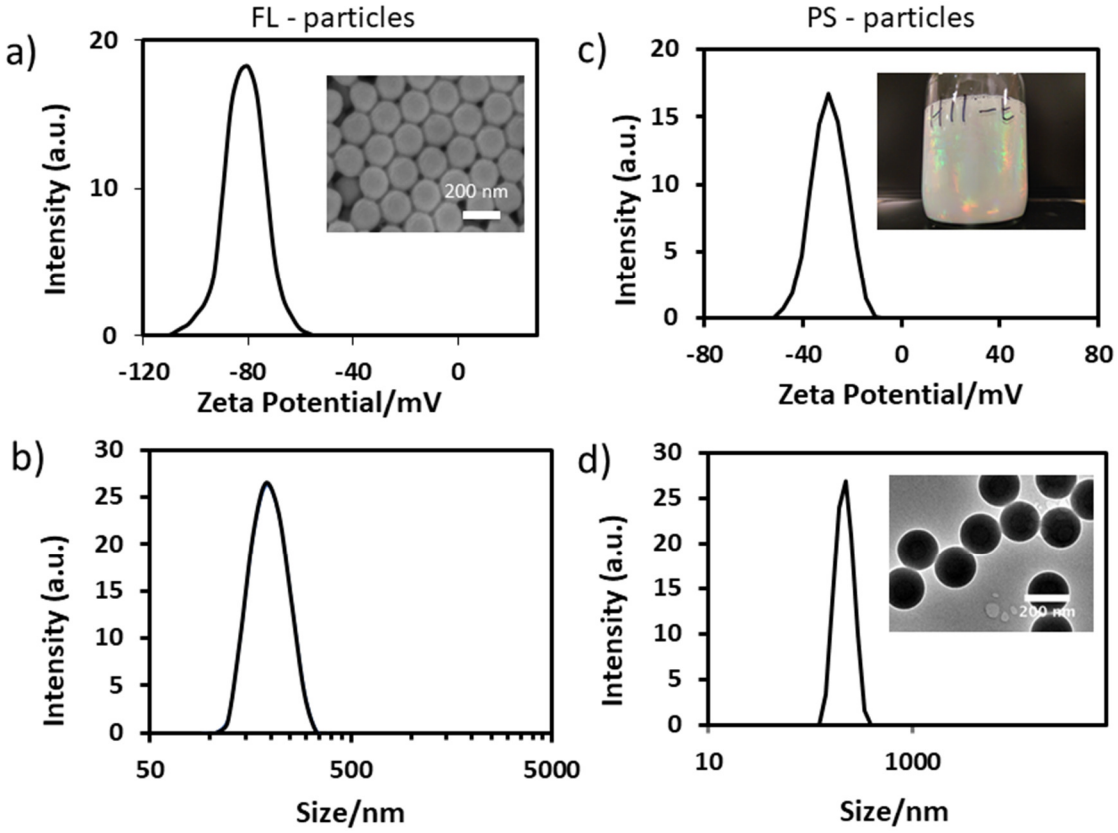

Figure 6.1. FL and PS particle size and zeta-potential. a) Zeta-potential measurement of the synthesised FL particles suspended in 10 mM PB. The inset shows an SEM image of the dried particles. b) Size distribution of the FL particles measured using DLS. c) Zeta-potential measurement of PS particles suspended in 10 mM PB. The inset shows a photograph of these PS particles after synthesis and washing. The particle content is roughly 2%, but the strongly scattering dispersion still shows iridescent colours. d) Size distribution of the PS particles measured using DLS. The inset shows a TEM micrograph taken of the dried PS particles. Taken from ref. [172].

The form factor, $F(q)$, obtained for dilute suspensions with a colloidal volume fraction of $\Phi \approx 0.1\%$ shed some light on this size difference. Analysing the scattered intensity obtained in SAXS measurements revealed a bimodal distribution with 70% of the signal accounting for FL particles with a diameter of 183 nm with the remaining particles having a rather narrow size distribution around 134 nm. Details are given in the section on SAXS.

Note that dried films of FL particles appeared completely white at all angles except in a very narrow angular range where a strong purple Bragg reflection was seen.

Figure 6.1 also presents zeta-potential measurements done in 10 mM PB, revealing that the FL particles were strongly charged with a potential of (-82 ± 4) mV. In addition, similarly sized PS particles were characterised: the zeta-potential was (-30 ± 4) mV and the hydrodynamic diameter was 220 nm with a polydispersity index of 1.4%. TEM images gave a dry particle size of (190 ± 5) nm suggesting that the PS particles had 'shrunk' less than the FL ones when dried. Hence in aqueous solution the two particle sizes were similar but still more than 10% different. Dry films of these PS-particles showed an even stronger white appearance with a sharp Bragg reflection in the blue, resulting from the ordering of the colloids into hexagonally close-packed layers at the free film-air interface. The white background was due to the strong scattering from the PS particles, which had a refractive index of 1.56, and disorder in form of grain boundaries and lattice defects generated during the drying process.

6.2 Reflectivity and Transmissivity

Both dilute, aqueous suspensions of FL and PS particles appeared completely white. Nevertheless, both dispersions already showed some structural colour in dilute solutions with only about 2% colloidal volume fractions due to their strong charge and their ordering close to the container walls (Figure 6.1 c inset).

However, concentrating the FL particles by centrifugation resulted in significantly more transparent and overall coloured samples (Figure 6.2), while both pure PS and PS+FL suspensions remained predominantly white and non-transparent. For better visualisation and for the SAXS measurements shown later, the concentrated samples were injected into flat 30×20×0.2 mm glass capillaries, which were then sealed with epoxy glue. In Figure 6.3 a the images of FL samples displayed a strong blue reflection at an estimated ~40% volume fraction, green at volume fractions of around 26-33% and red at 20-23% v/v. UV-Vis spectrometry transmission measurements were then done over a path length of 1 cm and showed that the transmission decreased with decreasing concentration in the range of 40-20% v/v (Figure 6.3 b). Below around 15% v/v, the FL suspensions turned white and non-transparent again, suggesting a transition from an ordered to a more liquid, disordered state.

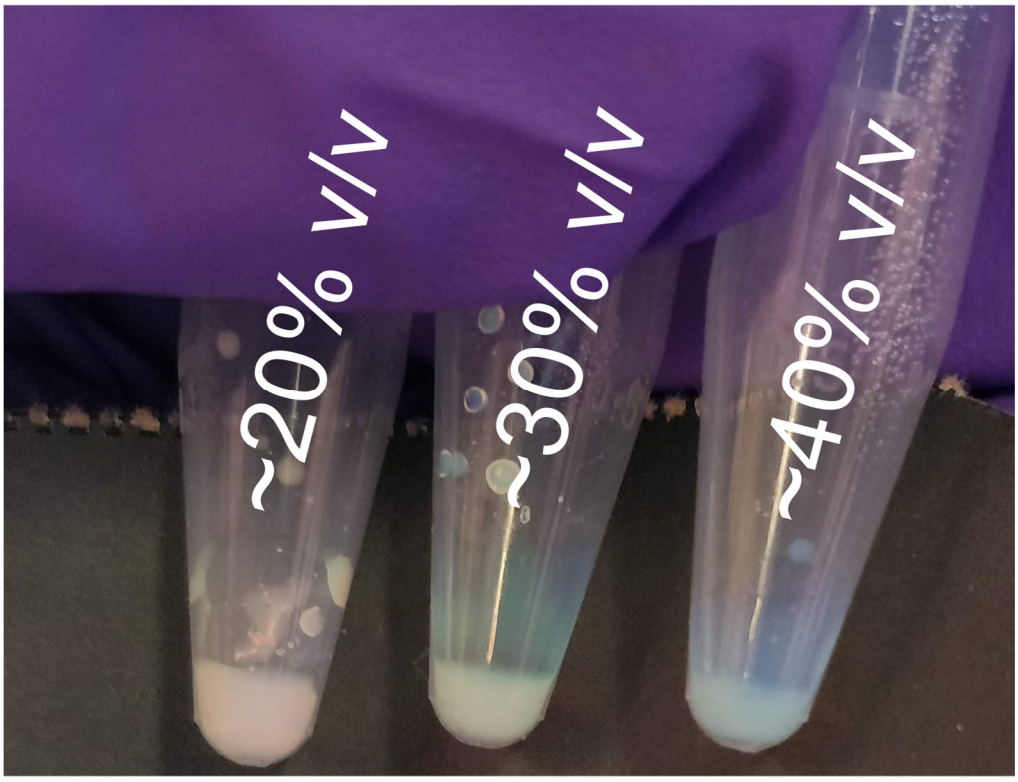

Figure 6.2. FL200 particles at three different concentrations under daylight.

For comparison, suspensions of PS particles of very similar size and zeta-potential were also investigated. As expected, the PS suspensions with a $\Delta n \approx 0.23$, the difference in refractive indices between the colloidal matter and the aqueous phase, remained predominantly white at concentrations between 2% and 40% v/v with a strongly angle-dependent colour due to Bragg scattering that appeared in the range of 20% to 40% v/v. Further testing included looking at PS+FL particle mixtures in the volume fraction range of 20-40% v/v, with the idea being that a lower Δn should convey more transparency. Although these mixtures were white at most angles and opaque overall, they did show some strong Bragg reflections within a very narrow angular range, which is discussed in the SAXS section.

Compared to previous reports on colloidal crystals, which typically show a white background with a sharp Bragg reflection, these FL suspensions displayed three interesting properties. The first was enhanced transparency in samples with volume fractions ranging between 15% and 40%. The second was the relatively angle-independent colour seen by the naked eye. The last was that some samples showed an additional strong Bragg reflection within a very narrow angular range typical for most photonic crystals made of spherical particles, but those that did not show such Bragg reflection still appeared coloured and partially transparent. Interestingly, the angle-

independent colour seen in reflection by the naked eye showed a small variation in the position of the reflection peaks, depending on the location in the sample (Figure 6.3 c and Table 1). Such a weak dependence suggests the existence of multiple crystalline domains having similar but slightly different lattice constants that most likely had originated from both fractionation due to small variations of surface charge from colloid to colloid and the bimodal size distribution of these FL particles. Further, having multiple crystal domains of similar character but different orientation may be the reason why we see relatively angle-dependent colour, combined with a sharp Bragg peak appearing only at certain angle.

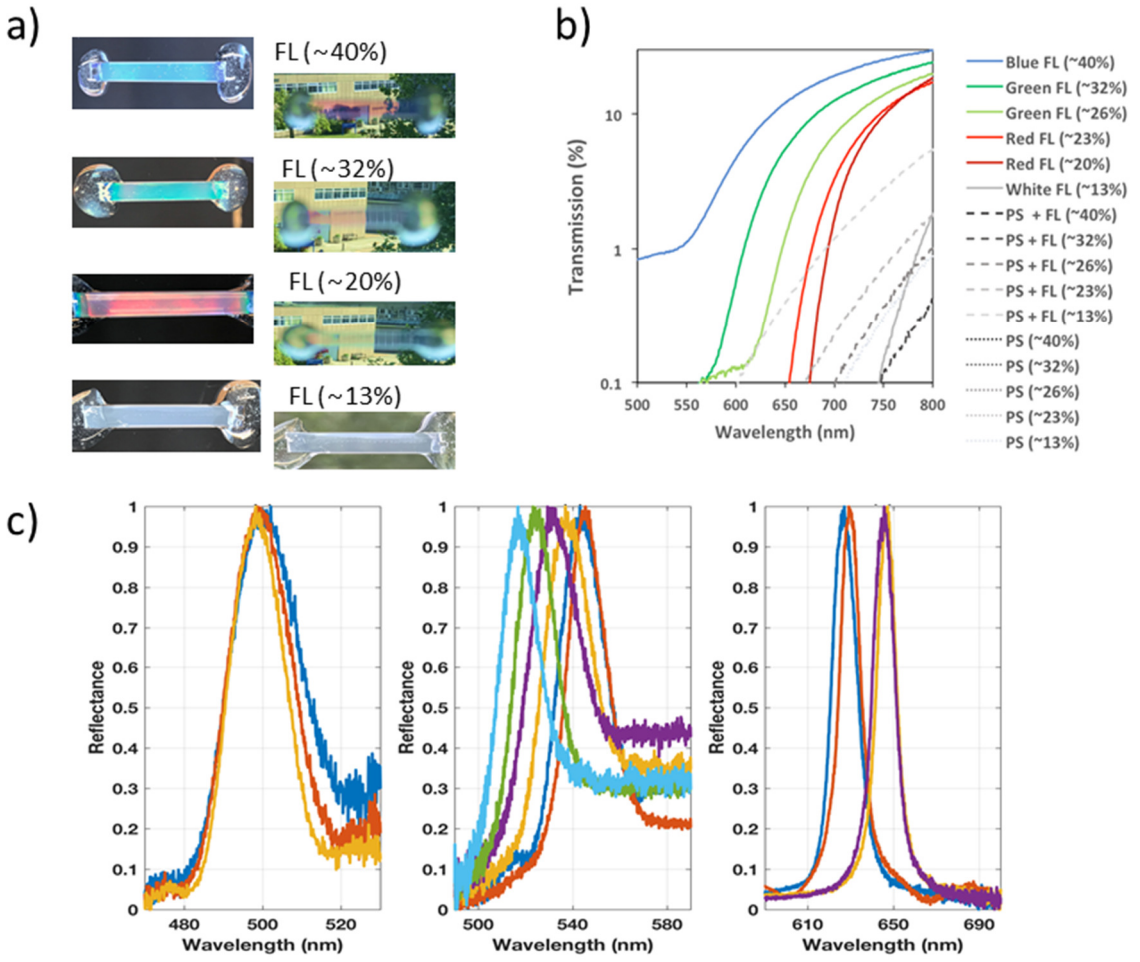

Figure 6.3. Reflectivity and transmissivity of FL samples. a) Photographs of flat capillaries containing aqueous suspensions of about 193 nm large FL particles of different concentrations, taken in reflection (left) and transmission (right). b) Transmission spectra measured using a UV-Vis spectrophotometer over a path length of 1 cm containing different volume fractions of FL, FL+PS and only PS particles. c) Normalised reflectivity measured at different positions in the (left) blue, (middle) green and (right) red sample of the FL suspensions shown in a). Figure taken from ref. [172].

	Peak position/nm	Line width/nm
Blue	498.0	16.6
	499.4	19.5
	500.2	22.4
Green	543.1	25.2
	545.3	21.2
	536.3	27.1
	531.5	30.4
	524.8	22.8
	516.8	22.6
Red	627.0	13.6
	629.1	11.5
	647.2	10.5
	645.6	12.0

Table 1. Measured reflection peaks and line widths.

6.3 Small-Angle X-ray Scattering

Following the reflectivity measurements indicating that the charge-stabilised FL colloids had formed ordered structures, SAXS measurements were performed using the focused beam of the ID2 beamline at the ESRF. Figure 6.4 shows two-dimensional SAXS patterns and the corresponding structure factors, $S(q)$, that were obtained by azimuthally integrating the scattering intensities, $I(q)$, and dividing these by the separately measured form factor, $F(q)$. The figure shows a sample with a volume fraction of about 40% containing only FL particles and a 1:1 mixture of similarly sized PS and FL particles. As expected, the pure FL suspension displayed very clear Bragg peaks, arising from the (111), (220), (113) and (133) scattering planes of a face-centred cubic (FCC) lattice corresponding to scattering vectors q_0 = 0.0403 nm^{-1}, q_1 = 0.0657 nm^{-1}, q_2 = 0.0765 nm^{-1} and q_3 = 0.1013 nm^{-1}. The strong hexagonal arrangement of the peaks stems from the dense (111) planes aligning parallel to the confining flat capillary walls. One could be tempted to think that this strong scattering came from a single crystal. Inspecting both the 2D spectrum and the radial integration more closely, three observations can be made. First, the Bragg peaks were slightly spread radially, which indicates a slight spread of the rotational orientation of the (111) planes. Hence it would be surprising to have a single crystal in the sample

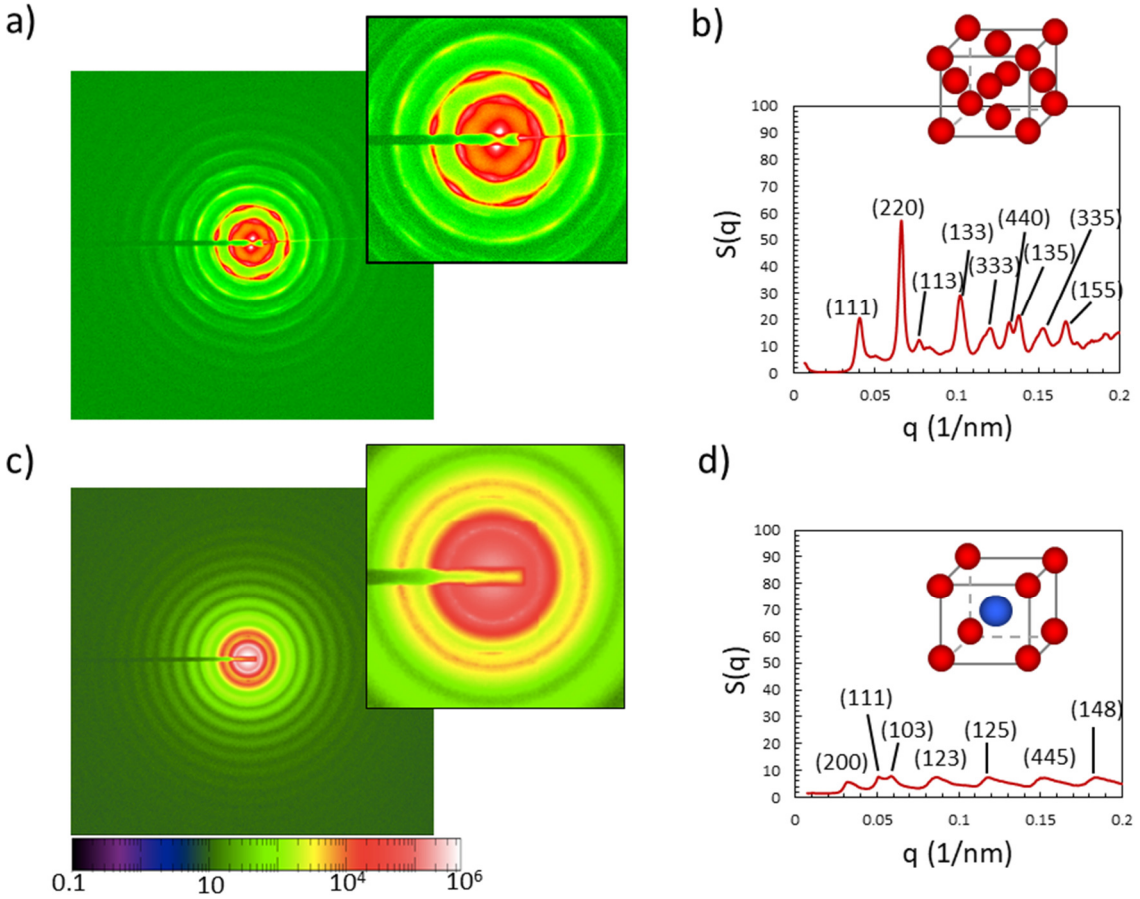

Figure 6.4. SAXS spectra of 30% v/v FL and FL+PS samples. a) SAXS spectrum taken of a 40% FL particle suspension. b) Azimuthally integrated structure factor of this sample, after dividing out the form factor, measured in a 0.1% suspension. The peaks are assigned to the corresponding Miller indices (hkl). c) Corresponding SAXS and d) integrated spectrum of the 1:1 mixture made of FL and PS particles. Figure taken from ref. [172].

considering the sample thickness was 200 μm and the beam size 150×150 μm. Moreover, similar scattering peaks with identical position were obtained in several spots measured in the sample. Second, there were faint hexagonal scattering patterns like rotated shadows of the strong peaks but at slightly higher *q* values. This may be due to the formation of a smaller crystal but with slightly larger lattice spacing and orientation. The difference in lattice spacing can be understood in terms of the bimodal size distribution (Figure 6.5) across all FL colloids, leading to local fractionation.

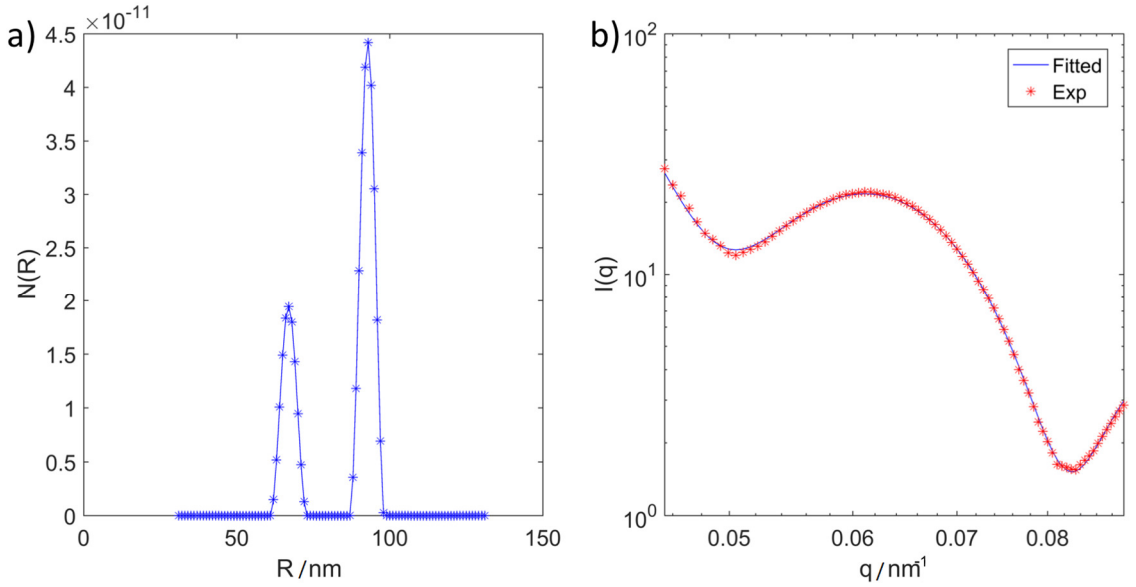

Figure 6.5. Bimodal FL particle size distribution. a) The distribution of particle number as a function of particle radius and b) the fit of bimodal particle distribution to the experimentally measured I(q) of 0.1% FL particle sample in SAXS.

Furthermore, the sample volume fraction had initially been estimated to be roughly 30%, but from the main peaks at q_0 = 0.0403 nm^{-1}, the separation between the centres of two neighbouring colloids in the FCC lattice was computed to be 191 nm, corresponding to 50% v/v. This also meant two colloid surfaces were roughly 30 nm apart. Such a big variation between estimated and measured volume fraction might have been due to the fact that a dense colloidal suspension evaporates much more rapidly during the filling of the capillaries than dilute ones. While it is known that FCC crystals of hard spheres never form for size polydispersities larger than 6%, that will not influence the crystal formation in a Wigner crystal [173]. The difference in lattice spacing observed in this system is possibly due to the bimodal size distribution of the FL particle samples and because the colloids will have a charge distribution. As the charged FL colloids in these suspensions had the possibility to rearrange, local fractionation into local crystals of similarly sized particles with similar surface charge was observed. Lastly, the $S(q)$ spectra showed many more peaks at larger q values, which could not be assigned to the FCC structure but rather to a BCC symmetry, very similar to the situation observed by Sirota et al. [111] who found a coexistence between FCC and BCC crystals and a glassy texture at higher volume fractions and low ionic strength. Glassy textures are typical for metallic glasses made of a single component. This coexistence of different crystal structures and lattice variation within a crystal structure due to size or charge polydispersity in combination with a small refractive index variation explains why strong iridescence under certain angles was

observed, while the samples on the whole showed rather angle-independent structural colour and significant transparency.

Indeed, Sirota et al. performed systematic SAXS measurements of charged PS-particle suspensions, establishing a phase diagram by plotting the measured structure as function of the ionic strength in the sample [111]. At very low ionic strengths (deionised solution) they observed a first transition from a liquid, disordered phase to a BCC crystal, followed by a coexistence region between BCC and FCC structure as the colloid volume fraction was increased from <5% to 6-15% and 16-22%, respectively. At even higher volume fractions the dispersions became glassy, manifesting the glassy character in terms of retaining some of the characteristic FCC-crystal peaks that had started to broaden. When the ionic strength was increased to about 0.2 mM, the BCC phase disappeared completely and the transitions from the liquid phase to an FCC structure and subsequently to the glassy phase shifted to higher volume fractions. Increasing the salinity slightly can also be interpreted in terms of making the repulsive Coulomb interactions more hard-sphere like, as the Debye screening length becomes more short-ranged but steeper (see Figure 1.1). With a zeta-potential of around -80 mV, these FL particles showed very similar behaviour in low salinity aqueous suspensions, although at slightly shifted volume fractions. Much like in Sirota et al. [111], the loss of crystallinity coinciding with the loss of transparency and the appearance of diffuse scattering when the samples' volume fraction became smaller than ~13% was observed. Whenever the samples were concentrated even more, the angle-independent structural colour in reflection and some transparency was retained, and the iridescence disappeared, which is most likely due to the increasingly glassy structure. SAXS images of these very concentrated samples showed more liquid-like scattering with up to 20 diffraction rings. Here it should be noted that while Sirota et al. made similar SAXS observations, their samples were strongly scattering in the visible range.

The scattering intensities measured for the 30% FL+PS suspensions also showed many scattering orders but at first glance one could have the impression that the sample was predominantly liquid, although on macroscopic inspection, iridescence under certain angles in reflection was observed, which could only have arisen from local order. Indeed, after zooming into the 2D scattering image, we see small but clear Bragg peaks (Figure 6.4 c). After dividing out the form-factor (using only the $F(q)$ of the FL particles), Miller indices (*hkl*) in the resulting $S(q)$ were assigned to the peaks, again using the fact that

scattering vectors are related to the nearest-neighbour distance a via $q_i = (\frac{2\pi}{a\sqrt{2}})(h^2 + k^2 + l^2)^{1/2}$. Diffraction peaks in a single-species crystal with FCC symmetry occur only for combinations of all (*hkl*) being either even or odd, while for BCC lattices, the sum of the Miller indices must be even. However, in the case of this 1:1 mixture, peaks at all combinations of (*hkl*) were seen. This means these similarly sized but on average differently charged FL and PS particles seem to form a CsCl lattice with a simple cubic structure. It is apparent that the large width of the scattering peaks reflects the polydispersity and thus small crystallite formation in our system. Nevertheless, it is interesting that these seemingly different particles do not segregate from each other. This could be rationalised by the Hume-Rothery rules stating that if the difference in particle size is no more than 15%, then AB crystals will form. This is again in analogy to metallic crystals/glasses, which are, in this case, formed by two different species A and B.

6.4 Electromagnetic Simulations

Based on the SAXS measurement results, electromagnetic simulations were carried out to show that the changing the lattice parameter of the FCC sets the colour of the reflection.

We used a commercially available finite difference time domain simulator (Lumerical) in three dimensions to simulate the optical response of a similarly arranged colloidal crystal to an incoming plane wave of visible light. In these simulations, FL particles were modelled as dielectric spheres having a refractive index of 1.37 and the background index was set to 1.33 to mimic water. The lattice constant was changed between 350 and 500 nm. The structure was illuminated at normal angle by a broadband plane wave source. Bloch boundary conditions were applied at x and y boundaries of the simulation region while the z boundaries were set as a perfectly matched layer.

These simulations proved that, despite the low refractive index contrast between the medium and the colloids, this system could still reflect the incident light at a certain range of wavelengths which was determined by the lattice constant (Figure 6.6). They also showed that in principle the whole visible regime could be covered using these colloids which further proved the feasibility of using these materials in colour filters, reflectors, and optical coatings.

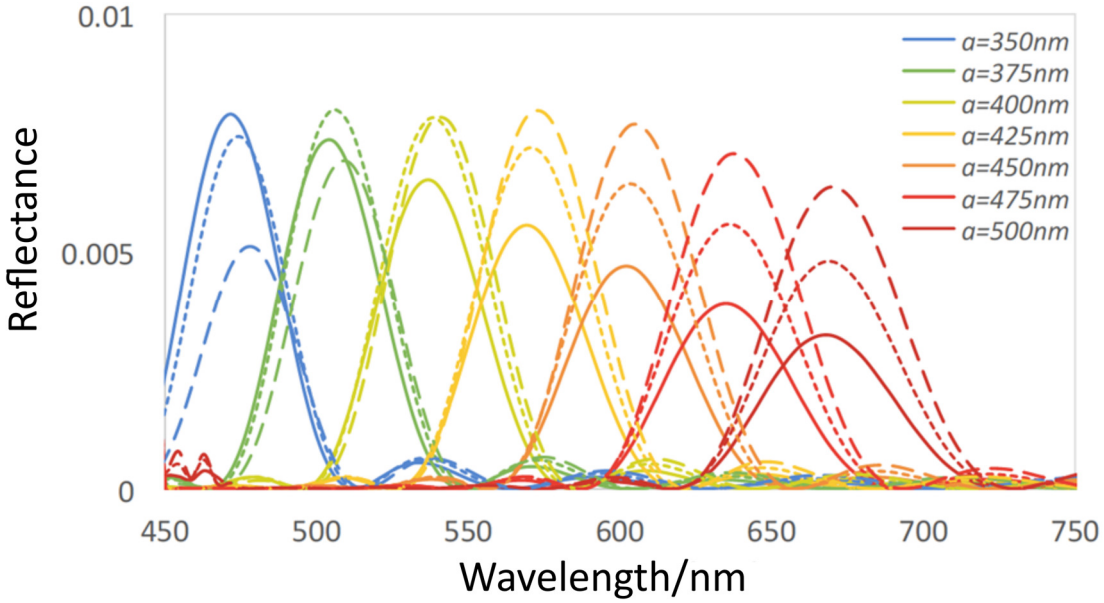

Figure 6.6. Simulated reflection spectra assuming an FCC crystal with different lattice constants a and particle diameters of 170 nm (continuous lines), 190 nm (short-dashed lines) and 210 nm (long-dashed lines). Taken from ref. [172].

It should be noted that iridescent colours were also obtained for FL particles that were 150 nm or 250 nm in diameter, however with a small shift in colour, with respect to a given volume fraction. However, the strength of the reflected colour seemed to be pronounced the most for the roughly 190 nm diameter ones.

6.5 Conclusions and Outlook

Photonic crystals made of fluorinated latex particles possessing a low refractive index were investigated in this chapter. The crystal structure of the system was studied using SAXS and determined that these colloids self-organised into predominantly FCC lattices. Their low refractive index helped to obtain a transparent colloidal photonic crystal which had strong reflectance at a certain range of wavelengths within the visible regime. Using electromagnetic simulations, the observations were confirmed and showed that the reflection colour had a strong dependence on the lattice parameter. Being transparent but also possessing a tuneable reflection band, these colloidal photonic crystals hold great promise for low cost optical coatings and filters. Finally, this work also showed that 1:1 mixtures of similarly sized FL and PS particles with different strong negative surface charge instead formed a simple cubic structure, reminiscent of an CsCl crystal. Such a CsCl structure is also found in binary (AB) metallic crystals, in which the two different species have different electronic contrast.

Further work has been planned to include ‘inverse opal’ structures, where the refractive index of the particles is smaller than that of the continuous phase.

7 Additional Projects

7.1 Gold Nanoparticles and Viruses

So far, this dissertation has focused on spherical colloidal particles. This section explores how colloidal interactions can be used to assemble anisotropic colloids together with spherical particles using DNA. Namely, gold nanoparticles and fd-virions were used. The resulting colloidal gels exhibited different morphologies than those accessible using only spherical colloids.

The work described in this section was adapted from the manuscript in reference [90]. The present author contributed to fd-virion production, DNA-coating, virion-nanoparticle gel formation, imaging and image analysis.

7.1.1 fd-Virus DNA-functionalisation

The filamentous bacteriophage fd-virus belongs to a relatively small category of filamentous viruses together with the Tobacco Mosaic Virus (TMV) and the M13 bacteriophage. All three of these have garnered the attention of soft matter researchers due to their high aspect ratios and great monodispersity, owing to their biological origin. While the TMV has a persistence length of 10 times its length, the M13 and fd-virions behave like semiflexible rods as their persistence lengths are only 2.5 times the length of the virion [174]. In addition, the M13 and the fd-virions only differ by a single amino acid in the major protein coating [175].

This work was built upon the research of Unwin et al. [176] who laid the groundwork for producing and functionalising the fd-virions with DNA. The fd-virions themselves have a length of about 880 nm and a diameter of ~8 nm, hence their effective aspect ratio could be in excess of 100 when the negative charges of the coat proteins were sufficiently screened [176]. Moreover, the approximately 2700 gp8 coat proteins have exposed amine groups, which were used to graft thiolated DNA to the virus. The functionalisation made use of a two-step process, similar to the procedure used to functionalise FL colloids in Chapter 3.1.2. First, sulfo-SMCC was reacted with the amine groups of the gp8 protein (Figure 7.1 a top). The functionalised virions were then purified using spin columns to remove the excess crosslinker. Thiolated DNA that had been activated using DTT was

then reacted to the maleimides on the virions (Figure 7.1 a middle and bottom). Finally, the DNA-functionalised virions were dialysed to yield the final product. The grafting density of DNA was measured to be ~160 strands per virion using UV-Vis spectroscopy by assuming the DNA and fd absorption profiles were additive when DNA was attached to the fd capsid. The DNA sequence used was thiol - 5'- TTT TTT TTT TTT TTT CCA ATC CAA T - 3' (**S**).

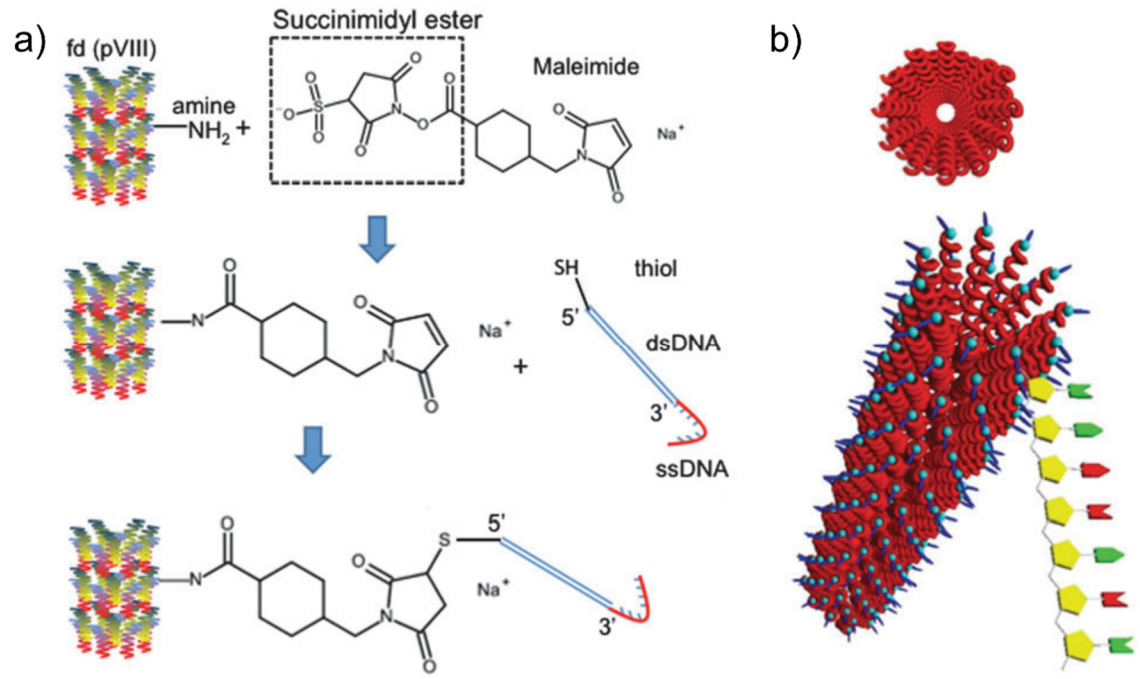

Figure 7.1. A schematic of fd-virion functionalisation with DNA. a) The coating process. B) 3D representation of the top view of a wild type fd-virion, showing its hollow inner part, and a side view showing an individual ssDNA with arbitrary sequence linked to major coat protein gp8. Image taken from ref. [176].

The gold nanoparticles (gold NPs) were purchased from Nanocomposix and functionalised with DNA by Z. Ruff. The full protocol is available in ref. [90]. The exact sequence was complementary to **S**: thiol - 5'- TTT TTT TTT TTT TTT ATT GGA TTG G - 3' (**S'**).

7.1.2 Structural Studies of Composite fd-NP Gels: Fast vs Slow Quench

NP mixtures with three different number ratios (R_{GV}) of gold NPs to virion particles were made in 10 mM TE buffer containing 50 mM NaCl. The volume fraction of gold colloids was 0.1% in all samples. Systems with R_{GV} = 2.5, 5 and 10 were studied, along with a control sample containing only gold NPs, in which half of the spherical particles were coated with **S** and the other with **S'**. Figure 7.2 depicts the system. The length of the virion

is an order of magnitude larger than the diameter of the gold NPs, allowing for multiple gold spheres to bind to a single virion. Therefore, the virions can be thought of the backbone of the gels held together by gold NPs.

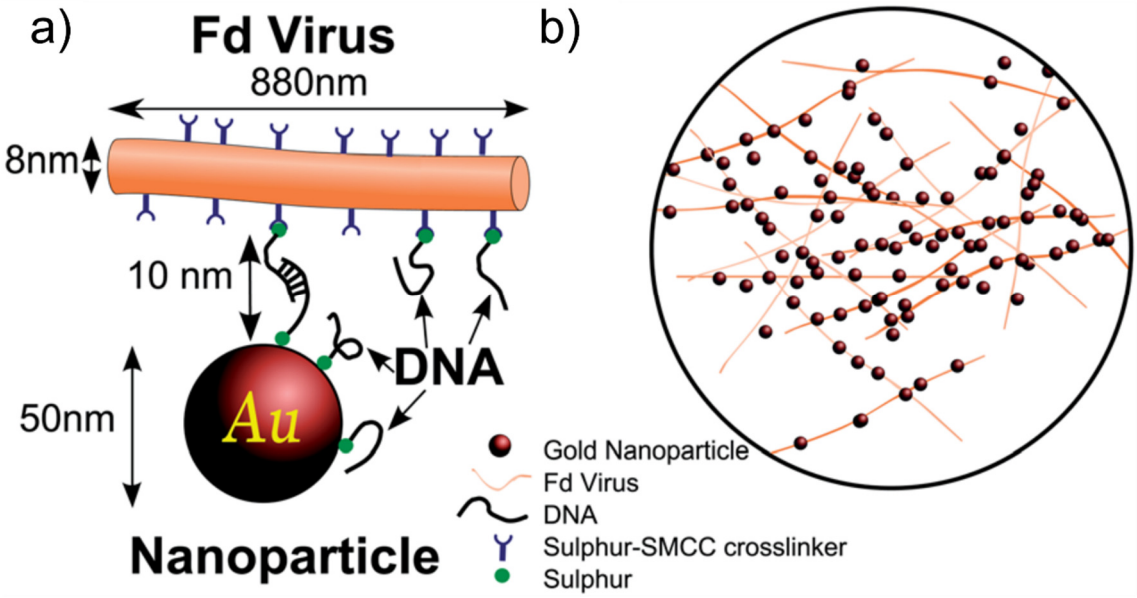

Figure 7.2. Sketch of the fd-viron and gold NP system. a) Gold nanoparticles attached reversibly to fd-virions via pairs of complementary DNA strands. b) Cartoon depicting the expected local network structure of viruses and nanoparticles in a kinetically arrested state. Image taken from ref. [90].

The same optical microscopy setup was used as in Chapter 4, with a Peltier device equipped with a PID controller for temperature control. Although the fd virions are almost one micrometre long they were too thin to be visible in optical microscopy and so were individual gold NPs. Nanoparticle aggregates, however, were visible and fluorescent microscopy with the gold NPs acting as a negative contrast agent against the fluorescent background of the solvent (fluorescein salt) was done. For the NP-virion system, images were obtained after mixing the sample but before heating it inside the microscope, after heating it to above the melting temperature of the DNA inside the microscope, and after cooling it to room temperature again (Figure 7.3). No sedimentation was seen in the sample of NPs and virions in the gaseous phase (Figure 7.3 c). Very different structures were seen before and after homogenisation at a high temperature – the difference in morphologies was a result of different cooling rates. The structures will be referred to as 'open' and 'homogenised'. When all three samples with different R_{GV} values were quenched from 60 °C (the samples had been prepared at that temperature outside the microscope) to RT in the microscope, open structures were observed. As RT was well

below the melt temperature of the DNA of this system (~42 °C), the samples went through macroscopic phase separation. They were then heated to 50 °C for a sufficient time, ~30 minutes, to have them return to the gaseous phase. After that they could be cooled down to RT in a controlled fashion inside the microscope, resulting in more fine-stranded structures, such as those seen in Figure 7.3 b. Just like in Chapter 4, these melting-cooling cycles could be repeated many times with the fine-stranded gel being reproduced each time.

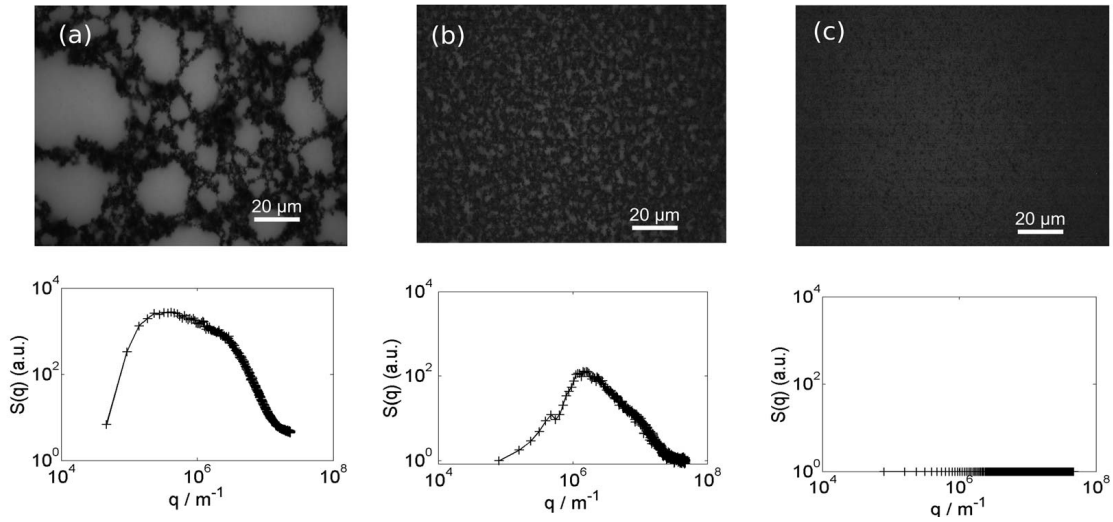

Figure 7.3. Epifluorescence microscopy images and the corresponding structure of the gold NP – fd-virion composite system. a) At RT: before homogenisation at a high temperature. b) At RT: after homogenisation. b) At 50 °C. Figure taken from ref. [90].

To understand these results, one must consider the difference in cooling rates: for the open structures, the cooling was approximately exponential, while the homogeneous structures were a result of a controlled linear cooling (Figure 7.4 a). During rapid cooling, the DNA base-pair mismatch was high, leading to a lower apparent melting temperature and a less stable structure. In this rapid quench, many small clusters formed which could still diffuse and join together, forming the structure seen in Figure 7.3 a. Meanwhile the slow cooling produced larger clusters which diffused slower and got kinetically arrested. This was even more evident after looking at structure factor analysis (see Chapter 2.5.2 for details) in the gaseous phase (Figure 7.3 c) $S(q)$ was flat, meanwhile in Figure 7.3 a and b a peak appeared, which is characteristic of arrested spinodal decomposition [105, 177]. However, for the fast quench the peak was much broader when compared to the slow cooling, evidence of spinodal decomposition followed by aggregation of clusters.

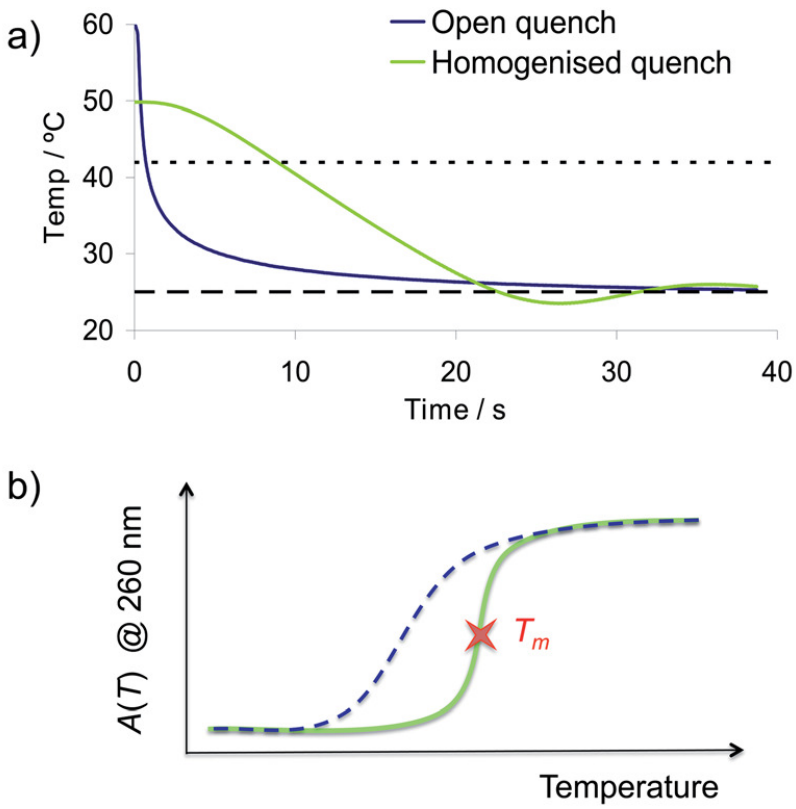

Figure 7.4. Curves of the different quenches performed on the system. a) Temperature vs time plot of the samples in open and homogenised quenches. b) Schematic melt curves of the samples, where the solid line indicates equilibrium cooling and heating while the dashed line shows a hypothetical out-of-equilibrium cooling curve. Figure taken from ref. [90].

7.1.3 Structural Evolution as a Function of Quench Depth

In order to study the kinetics of gel formation, the samples were quenched from the gas phase to four different temperatures below the melt temperature, with epifluorescence microscopy images taken every 20 seconds. Figure 7.5 a shows the time development of $S(q_{\max}, t)$, the peak of the system's structure factor, for the sample with R_{GV} = 5. The shape of $S(q)$ stayed the same while the magnitude increased proportionally at each wavevector. The preferred wavevector $q_{\max}$ stayed constant, indicating spinodal phase separation being the gel formation mechanism; the gel did not show subsequent coarsening after the initial formation [105, 177]. This happened due to the high collective binding energy of the DNA interaction (~ tens of $k_B T$) and which was activated over a narrow temperature transition of a few degrees. The density fluctuations with the characteristic wavevector $q_{\max}$ grew until gelation arrested further coarsening of the aggregates, marked by the plateau in Figure 7.5 b. In addition, the transition from a

completely fluid sample with no structural peak at 44 °C to the onset of gelation (42 °C) was observed: dropping just to this critical point the peak in the structure factor already showed evidence of demixing, and indeed cluster formation was seen in the sample, even though as a whole it still seemed to be fluid-like.

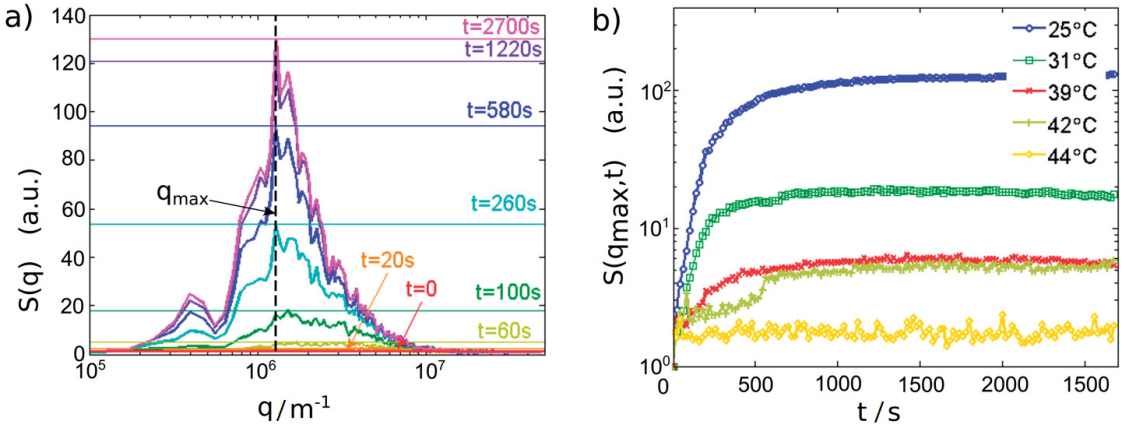

Figure 7.5. Time evolution of the structure factor S(q) of a gold NP–virion sample with R_{GV} = 5.S(q) evolution when the sample was quenched to 25 °C. The dashed line shows the position of S(q). b) The height of the maximum of S(q) over time for various quench depths for the same system. Figure taken from ref. [90].

The rate of gel formation was similar for all quench depths, with $S(q_{\max})$ reaching higher values for lower quench temperatures. Looking at the slopes of the increase in $S(q_{\max}, t)$ more closely, the phase separation process seemed to become faster as the sample was cooled deeper into the two-phase region, but the overall structure of the fine-stranded gel did not change much. As explained above, the full attractive potential is already reached a few degrees below the melting temperature, owing to the finite and well-defined attractive interactions provided by the DNA. Hence it was only the entropic term that provided lowering of the system's Gibbs free energy upon further cooling.

Average length-scales (λ_{pores} and $\lambda_{\text{aggregates}}$) were then obtained from chord analysis (see Chapter 2.5.1 and Chapter 4). While $S(q)$ was the result of averaging over the entire sample, chord analysis separated the two phases, providing complementary information. For the samples quenched to 25 °C and 39 °C, λ_pores and λ_aggregates were found to be similar at both temperatures and times for both samples, again suggesting that the DNA hybridisation energy rather than the entropic energy was responsible for the most prevalent length-scales in the gel. However, unlike for the gels of Chapter 4 and the control sample gels comprised of only gold NPs, two length-scales were seen in the homogenised samples of the gold NP-virion system. Both are listed in Table 2. The short

length-scales were found to be on the order of one third of the contour length of one fd-virion. This suggests that the stiffness of the rods combined with the tendency for the gold NPs to bind as many rods as possible influence the overall gel structure of the system.

R_{GV}	Time/s	$\lambda_{aggregates}/\mu m$		$\lambda_{pores}/\mu m$
		short	long	
2	400	0.37	4.03	4.09
5	400	0.42	3.20	3.75
10	400	0.36	3.76	2.68
Control	400	-	1.95	3.19
2	1200	0.41	4.41	4.74
5	1200	0.39	4.09	3.02
10	1200	0.27	5.25	2.53
Control	1200	-	5.18	3.89

Table 2. Characteristic length-scales extracted from epifluorescence microscopy images of samples with different R_{GV} and control samples, all quenched from 50 °C to RT.

The shorter length-scale might correspond to the diameter of the gel branches linked along the long axis of the virions by gold NPs. Viruses bound perpendicular to each other would support a length-scale at least as long as the virus. Since no short length-scale was seen in samples of spherical colloids, this implies it indeed was a direct result of the virion-NP interaction. SAXS or SEM imaging might aid in resolving these length-scales more accurately.

The long aggregate length-scale was similar across all R_{GV} values, while the pore length-scale was decreasing with increasing R_{GV}. As the number of virions was decreased, the number of gold NPs was kept constant, increasing the number of points of contact per virion (the NPs), leading to a decrease in the overall porosity.

7.1.4 Conclusions

This work introduced a new binary system of long filamentous virions and gold nanoparticles, in which both were functionalised with complementary single-stranded DNA, providing temperature-reversible aggregation. Virion-NP binding was allowed, while virion-virion and NP-NP bindings were forbidden. The aggregation of this mixture of different ratios of NPs to virions was investigated as a function of fast and slow cooling rates using epifluorescence microscopy. Fast quenches resulted in ‘open’ structures, while

the slower cooling produced more ‘homogeneous’ colloidal gels. Overall, the structure formation in these NP–virion systems was somewhat different from that in systems of spherical particles. While spherical particle systems display one characteristic length-scale of the aggregates, this rod-sphere system showed two, indicating that the stiffness of the rods combined with the tendency of the gold NPs to bind as many rods as possible influenced the overall gel structure of the system. Finally, the aggregation depended on the concentration ratio of NPs to virions, with the samples containing a lower concentration of virions relative to the NPs being less porous.

7.2 Magnetic Field Assisted Self-Assembly of Colloidal Superstructures

When self-assembly of colloids through the usual thermodynamic pathways for relaxation into equilibrium structures is slow or hindered by kinetic barriers, external forces through gravity, shear stress, electric and/or magnetic fields can be employed. In this section an approach for directing the assembly of a multi-component system of DNACCs via an externally applied magnetic field is explored. Long coaxial skeletons of smaller colloids around larger superparamagnetic cores are demonstrated in a two-component system. Proof of concept is demonstrated to further stabilise these structures by adding a suitably functionalised third component.

The work described in this section was done in collaboration with D. Joshi.

7.2.1 Experimental Setup

Commercially available streptavidin-coated polystyrene and poly(methyl methacrylate) (PMMA) colloids were functionalised with biotinylated DNA, as described by Joshi et al. [132]. Swelling-deswelling was not used because swelling PS colloids containing superparamagnetic iron oxide nanoparticles caused the NPs to diffuse out of the polymer matrix, thus destroying the colloids. This could be circumvented by covalently linking the NPs to the polymer matrix in an updated system. Table 3 lists the colloids used. M refers to the superparamagnetic colloids, while R and G stand for red and green fluorescence.

Two sets of one-component gels of PS R1 colloids were prepared with $\mathbf{D_7D'_7}$ and $\mathbf{D_6D'_7}$ DNA to measure the melting temperatures, much like the one-component gels in Chapter 4. T_m was measured to be 48 °C for $\mathbf{D_7D'_7}$ colloids, whereas for the $\mathbf{D_6D'_7}$ ones it was found to be 34 °C. As before, **D** is complementary to **D’** while the number corresponds

to the bases in the sticky end; in this system it was necessary to introduce a double-stranded spacer (69 base-pairs) before the sticky end to make sure the end could explore a larger volume instead of coiling up due to the lower surface coating density.

Colloid type	Diameter/μm	DNA	Sticky end	Vendor
PS M1	2.8	**D_7**	CCC GGC C	ThermoFisher
PS M2	1.0	**D_7**	CCC GGC C	Microparticles
PS G	0.5	**D'_7**	GGC CGG G	Microparticles
PMMA G	0.2	**D'_7**	GGC CGG G	Microparticles
PS R	0.5	**D_6**	CCG GCC	Microparticles

Table 3. Types of colloids used in magnetic field assisted self-assembly experiments.

A pair of custom-made Helmholtz coils with a Peltier device were used to control the magnetic field and temperature of the samples in the optical microscope.

7.2.2 Two-component System

For a two-component system, the assembly strategies are outlined in Figure 7.6. Switching the magnetic field on at different stages determines the final assembled superstructure. A mixture of superparamagnetic (brown spheres in Figure 7.6) colloids and the second colloidal component of desired size (depicted green in Figure 7.6) coated with complementary DNA linkers are first heated to 60 °C to make sure the colloids are in the gaseous phase. Raspberry-like superstructures are formed when the system is cooled slowly in the absence of a magnetic field (Figure 7.6 Scheme I). These colloidal raspberries can then be aligned into chain-like structures by turning the field on. They diffuse and break apart if the field is switched off, as the green colloids do not bind amongst themselves. If the field is switched on at $T > T_m$ and the system is cooled slowly in the presence of said field, linear coaxial scaffolds with a superparamagnetic core are formed (Figure 7.6 Scheme II): first the superparamagnetic colloids are pushed together forming long chains as their magnetic dipoles align in the direction of applied magnetic field. Ideally the DNA coating should prevent them from permanently aggregating. After slow cooling in the presence of the magnetic field, the green colloids will coat the magnetic bead 'cables', attaching to them via DNA.

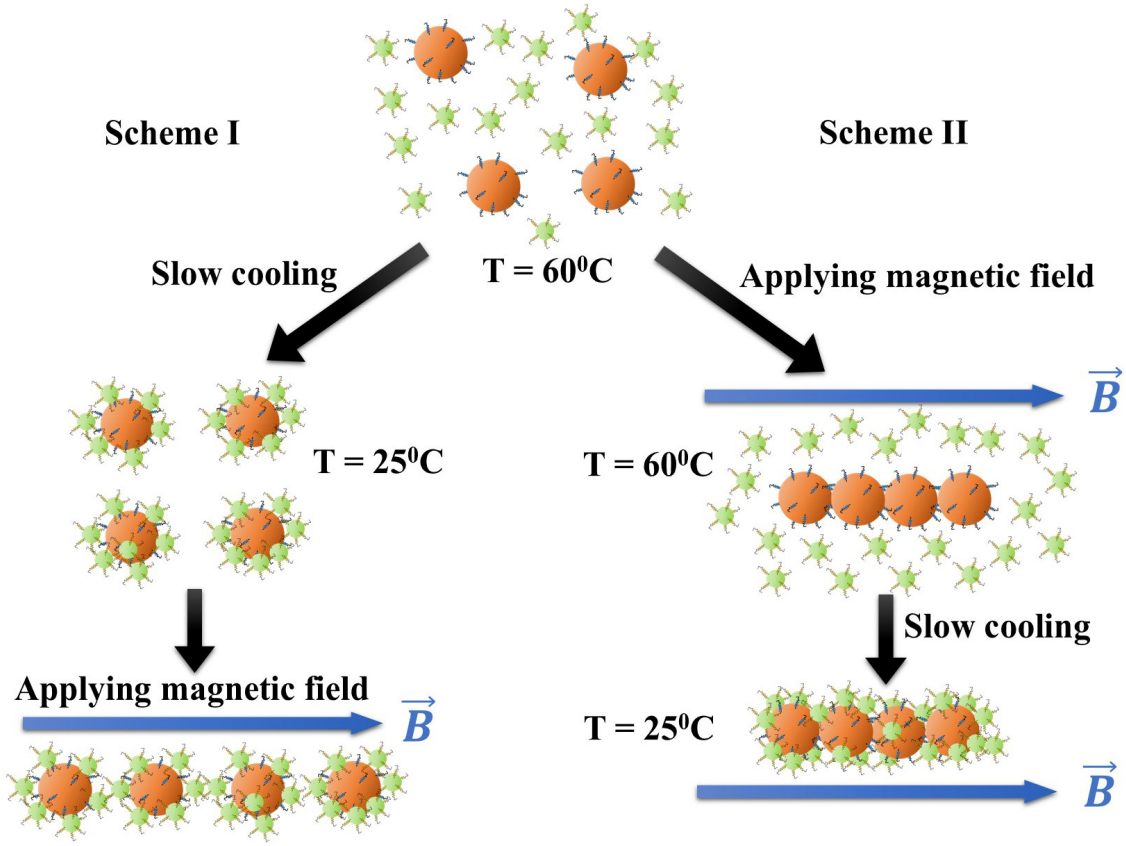

Figure 7.6. A cartoon describing the strategy for assembling 'raspberry' and coaxial scaffolds in a two-component system. The small green colloids represent non-magnetic particles, while the bigger brown ones are superparamagnetic. Figure created by D. Joshi and modified by the present author.

Working along Scheme I, PS M1 2.8 µm diameter colloids were mixed with PMMA G 0.2 µm diameter particles, heated up to 60 °C and slowly cooled down to room temperature (0.1°C/min). Care must be taken, as the small particles could bridge two or more of the large ones, hence this was done in a very dilute regime of the magnetic spheres (~0.01% v/v) with an excess of the small ones. After switching on the in-plane magnetic field at room temperature, these colloidal 'raspberries' aligned into straight chains in the direction of the magnetic field (Figure 7.7 a). These chains stayed assembled as long as the magnetic field was on and fell apart into individual raspberries due to thermal motion soon after switching off the field (Figure 7.7 b) . However, if a strong magnetic field (>20 mT) was applied, some of these structures would aggretate irreversibly (Figure 7.7 c), possibly due to a relatively low DNA coating density of the colloids. The superparamagnetic beads themselves were found to not have significant remanent magnetisation.

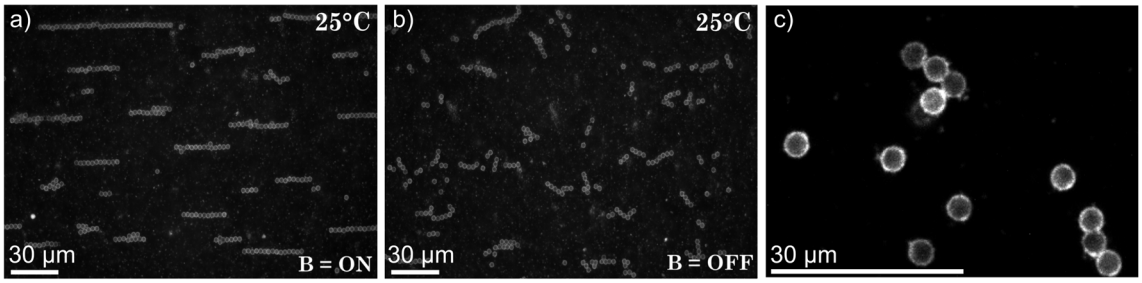

*Figure 7.7. Epifluorescence microscopy images of a two-component system composed of 2.8 μm PS superparamagnetic colloids coated with **D7** DNA and 0.5 μm green fluorescent PMMA G colloids coated with **D'7** DNA. a) Colloidal raspberries align into straight chains when an in-plane magnetic field is applied. b) These chains fall apart upon removal of the magnetic field. c) Zoomed-in epifluorescence microscopy picture showing the magnetic colloids coated with the green-fluorescent PMMA ones.*

The 0.5 μm diameter PS G beads were then used to coat the 2.8 μm diameter PS M1 particles through complementary DNA. When the system was cooled down from the gas phase, colloidal 'raspberries' were again formed. However, when the magnetic field was switched on above T_m and the sample was cooled in the presence of a magnetic field (so working along Scheme II of Figure 7.6), large coaxial chains with the superparamagnetic cores held together by small colloids through DNA hybridisation. Figure 7.8 shows epifluorescence images of long coaxial chains several hundred of micrometres in length, comprised of PS G colloids wrapped around the magnetic particles. These chains curled up or became floppy when the magnetic field was removed, but they did not break and fall apart even several hours after switching off the magnetic field. However, some non-specific binding was still seen in the system, showing further evidence for the need of higher coating densities. Note that the melting temperature for this system had increased to ~53 °C when compared to the control sample consisting of only PS G colloids with **$D_7D'_7$** DNA. This could have been due to the increased contact area between colloids (as the PS M1 beads were almost 3 μm in diameter and hence had smaller curvature), in addition to the non-specific aggregation.

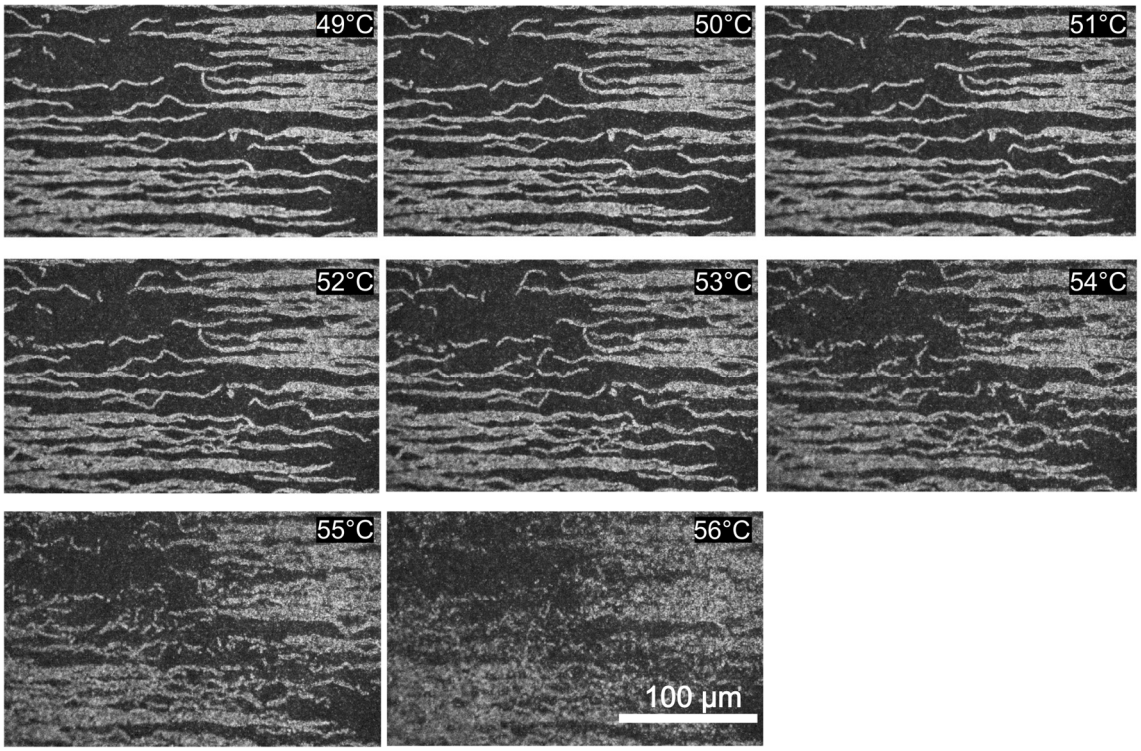

Figure 7.8. Epifluorescence microscopy images of a two-component system of floppy magnetic bead chains with the magnetic field off. The system was constructed according to Scheme I of Figure 7.6 using PS M and PS G colloids. The images show the progressive melting of the chains as the temperature was increased at the rate of 3 °C/min.

7.2.3 Three-component System

The self-assembly of long straight scaffolds is an important step towards multi-hierarchical and more complicated colloidal superstructures. As a proof of concept for functionalisation, we present 'furry chains' assembled in a three-component system. The third component – a colloidal species coated with $\mathbf{D_6}$ DNA – can connect to $\mathbf{D'_7}$ DNA bearing colloids, thus providing further rigidity to the long scaffolds.

Figure 7.9 shows a strategy of functionalising an existing linear scaffold further with a third component. At 60 °C all components of the system are in the gas phase. First, the superparamagnetic colloids (light brown Figure 7.9) are aligned into linear chains by applying a magnetic field as before and then the sequential DNA interactions are switched on by gradually reducing the temperature of the system. As the system is slowly cooled, the first attractive interaction switches on and the green PS colloids coat the magnetic beads forming linear coaxial scaffolds. Holding the system at 40 °C for a few hours allows for better coverage, as the green colloids have more time to explore the volume. Further

reducing the temperature of the system activates the second attractive interaction between the green and the red components, resulting in the red particles coating the green ones.

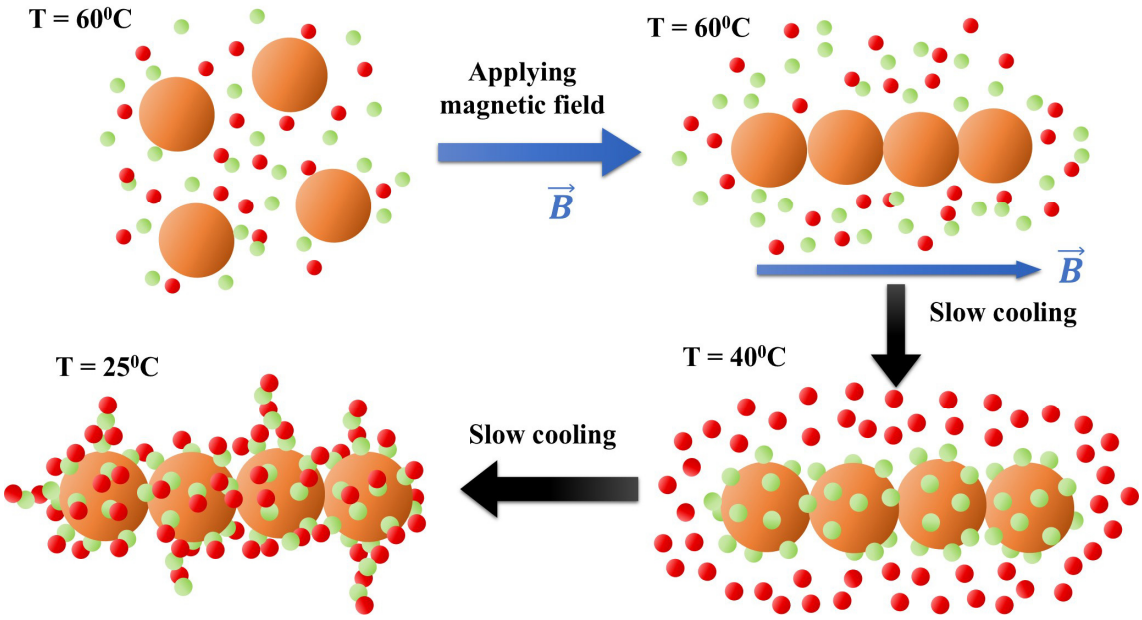

Figure 7.9. A cartoon demonstrating the strategy for functionalising linear scaffolds from a two-component system into 'furry chain'-like geometry by adding a suitably tailored third component. DNA linkers not shown for clarity of picture. Figure created by D. Joshi.

Starting with a two-component system having 1.0 μm diameter PS M2 superparamagnetic colloids and 0.5 μm diameter green fluorescent PS G colloids, PS R particles were added to the system. While cooling from a high-temperature homogeneous gaseous phase, the PS M2 and PS G binding switched on at a higher temperature (~53 °C). Cooling the system slowly and holding just below T_m for about an hour ensured that PS M2 particles were thoroughly covered by the PS G ones. Further cooling the system below the melt temperature of PS G-PS R colloids (**D'$_7$D$_6$**), the binding between PS G and PS R colloids was activated. Hence, PS R colloids were observed binding to PS G colloids attached to the PS M2 'backbone'. The addition of the third species imparted extra rigidity to the linear coaxial chains and we observed very stable and long, a few hundred of microns in length, chains without any floppiness (Figure 7.10). Since there were a number of PS G colloids free in the bulk of the solution, additional G-R aggregation in the bulk and also additional G-R-G-R chains branching out from our 'furry chains' were observed. This additional aggregation could be mitigated by performing these experiments in a temperature-controlled flow cell or microfluidic device where it would be possible to flow just enough PS G and PS R colloids to coat the chains without branching.

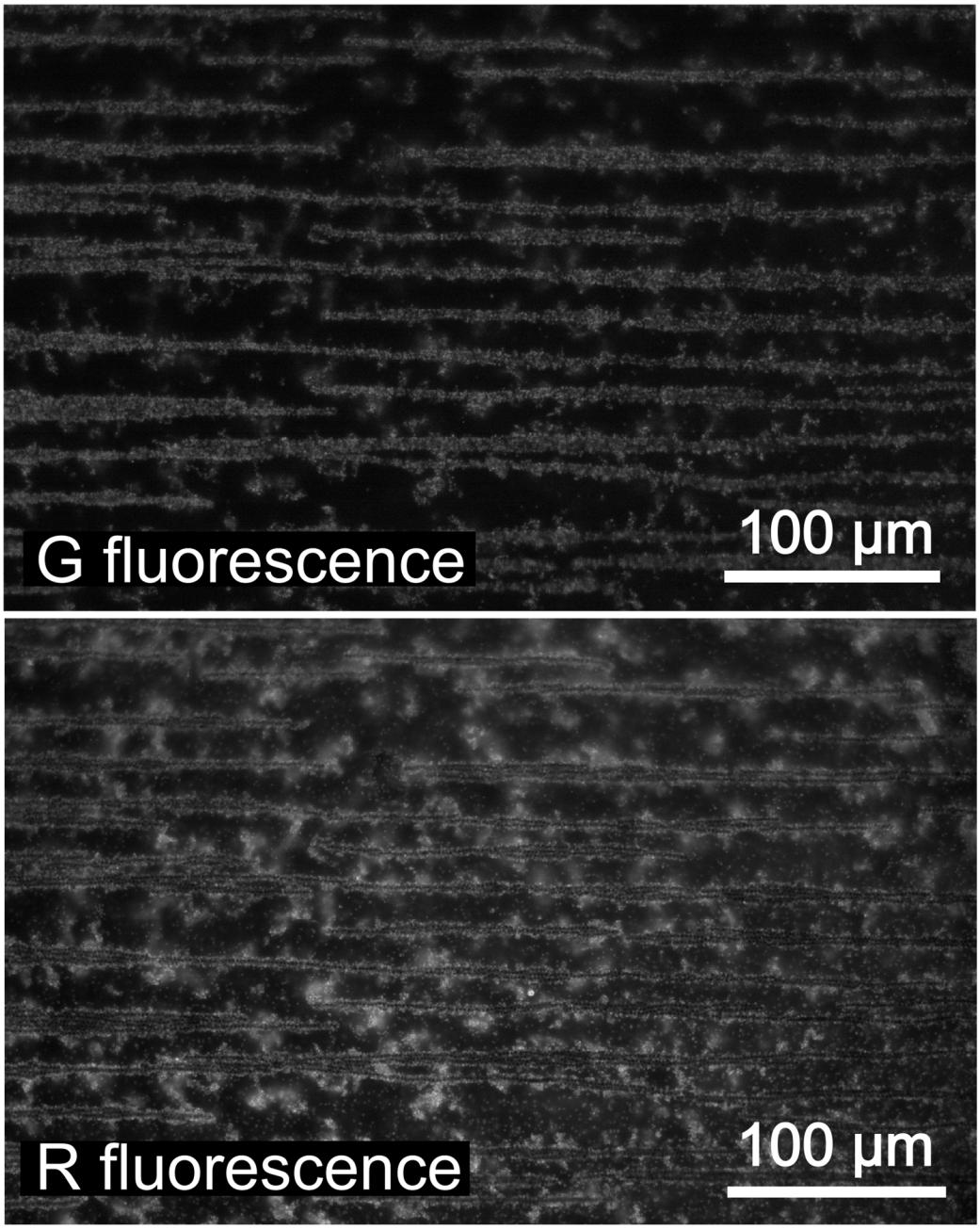

Figure 7.10. Epifluorescence microscopy images of a three-component system. It was composed of PS M2 magnetic colloids coated with PS G colloids, which in turn got coated with PS R colloids at a lower temperature, resulting in 'furry chains'.

7.2.4 Conclusions

This work has demonstrated thermally reversible assembly of colloidal components of various size ratios into raspberry-like and linear coaxial constructs via DNA and the use of an external magnetic field. Using superparamagnetic beads as one of the components ensured there was no remanent magnetisation. The addition of a third colloidal species that coated the coaxial scaffolds imparted more stability to the constructs.

8 Closing Remarks

This dissertation has outlined work contributing to the advancement of research on colloidal self-assembly, mainly focusing on DNA-coated colloidal particles. In-house polymeric particle synthesis and functionalisation with custom-tailored DNA ligands, explored in Chapter 3, allowed us to create functional monodisperse colloids. The particles were first coated with azide end-functionalised block copolymers through swelling-deswelling and had DNA grafted onto them via a click reaction, achieving coating densities as high as 12,500 ligands per one 200 nm diameter colloid.

Utilising these densely coated colloidal particles, the work in Chapter 4 demonstrated core-shell bigels, where the selective nature of DNA hybridisation was exploited to sequentially activate the attraction between the different components of the gel. A lot of industrial formulations have colloids in a jammed or gelled state, so this work was to provide information on the morphology of such structures. However, optical imaging deep inside colloidal gels is usually problematic due to light scattering. Fortunately, using fluorinated latex (FL) particles as one of the colloidal components enabled optical imaging deep inside these dense (10% v/v) gels, as FL particles had a very low refractive index (1.36-1.37) and were easily index-matched by adding sucrose to the aqueous solution. As the FL particles were relatively dense compared to the aqueous phase, to avoid the sedimentation of the gel, these colloids were condensed onto a polystyrene (PS) colloid 'scaffold' to make spatially homogeneous colloidal structures. In addition, the low refractive index was exploited further to track PS tracer beads inside a refractive index-matched FL gel, obtaining diffusivity data using Differential Dynamic Microscopy; these tracers were found to diffuse slower than they otherwise would, as they were indeed confined to 'cages' created by the surrounding gel.

In Chapter 5, the same coating strategy – using azide end-functionalised amphiphilic block copolymers – was employed to coat oil droplets (ODs) with DNA. Three emulsification strategies (ultrasonication, membrane emulsification and microfluidics) were employed to create stable oil-in-water emulsions. Due to using commercially available Synperonic surfactants, the functionalisation method proved to be very scalable, enabling batch production of these functional oil droplets. The self-organisation

properties were demonstrated by creating hierarchical droplet structures dubbed "raspberry droplets" and a thermally responsive emulsion gel of submicron-sized DNA-coated ODs. In addition, a simple controlled surface-release system was shown. Oil droplets are at the core of many industrial and pharmaceutical formulations and it is hoped that this work will provide a useful reference; compartmentalised formulations and controlled release are of interest in prolonging the shelf-life of emulsions, while careful design of the interactions between droplets might lead to emulsions and gels with novel and exotic properties. Our group is currently working on exploring the rheological properties of large DNA-coated oil droplets using the coating protocols described in this dissertation.

Chapter 6 jumped back to fluorinated latex particles; due to their size, high surface charge and low refractive index, they were found to self-organise into photonically active crystals at concentrations at and above 20% v/v, without any additional surface functionalisation. At these higher volume fractions, the colloidal solutions exhibited high transmissivity and strong reflectivity at a certain range of wavelengths within the visible regime. The reflection colour had a strong dependence on the lattice parameter, which in turn depended on the volume fraction of the samples. SAXS data showed these colloids would predominantly assemble into face-centred cubic lattices. Such fluorinated latex particle photonic crystals might have potential applications in wearable optoelectronic devices and optical coatings. Work is underway to investigate the system further by using particles of different size and creating 'inverse opal' structures, where the refractive index of the continuous phase is higher than that of the particles.

As an aside to the main research, Chapter 7 presented an investigation of a rod-sphere colloidal system, showing that the geometry of the building blocks and the quench speed could control the structure of colloidal gels. More complex colloidal structures could be formed through the application of an external magnetic field, as demonstrated in the second part of the final chapter.

The new findings outlined in this dissertation have the potential to contribute to the next generation of functional materials and it is my hope that the work of this rich field of physics that is soft matter will continue to innovate our daily lives.

9 REFERENCES

[1] J. N. Israelachvili, *Intermolecular and surface forces*. Academic Press, 2011.

[2] R. Jost, Jost, and Rolf, "Milk and Dairy Products," in *Ullmann's Encyclopedia of Industrial Chemistry*, Weinheim, Germany: Wiley-VCH Verlag GmbH & Co. KGaA, 2005.

[3] D. F. Evans and H. Wennerström, *The Colloidal Domain : Where Physics, Chemistry, Biology, and Technology Meet*. Wiley-VCH, 1999.

[4] Y. H. Roos and S. Drusch, *Phase Transitions in Foods*. 2015.

[5] A. Einstein, "On the Motion of Small Particles Suspended in Liquids at Rest Required by the Molecular-Kinetic Theory of Heat," *Ann. Phys.*, no. 17, pp. 549–560, 1905.

[6] T. G. Mason and D. A. Weitz, "Optical Measurements of frequency dependent linear viscoelastic moduli of complex fluids," *Phys. Rev. Lett.*, vol. 74, no. 7, p. 1250, 1995.

[7] A. J. Levine and T. C. Lubensky, "One- and two-particle microrheology," *Phys. Rev. Lett.*, vol. 85, no. 8, pp. 1774–1777, 2000.

[8] S. Keen, J. Leach, G. Gibson, and M. J. Padgett, "Comparison of a high-speed camera and a quadrant detector for measuring displacements in optical tweezers," *J. Opt. A Pure Appl. Opt.*, vol. 9, no. 8, pp. 2–5, 2007.

[9] J. Crocker and D. Grier, "Methods of Digital Video Microscopy for Colloidal Studies," *J. Colloid Interface Sci.*, vol. 179, no. 1, pp. 298–310, 1996.

[10] R. Cerbino and V. Trappe, "Differential dynamic microscopy: Probing wave vector dependent dynamics with a microscope," *Phys. Rev. Lett.*, vol. 100, no. 18, pp. 1–4, 2008.

[11] D. J. Pine, D. A. Weitz, P. M. Chaikin, and E. Herbolzheimer, "Diffusing wave

spectroscopy," *Phys. Rev. Lett.*, vol. 60, no. 12, pp. 1134–1137, 1988.

[12] J. N. Israelachvili, *Intermolecular and surface forces*. Academic Press, 2011.

[13] H. C. Hamaker, "The London-van der Waals attraction between spherical particles," *Physica*, vol. 4, no. 10, pp. 1058–1072, 1937.

[14] W. B. Russel, D. A. Saville, and W. R. Schowalter, *Colloidal Dispersions*. Cambridge: Cambridge University Press, 1989.

[15] P. Van Rysselberghe, "Remarks Concerning the Clausius-Mossotti Law," *J. Phys. Chem.*, vol. 36, no. 4, pp. 1152–1155, 1931.

[16] E. J. W. Verwey and J. T. G. Overbeek, "Theory of the stability of lyophobic colloids," *J. Colloid Sci.*, vol. 10, no. 2, pp. 224–225, 1955.

[17] D. Fairhurst and R. W. Lee, "The Zeta Potential & its Use in Pharmaceutical Applications - Part 1: Charged Interfaces in Polar & Non-Polar Media & the Concept of the Zeta Potential," *Drug Dev. Deliv.*, vol. 11, no. 6, p. 60, 2011.

[18] B. Derjaguin and L. Landau, "Theory of the stability of strongly charged lyophobic sols and of the adhesion of strongly charged particles in solutions of electrolytes," *Prog. Surf. Sci.*, vol. 43, no. 1–4, pp. 30–59, 1993.

[19] Y. Min, M. Akbulut, K. Kristiansen, Y. Golan, and J. Israelachvili, "The role of interparticle and external forces in nanoparticle assembly," *Nat. Mater.*, vol. 7, no. 7, pp. 527–538, 2008.

[20] P. G. de Gennes, "Polymers at an interface; a simplified view," *Adv. Colloid Interface Sci.*, vol. 27, no. 3–4, pp. 189–209, 1987.

[21] S. Asakura and F. Oosawa, "Interaction between particles suspended in solutions of macromolecules," *J. Polym. Sci.*, vol. 33, no. 126, pp. 183–192, 1958.

[22] D. J. Kraft *et al.*, "Surface roughness directed self-assembly of patchy particles into colloidal micelles," *Proc. Natl. Acad. Sci.*, vol. 109, no. 27, pp. 10787–10792, 2012.

[23] J. R. Wolters *et al.*, "Self-assembly of 'Mickey Mouse' shaped colloids into tube-like structures: experiments and simulations," *Soft Matter*, vol. 11, no. 6, pp. 1067–1077, 2015.

[24] S. Sacanna, W. T. M. Irvine, P. M. Chaikin, and D. J. Pine, "Lock and key colloids," *Nature*, vol. 464, no. 7288, pp. 575–578, 2010.

[25] S. Sacanna *et al.*, “Shaping colloids for self-assembly,” *Nat. Commun.*, vol. 4, pp. 2–7, 2013.

[26] A. C. Balazs, T. Emrick, and T. P. Russell, “Nanoparticle Polymer Composites : Meet Two Small Worlds,” *Science (80-)*, vol. 314, no. 5802, pp. 1107–1110, 2013.

[27] B. Meets, “Biotechnology Meets Materials Science,” *Mater. Sci.*, vol. 40, no. 22, pp. 4128–4158, 2001.

[28] Y. Lan, Y. Wu, A. Karas, and O. A. Scherman, “Photoresponsive hybrid raspberry-like colloids based on cucurbit[8]uril host-guest interactions,” *Angew. Chemie - Int. Ed.*, vol. 53, no. 8, pp. 2166–2169, 2014.

[29] Y. Lan, X. J. Loh, J. Geng, Z. Walsh, and O. A. Scherman, “A supramolecular route towards core–shell polymeric microspheres in water via cucurbit[8]uril complexation,” *Chem. Commun.*, vol. 48, no. 70, p. 8757, 2012.

[30] J. Watson and F. C. Crick, “Molecular Structure Of Nucleic Acids: A Structure for Deoxyribose Nucleic Acid,” no. 4356, p. 4356, 1953.

[31] N. Geerts, “DNA-driven Assembly of Micron-sized Colloids,” Universiteit van Amsterdam, 2009.

[32] H. H. Kazazian, *Mobile DNA: finding treasure in junk*. FT Press, 2011.

[33] “DNA,” *Wikipedia*. 2018.

[34] C. Schildkraut and S. Lifson, “Dependence of the melting temperature of DNA on salt concentration,” *Biopolymers*, vol. 3, no. 2, pp. 195–208, 1965.

[35] C. R. Calladine, H. Drew, B. Luisi, and A. Travers, *Understanding DNA : the molecule and how it works*. Elsevier Academic Press, 2004.

[36] J. SantaLucia and D. Hicks, “The Thermodynamics of DNA Structural Motifs,” *Annu. Rev. Biophys. Biomol. Struct.*, vol. 33, no. 1, pp. 415–440, 2004.

[37] J. SantaLucia, “A unified view of polymer, dumbbell, and oligonucleotide DNA nearest-neighbor thermodynamics,” *Proc. Natl. Acad. Sci.*, vol. 95, no. 4, pp. 1460–1465, 1998.

[38] K. B. Mullis, F. Ferré, and R. Gibbs, *The Polymerase chain reaction*. Birkhäuser, 1994.

[39] M. Caruthers, “Gene synthesis machines: DNA chemistry and its uses,” *Science*

(80-), vol. 230, no. 4723, pp. 281–285, 1985.

[40] S. Brinkers, H. R. C. Dietrich, F. H. De Groote, I. T. Young, and B. Rieger, "The persistence length of double stranded DNA determined using dark field tethered particle motion," *J. Chem. Phys.*, vol. 130, no. 21, 2009.

[41] N. Geerts and E. Eiser, "DNA-functionalized colloids: Physical properties and applications," *Soft Matter*, vol. 6, no. 19, p. 4647, 2010.

[42] S. F. Wolf, L. Haines, J. Fisch, J. N. Kremsky, J. P. Dougherty, and K. Jacobs, "Rapid hybridization kinetics of DNA attached to submicron latex particles.," *Nucleic Acids Res.*, vol. 15, no. 7, pp. 2911–26, Apr. 1987.

[43] C. A. Mirkin, R. L. Letsinger, R. C. Mucic, and J. J. Storhoff, "A DNA-based method for rationally assembling nanoparticles into macroscopic materials," *Nature*, vol. 382, no. 6592. pp. 607–609, 1996.

[44] A. P. Alivisatos *et al.*, "Organization of 'nanocrystal molecules' using DNA.," *Nature*, vol. 382, no. 6592. pp. 609–11, 1996.

[45] J. Sharma, R. Chhabra, Y. Liu, Y. Ke, and H. Yan, "DNA-templated self-assembly of two-dimensional and periodical gold nanoparticle arrays," *Angew. Chemie - Int. Ed.*, vol. 45, no. 5, pp. 730–735, 2006.

[46] C. Zhang *et al.*, "A general approach to DNA-programmable atom equivalents," *Nat. Mater.*, vol. 12, no. 8, pp. 741–746, 2013.

[47] M. M. Maye, D. Nykypanchuk, D. Van Der Lelie, and O. Gang, "DNA-regulated micro- and nanoparticle assembly," *Small*, vol. 3, no. 10, pp. 1678–1682, 2007.

[48] L. Di Michele, "Multicomponent amorphous phases of DNA-functionalised colloids," 2013.

[49] S. Manley *et al.*, "Glasslike arrest in spinodal decomposition as a route to colloidal gelation," *Phys. Rev. Lett.*, vol. 95, no. 23, pp. 1–4, 2005.

[50] J. S. Oh, Y. Wang, D. J. Pine, and G. R. Yi, "High-Density PEO-b-DNA Brushes on Polymer Particles for Colloidal Superstructures," *Chem. Mater.*, vol. 27, no. 24, pp. 8337–8344, 2015.

[51] Y. Wang *et al.*, "Crystallization of DNA-coated colloids," *Nat. Commun.*, vol. 6, p. 7253, 2015.

[52] M. F. Hagan, O. M. Elrad, and R. L. Jack, "Mechanisms of kinetic trapping in self-

assembly and phase transformation," *J. Chem. Phys.*, vol. 135, no. 10, 2011.

[53] F. Varrato *et al.*, "Arrested demixing opens route to bigels.," *Proc. Natl. Acad. Sci. U. S. A.*, vol. 109, no. 47, pp. 19155–60, 2012.

[54] N. Geerts, T. Schmatko, and E. Eiser, "Clustering versus percolation in the assembly of colloids coated with long DNA," *Langmuir*, vol. 24, no. 9, pp. 5118–5123, 2008.

[55] L. Di Michele, D. Fiocco, F. Varrato, S. Sastry, E. Eiser, and G. Foffi, "Aggregation dynamics, structure, and mechanical properties of bigels," *Soft Matter*, vol. 10, no. 20, pp. 3633–3648, 2014.

[56] L. Di Michele, F. Varrato, J. Kotar, S. H. Nathan, G. Foffi, and E. Eiser, "Multistep kinetic self-assembly of DNA-coated colloids," *Nat. Commun.*, vol. 4, Jun. 2013.

[57] S. Hiki and K. Kataoka, "A facile synthesis of azido-terminated heterobifunctional poly (ethylene glycol) s for 'click' conjugation," *Bioconjug. Chem.*, vol. 18, no. 6, pp. 2191–2196, 2007.

[58] R. A. L. Jones, *Soft condensed matter*. Oxford University Press, 2002.

[59] I. Tinoco, "Hypochromism in Polynucleotides," *J. Am. Chem. Soc.*, vol. 82, no. 18, pp. 4785–4790, 1960.

[60] A. R. Hind, S. K. Bhargava, and A. McKinnon, "At the solid/liquid interface: FTIR/ATR - The tool of choice," *Adv. Colloid Interface Sci.*, vol. 93, no. 1–3, pp. 91–114, 2001.

[61] S. J. Hurst, A. K. R. Lytton-Jean, and C. A. Mirkin, "Maximizing DNA Loading on a Range of Gold Nanoparticle Sizes," *Anal Chem.*, vol. 78, no. 24, pp. 8313–8318, 2008.

[62] S. G. Lipson, H. Lipson, and D. S. Tannhauser, *Optical physics*. Cambridge University Press, 1995.

[63] J. Méring and D. Tchoubar, "Interprétation de la diffusion centrale des rayons X par les systèmes poreux," *J. Appl. Crystallogr.*, vol. 1, no. 3, pp. 153–165, 1968.

[64] P. Levitz and D. Tchoubar, "Disordered porous solids: from chord distributions to small angle scattering," *J. Phys. I*, vol. 2, no. 6, pp. 771–790, 1992.

[65] P. Levitz, "Toolbox for 3D imaging and modeling of porous media: Relationship with transport properties," *Cem. Concr. Res.*, vol. 37, no. 3, pp. 351–359, Mar.

2007.

[66] P. J. Lu *et al.*, "Characterizing concentrated, multiply scattering, and actively driven fluorescent systems with confocal differential dynamic microscopy," *Phys. Rev. Lett.*, vol. 108, no. 21, pp. 1–5, 2012.

[67] F. Ferri *et al.*, "Kinetics of colloidal fractal aggregation by differential dynamic microscopy," *Eur. Phys. J. Spec. Top.*, vol. 199, no. 1, pp. 139–148, 2011.

[68] L. G. Wilson *et al.*, "Differential dynamic microscopy of bacterial motility," *Phys. Rev. Lett.*, vol. 106, no. 1, pp. 7–10, 2011.

[69] E. Eiser, "Dynamic Light Scattering," in *Multi Length-Scale Characterisation*, Chichester, UK: John Wiley & Sons, Ltd, 2013, pp. 233–282.

[70] H. Kawaguchi, "Functional polymer microspheres," *Prog. Polym. Sci.*, vol. 25, no. 8, pp. 1171–1210, 2000.

[71] J. P. Rao and K. E. Geckeler, "Polymer nanoparticles: Preparation techniques and size-control parameters," *Prog. Polym. Sci.*, vol. 36, no. 7, pp. 887–913, 2011.

[72] C. E. Reese, C. D. Guerrero, J. M. Weissman, K. Lee, and S. A. Asher, "Synthesis of highly charged, monodisperse polystyrene colloidal particles for the fabrication of photonic crystals," *J. Colloid Interface Sci.*, vol. 232, no. 1, pp. 76–80, 2000.

[73] J. A. Champion, Y. K. Katare, and S. Mitragotri, "Particle shape: A new design parameter for micro- and nanoscale drug delivery carriers," *J. Control. Release*, vol. 121, no. 1–2, pp. 3–9, 2007.

[74] S. Brahim, D. Narinesingh, and A. Guiseppi-Elie, "Amperometric determination of cholesterol in serum using a biosensor of cholesterol oxidase contained within a polypyrrole-hydrogel membrane," *Anal. Chim. Acta*, vol. 448, no. 1–2, pp. 27–36, 2001.

[75] P. York, "Strategies for particle design using supercritical fluid technologies," *Pharm. Sci. Technol. Today*, vol. 2, no. 11, pp. 430–440, 1999.

[76] H. Fudouzi and Y. Xia, "Photonic papers and inks: Color writing with colorless materials," *Adv. Mater.*, vol. 15, no. 11, pp. 892–896, 2003.

[77] D. V. Talapin, J.-S. Lee, M. V. Kovalenko, and E. V. Shevchenko, "Prospects of Colloidal Nanocrystals for Electronic and Optoelectronic Applications," *Chem. Rev.*, vol. 110, no. 1, pp. 389–458, 2010.

[78] J. M. Asua, "Miniemulsion polymerization," *Prog. Polym. Sci.*, vol. 27, no. 7, pp. 1283–1346, 2002.

[79] N. Anton, J. P. Benoit, and P. Saulnier, "Design and production of nanoparticles formulated from nano-emulsion templates-A review," *J. Control. Release*, vol. 128, no. 3, pp. 185–199, 2008.

[80] S. C. Thickett and R. G. Gilbert, "Emulsion polymerization: State of the art in kinetics and mechanisms," *Polymer (Guildf).*, vol. 48, no. 24, pp. 6965–6991, 2007.

[81] G. Kim, S. Lim, B. H. Lee, S. E. Shim, and S. Choe, "Effect of homogeneity of methanol/water/monomer mixture on the mode of polymerization of MMA: Soap-free emulsion polymerization versus dispersion polymerization," *Polymer (Guildf).*, vol. 51, no. 5, pp. 1197–1205, 2010.

[82] G. R. Bardajee, C. Vancaeyzeele, J. C. Haley, A. Y. Li, and M. A. Winnik, "Synthesis, characterization, and energy transfer studies of dye-labeled poly(butyl methacrylate) latex particles prepared by miniemulsion polymerization," *Polymer (Guildf).*, vol. 48, no. 20, pp. 5839–5849, 2007.

[83] S. W. Kim, H. G. Cho, and C. R. Park, "Fabrication of unagglomerated polypyrrole nanospheres with controlled sizes from a surfactant-free emulsion system," *Langmuir*, vol. 25, no. 16, pp. 9030–9036, 2009.

[84] T. Ding, E. S. Daniels, M. S. El-Aasser, and A. Klein, "Synthesis and characterization of functionalized polymer latex particles through a designed semicontinuous emulsion polymerization process," *J. Appl. Polym. Sci.*, vol. 97, no. 1, pp. 248–256, 2005.

[85] J. Lei and G. Zhou, "Polystyrene microbeads by dispersion polymerization: Effect of solvent on particle morphology," *Int. J. Polym. Sci.*, vol. 2014, 2014.

[86] C. K. Ober and Kar P. Lok, "Particle size control in dispersion polymerization of polystyrene," *Can. J. Chem.*, vol. 63, no. 1, p. 8, 1985.

[87] G. H. Koenderink, S. Sacanna, C. Pathmamanoharan, M. Raşa, and A. P. Philipse, "Preparation and Properties of Optically Transparent Aqueous Dispersions of Monodisperse Fluorinated Colloids," *Langmuir*, vol. 17, no. 20, pp. 6086–6093, Oct. 2001.

[88] S. Sacanna, G. H. Koenderink, and A. P. Philipse, "Microemulsion Synthesis of

Fluorinated Latex Spheres," *Langmuir*, vol. 20, no. 19, pp. 8398–8400, 2004.

[89] G. T. Hermanson, *Bioconjugate techniques*. Academic Press, 2008.

[90] Z. Ruff *et al.*, "Designing disordered materials using DNA-coated colloids of bacteriophage fd and gold," *Faraday Discuss.*, pp. 473–488, 2016.

[91] S. V. Orski, G. R. Sheppard, S. Arumugam, R. M. Arnold, V. V. Popik, and J. Locklin, "Rate determination of azide click reactions onto alkyne polymer brush scaffolds: A comparison of conventional and catalyst-free cycloadditions for tunable surface modification," *Langmuir*, vol. 28, no. 41, pp. 14693–14702, 2012.

[92] A. J. Kim, P. L. Biancaniello, and J. C. Crocker, "Engineering DNA-mediated colloidal crystallization," *Langmuir*, vol. 22, no. 5, pp. 1991–2001, 2006.

[93] P. Alexandridis and T. Alan Hatton, "Poly(ethylene oxide)poly(propylene oxide)poly(ethylene oxide) block copolymer surfactants in aqueous solutions and at interfaces: thermodynamics, structure, dynamics, and modeling," *Colloids Surfaces A Physicochem. Eng. Asp.*, vol. 96, no. 1–2, pp. 1–46, 1995.

[94] E. Lieber, C. N. R. Rao, T. S. Chao, and C. W. W. Hoffman, "Infrared Spectra of Organic Azides," *Anal. Chem.*, vol. 29, no. 6, pp. 916–918, 1957.

[95] F. Kienberger *et al.*, "Static and Dynamical Properties of Single Poly(Ethylene Glycol) Molecules Investigated by Force Spectroscopy," *Single Mol.*, vol. 1, no. 2, pp. 123–128, 2000.

[96] H. Lee, R. M. Venable, A. D. MacKerell, and R. W. Pastor, "Molecular dynamics studies of polyethylene oxide and polyethylene glycol: Hydrodynamic radius and shape anisotropy," *Biophys. J.*, vol. 95, no. 4, pp. 1590–1599, 2008.

[97] K. Binder and A. Milchev, "Polymer brushes on flat and curved surfaces: How computer simulations can help to test theories and to interpret experiments," *J. Polym. Sci. Part B Polym. Phys.*, vol. 50, no. 22, pp. 1515–1555, 2012.

[98] P. G. de Gennes, "Conformations of Polymers Attached to an Interface," *Macromolecules*, vol. 13, no. 5, pp. 1069–1075, 1980.

[99] B. Tinland, A. Pluen, J. Sturm, G. Weill, and I. C. Sadron-cnrs-universite, "Persistence Length of Single-Stranded DNA," vol. 9297, no. 97, pp. 5763–5765, 1997.

[100] J. Lee, C. K. Hong, S. Choe, and S. E. Shim, "Synthesis of polystyrene/silica

composite particles by soap-free emulsion polymerization using positively charged colloidal silica," *J. Colloid Interface Sci.*, vol. 310, no. 1, pp. 112–120, 2007.

[101] M. R. Ferrick, J. Murtagh, and J. K. Thomas, "Synthesis and Characterization of Polystyrene Latex Particles," *Macromolecules*, vol. 22, no. 4, pp. 1515–1517, 1989.

[102] E. Zaccarelli, "Colloidal gels: Equilibrium and non-equilibrium routes," *J. Phys. Condens. Matter*, vol. 19, no. 32, 2007.

[103] L. Cipelletti *et al.*, "Universal non-diffusive slow dynamics in aging soft matter," *Faraday Discuss.*, vol. 123, pp. 237–251, 2003.

[104] D. Nykypanchuk, M. M. Maye, D. van der Lelie, and O. Gang, "DNA-guided crystallization of colloidal nanoparticles.," *Nature*, vol. 451, no. 7178, pp. 549–552, 2008.

[105] P. J. Lu, E. Zaccarelli, F. Ciulla, A. B. Schofield, F. Sciortino, and D. A. Weitz, "Gelation of particles with short-range attraction," *Nature*, vol. 453, no. 7194, pp. 499–503, 2008.

[106] S. Y. Park, A. K. R. Lytton-Jean, B. Lee, S. Weigand, G. C. Schatz, and C. A. Mirkin, "DNA-programmable nanoparticle crystallization.," *Nature*, vol. 451, no. 7178, pp. 553–6, 2008.

[107] L. Di Michele and E. Eiser, "Developments in understanding and controlling self assembly of DNA-functionalized colloids," *Phys. Chem. Chem. Phys.*, vol. 15, no. 9, p. 3115, 2013.

[108] Z. Ruff, P. Cloetens, T. O'Neill, C. P. Grey, and E. Eiser, "Thermally reversible nanoparticle gels with tuneable porosity showing structural colour," *Phys. Chem. Chem. Phys.*, vol. 20, pp. 467–477, 2017.

[109] S. Ashdown, I. Markovic, R. H. Ottewill, P. Lindner, R. C. Oberthur, and A. R. Rennie, "Small-angle neutron-scattering studies on ordered polymer colloid dispersions," *Langmuir*, vol. 6, no. 2, pp. 303–307, 1990.

[110] P. N. Pusey and W. van Megen, "Phase behavior of concentrated suspensions of nearly hard colloidal spheres," *Nature*, vol. 320, no. 6060, pp. 340–342, 1986.

[111] E. B. Sirota, H. D. Ou-Yang, S. K. Sinha, P. M. Chaikin, J. D. Axe, and Y. Fujii, "Complete phase diagram of a charged colloidal system: A synchrotron x-ray

scattering study," *Phys. Rev. Lett.*, vol. 62, no. 13, pp. 1524–1527, 1989.

[112] A. P. Leis, S. Schlicher, H. Franke, and M. Strathmann, "Optically Transparent Porous Medium for Nondestructive Studies of Microbial Biofilm Architecture and Transport Dynamics," vol. 71, no. 8, pp. 4801–4808, 2005.

[113] L. M. McDowell-Boyer, J. R. Hunt, and N. Sitar, "Particle Transport Through Porous Media," *Water Resour. Res.*, vol. 22, no. 13, pp. 1901–1921, 1986.

[114] R.-X. Yang, T.-T. Wang, and W.-Q. Deng, "Extraordinary capability for water treatment achieved by a perfluorous conjugated microporous polymer.," *Sci. Rep.*, vol. 5, no. April, p. 10155, 2015.

[115] H. M. van der Kooij and J. Sprakel, "Watching paint dry; more exciting than it seems.," *Soft Matter*, vol. 11, pp. 6353–6359, 2015.

[116] M. Zupkauskas, Y. Lan, D. Joshi, Z. Ruff, and E. Eiser, "Optically Transparent Dense Colloidal Gels," *Chem. Sci.*, vol. 8, no. 8, pp. 5559–5566, 2017.

[117] Z. Ruff *et al.*, "Designing disordered materials using DNA-coated colloids of bacteriophage fd and gold," *Faraday Discuss.*, 2015.

[118] V. Testard, L. Berthier, and W. Kob, "Influence of the glass transition on the liquid-gas spinodal decomposition," *Phys. Rev. Lett.*, vol. 106, no. 12, pp. 1–4, 2011.

[119] P. Levitz, "Off-lattice reconstruction of porous media: critical evaluation, geometrical confinement and molecular transport," *Adv. Colloid Interface Sci.*, vol. 76–77, pp. 71–106, 1998.

[120] P. L. Biancaniello, A. J. Kim, and J. C. Crocker, "Colloidal interactions and self-assembly using DNA hybridization," *Phys. Rev. Lett.*, vol. 94, no. 5, pp. 94–97, 2005.

[121] J. Happel and H. Brenner, *Low Reynolds number hydrodynamics*, vol. 1. Dordrecht: Springer Netherlands, 1981.

[122] A. E. Cervantes-Martínez, A. Ramírez-Saito, R. Armenta-Calderón, M. A. Ojeda-López, and J. L. Arauz-Lara, "Colloidal diffusion inside a spherical cell," *Phys. Rev. E - Stat. Nonlinear, Soft Matter Phys.*, vol. 83, no. 3, pp. 1–4, 2011.

[123] T. F. Tadros, "Emulsion Formation, Stability, and Rheology," in *Emulsion Formation and Stability*, T. F. Tadros, Ed. John Wiley & Sons, 2013, p. 272.

[124] B. P. Binks and R. Murakami, "Phase inversion of particle-stabilized materials from foams to dry water," *Nat. Mater.*, vol. 5, no. 11, pp. 865–869, 2006.

[125] V. N. Manoharan, M. T. Elsesser, and D. J. Pine, "Dense Packing and Symmetry in Small Clusters of Microspheres," *Science (80-)*, vol. 301, no. 5632, pp. 483–487, Jul. 2003.

[126] L. D. Zarzar, V. Sresht, E. M. Sletten, J. a Kalow, D. Blankschtein, and T. M. Swager, "Dynamically reconfigurable complex emulsions via tunable interfacial tensions.," *Nature*, vol. 518, no. 7540, pp. 520–4, 2015.

[127] S. Tsuji and H. Kawaguchi, "Thermosensitive pickering emulsion stabilized by poly(N- isopropylacrylamide)-carrying particles," *Langmuir*, vol. 24, no. 7, pp. 3300–3305, 2008.

[128] L. B. Maçon, S. U. Rehman, R. V Bell, and J. V. M. Weaver, "Reversible assembly of pH responsive branched copolymer-stabilised emulsion via electrostatic forces.," *Chem. Commun.* , vol. 52, no. 1, pp. 136–9, 2015.

[129] Y. Zhang *et al.*, "Sequential self-assembly of DNA functionalized droplets," *Nat. Commun.*, vol. 8, no. 1, p. 21, Dec. 2017.

[130] M. Hadorn, E. Boenzli, K. T. Sørensen, H. Fellermann, P. Eggenberger, and M. M. Hanczyc, "Specific and reversible DNA-directed self-assembly of oil-in-water emulsion droplets," *Proc. Natl. Acad. Sci.*, vol. 109, no. 50, pp. 20320–20325, 2012.

[131] L. Feng, L.-L. Pontani, R. Dreyfus, P. Chaikin, and J. Brujic, "Specificity, flexibility and valence of DNA bonds guide emulsion architecture," *Soft Matter*, vol. 9, no. 41, p. 9816, 2013.

[132] D. Joshi *et al.*, "Kinetic control of the coverage of oil droplets by DNA-functionalized colloids," *Sci. Adv.*, vol. 2, no. 8, 2016.

[133] M. Hadorn, E. Boenzli, and M. M. Hanczyc, "Specific and Reversible DNA-Directed Self-Assembly of Modular Vesicle-Droplet Hybrid Materials," *Langmuir*, vol. 32, no. 15, pp. 3561–3566, Apr. 2016.

[134] L. Parolini, B. M. Mognetti, J. Kotar, E. Eiser, P. Cicuta, and L. Di Michele, "Volume and porosity thermal regulation in lipid mesophases by coupling mobile ligands to soft membranes.," *Nat. Commun.*, vol. 6, p. 5948(1)-5948(10), 2015.

[135] A. Caciagli *et al.*, "DNA-Coated Functional Oil Droplets," *Langmuir*, vol. 34, no. 34, pp. 10073–10080, 2018.

[136] M. J. Schick, *Nonionic Surfactants : Physical Chemistry*. CRC Press, 1987.

[137] E. Egidi, G. Gasparini, R. G. Holdich, G. T. Vladisavljević, and S. R. Kosvintsev, "Membrane emulsification using membranes of regular pore spacing: Droplet size and uniformity in the presence of surface shear," *J. Memb. Sci.*, vol. 323, no. 2, pp. 414–420, 2008.

[138] C. Charcosset, I. Limayem, and H. Fessi, "The membrane emulsification process - A review," *Journal of Chemical Technology and Biotechnology*, vol. 79, no. 3. pp. 209–218, 2004.

[139] J. P. Canselier, H. Delmas, A. M. Wilhelm, and B. Abismaïl, "Ultrasound Emulsification—An Overview," *J. Dispers. Sci. Technol.*, vol. 23, no. 1–3, pp. 333–349, 2002.

[140] R. K. Shah *et al.*, "Designer emulsions using microfluidics," *Materials Today*, vol. 11, no. 4. pp. 18–27, 2008.

[141] G. T. Vladisavljević, I. Kobayashi, and M. Nakajima, "Production of uniform droplets using membrane, microchannel and microfluidic emulsification devices," *Microfluidics and Nanofluidics*, vol. 13, no. 1. pp. 151–178, 2012.

[142] A. Gupta, H. B. Eral, T. A. Hatton, and P. S. Doyle, "Nanoemulsions: formation, properties and applications," *Soft Matter*, vol. 12, no. 11, pp. 2826–2841, 2016.

[143] C. Solans, P. Izquierdo, J. Nolla, N. Azemar, and M. J. Garcia-Celma, "Nano-emulsions," *Current Opinion in Colloid and Interface Science*, vol. 10, no. 3–4. pp. 102–110, 2005.

[144] M. Kukizaki, "Shirasu porous glass (SPG) membrane emulsification in the absence of shear flow at the membrane surface: Influence of surfactant type and concentration, viscosities of dispersed and continuous phases, and transmembrane pressure," *J. Memb. Sci.*, vol. 327, no. 1–2, pp. 234–243, Feb. 2009.

[145] D. M. Lloyd, I. T. Norton, and F. Spyropoulos, "Processing effects during rotating membrane emulsification," *J. Memb. Sci.*, vol. 466, pp. 8–17, 2014.

[146] P. Taylor, "Ostwald ripening in emulsions," *Adv. Colloid Interface Sci.*, vol. 75, no. 2, pp. 107–163, Apr. 1998.

[147] C. Holtze *et al.*, "Biocompatible surfactants for water-in-fluorocarbon emulsions," *Lab Chip*, vol. 8, no. 10, p. 1632, 2008.

[148] T. S. H. Leong, T. J. Wooster, S. E. Kentish, and M. Ashokkumar, "Minimising oil droplet size using ultrasonic emulsification," *Ultrason. Sonochem.*, vol. 16, no. 6, pp. 721–727, 2009.

[149] S. G. Gaikwad and A. B. Pandit, "Ultrasound emulsification: Effect of ultrasonic and physicochemical properties on dispersed phase volume and droplet size," *Ultrason. Sonochem.*, vol. 15, no. 4, pp. 554–563, 2008.

[150] A. J. O'Lenick, "Silicone emulsions and surfactants," *J. Surfactants Deterg.*, vol. 3, no. 3, pp. 387–393, 2000.

[151] T. Yanagishima, D. Michele, and E. Eiser, "Diffusive behaviour of PLL – PEG coated colloids on l -DNA brushes – tuning hydrophobicity," pp. 6792–6798, 2012.

[152] N. Patra and A. V. Tkachenko, "Layer-by-layer assembly of patchy particles as a route to nontrivial structures," *Phys. Rev. E*, vol. 96, no. 2, p. 022601, Aug. 2017.

[153] A. V. Tkachenko, "Theory of programmable hierarchic self-assembly," *Phys. Rev. Lett.*, vol. 106, no. 25, 2011.

[154] C. Chen, R. A. L. Wylie, D. Klinger, and L. A. Connal, "Shape Control of Soft Nanoparticles and Their Assemblies," *Chem. Mater.*, vol. 29, no. 5, pp. 1918–1945, 2017.

[155] Y. Wang *et al.*, "Colloids with valence and specific directional bonding," *Nature*, vol. 491, no. 7422, pp. 51–55, 2012.

[156] D. J. Pine and A. Imhof, "Ordered macroporous materials by emulsion templating," *Nature*, vol. 389, no. 6654, pp. 948–951, 1997.

[157] S. Roldán-Vargas, F. Smallenburg, W. Kob, and F. Sciortino, "Gelling by Heating," *Sci. Rep.*, vol. 3, no. 1, p. 2451, 2013.

[158] R. O. Prum and R. H. Torres, "A Fourier Tool for the Analysis of Coherent Light Scattering by Bio-Optical Nanostructures 1," *Integr. Comp. Biol*, vol. 43, pp. 591–602, 2003.

[159] J. Zhang, Z. Sun, and B. Yang, "Self-assembly of photonic crystals from polymer colloids," *Curr. Opin. Colloid Interface Sci.*, vol. 14, no. 2, pp. 103–114, 2009.

[160] Y. Zhao *et al.*, “Multifunctional photonic crystal barcodes from microfluidics,” *NPG Asia Mater.*, vol. 4, no. 9, pp. e25-7, 2012.

[161] S. Furumi, H. Fudouzi, and T. Sawada, “Self-organized colloidal crystals for photonics and laser applications,” *Laser Photonics Rev.*, vol. 4, no. 2, pp. 205–220, 2010.

[162] F. S. Diana *et al.*, “Photonic crystal-assisted light extraction from a colloidal quantum Dot/GaN hybrid structure,” *Nano Lett.*, vol. 6, no. 6, pp. 1116–1120, 2006.

[163] H. Wang and K. Q. Zhang, “Photonic crystal structures with tunable structure color as colorimetric sensors,” *Sensors (Switzerland)*, vol. 13, no. 4, pp. 4192–4213, 2013.

[164] B. J. Alder and T. E. Wainwright, “Phase transition for a hard sphere system,” *J. Chem. Phys.*, vol. 27, no. 5, pp. 1208–1209, 1957.

[165] D. Gottwald, C. N. Likos, G. Kahl, and H. Löwen, “Phase Behavior of Ionic Microgels,” *Phys. Rev. Lett.*, vol. 92, no. 6, pp. 4–7, 2004.

[166] A. Yethiraj and A. Van Blaaderen, “A colloidal model system with an interaction tunable from hard sphere to soft and dipolar,” *Nature*, vol. 421, no. 6922, pp. 513–517, 2003.

[167] D. M. Heyes and A. C. Brańka, “Interactions between microgel particles,” *Soft Matter*, vol. 5, no. 14, p. 2681, 2009.

[168] T. T. Ngo, C. M. Liddell, M. Ghebrebrhan, and J. D. Joannopoulos, “Tetrastack: Colloidal diamond-inspired structure with omnidirectional photonic band gap for low refractive index contrast,” *Appl. Phys. Lett.*, vol. 88, no. 24, pp. 1–4, 2006.

[169] I. Tarhan and G. Watson, “Photonic band structure of fcc colloidal crystals.,” *Phys. Rev. Lett.*, vol. 76, no. 2, pp. 315–318, 1996.

[170] C. E. Finlayson *et al.*, “Interplay of index contrast with periodicity in polymer photonic crystals,” *Appl. Phys. Lett.*, vol. 99, no. 26, 2011.

[171] C. F. Lai, C. L. Hsieh, and C. J. Wu, “Light-spectrum modification of warm white-light-emitting diodes with 3D colloidal photonic crystals to approximate candlelight,” *Opt Lett*, vol. 38, no. 18, pp. 3612–3615, 2013.

[172] T. Erdem *et al.*, “Tunable colloidal photonic crystals,” Aug. 2018.

[173] N. Geerts, S. Jahn, and E. Eiser, “Direct observation of size fractionation during colloidal crystallization.,” *J. Phys. Condens. Matter*, vol. 22, no. 10, p. 104111, 2010.

[174] Z. Dogic and S. Fraden, “Smectic Phase in a Colloidal Suspension of Semi exible Virus Particles,” *Prl*, vol. 78, no. 12, pp. 2417–2420, 1997.

[175] D. A. Marvin, R. D. Hale, C. Nave, and M. H. Citterich, “Molecular models and structural comparisons of native and mutant class I filamentous bacteriophages. Ff (fd, f1, M13), If1 and IKe,” *J. Mol. Biol.*, vol. 235, no. 1, pp. 260–286, 1994.

[176] R. R. Unwin *et al.*, “DNA driven self-assembly of micron-sized rods using DNA-grafted bacteriophage fd virions,” *Phys. Chem. Chem. Phys.*, vol. 17, no. 12, pp. 8194–8202, 2015.

[177] J. Bergenholtz, W. C. K. Poon, and M. Fuchs, “Gelation in model colloid-polymer mixtures,” *Langmuir*, vol. 19, no. 10, pp. 4493–4503, 2003.

10 APPENDICES

$PS_{(30)}$-$PEG_{(79)}$-N_3 DIBLOCK COPOLYMER SYNTHESIS

This synthesis was performed by Dr Clément Mugemana and Prof Nico Bruns at the Adolphe Merkle Institute.

All chemicals and solvents (purity > 95%) were purchased from Sigma-Aldrich. CDCl3 was purchased from Cambridge Isotope Laboratories Inc. Azide end-functionalized polyethylene glycol (M_n= 3300 g/mol, degree of polymerization = 75, Đ = 1.07) was purchased from RAPP Polymere. The styrene monomer was passed through a neutral aluminium oxide column to remove the inhibitor before the polymerization.

^{1}H NMR spectroscopy was measured on a Bruker 300 MHz Avance III spectrometer using $CDCl_3$ as solvent. Size-exclusion chromatography (SEC) experiments were performed on an Agilent 1200 series HPLC system equipped with an Agilent PLgel mixed guard column (particle size = 5 µm) and two Agilent PLgel mixed-D columns (ID = 7.5 mm, L = 300 mm, particle size = 5 µm). Signals were recorded by a UV detector (Agilent 1200 series), an Optilab REX interferometric refractometer, and a mini Dawn TREOS light scattering detector (Wyatt Technology Corp.). Samples were run using THF as the eluent at 30 °C and a flow rate of 1.0 ml/min. Data analysis was performed on Astra software (Wyatt Technology Corp.) and molecular weights were determined based on narrow-molecular-weight polystyrene calibration (from 2340 to 364000 g/mol). FT-IR spectra were recorded on PerkinElmer Spectrum 65 equipped with an attenuated total reflection (ATR) measuring device.

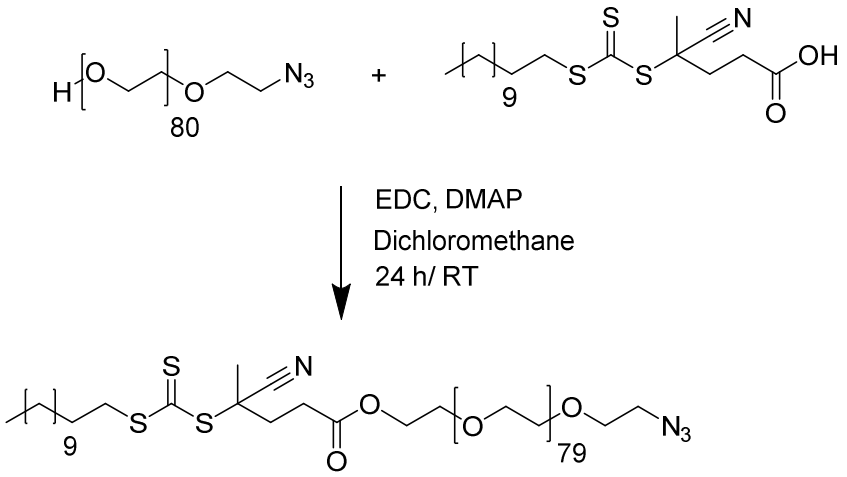

Synthesis of azide-PEG-chain transfer agent (N_3-PEG-CTA).

The synthesis of the CTA-functionalised PEG was adapted from literature (R. Palao-Suay, M. R. Aguilar, F. J. Parra-Ruiz, S. Maji, R. Hoogenboom, N. A. Rohner, S. N. Thomas, J. San Román, *Polym. Chem*. 2016, 7, 838). Azide-functionalised polyethylene

glycol (0.4 g, 0.13 mmol, 1 eq.) and 4-cyano-4-[(dodecyl-sulfanylthiocarbonyl)sulfanyl]pentanoic acid (0.08 g, 0.2 mmol, 1.5 eq.) were introduced in a 50 ml round-bottom flask under nitrogen atmosphere and dissolved in 7 ml of dry dichloromethane (DCM). The flask was then placed in an ice bath. 1-Ethyl-3-(3-dimethylaminopropyl)carbodiimide (38 mg, 0.2 mmol, 1.5 eq.) was dissolved in 3 ml of dry DCM and added dropwise to the reaction mixture under gentle stirring. 4-(Dimethylamino)pyridine (density: 0.884 g/cm^3 and purity of 99%) (2.7 ml, 16 µmol, 0.12 eq.) was added in the same manner. The round-bottom flask was then removed from the ice bath, and the reaction mixture was stirred for 24 h at room temperature under nitrogen atmosphere. After the reaction, the solution mixture was concentrated (to yield a viscous solution) under reduced pressure using a rotary evaporator. The polymer was then precipitated into diethyl ether and dried under vacuum. The yield of the reaction was 75% (0.3 g). ^{1}H NMR (400 MHz, $CDCl_3$): δ_H 4.24 ppm (t, 2.0H, h); 3.89 ppm (t, 1.7H, i); 3.64 ppm (s, 320H, j+k); 3.38 ppm (t, 3.1H, l); 3.32 ppm (t, 2.1 H, g); 2.66 ppm (t, 2.0H, f); 2.49 ppm +2.37 ppm (m, 2.5H, d); 1.87 ppm (s, 3.0H, e); 1.83 ppm (s, water); 1.69 ppm (t, 2.6H, c), 1.25 ppm (s, 18.6H, b), 0.87 ppm (t, 3.3H, a); degree of polymerisation (PEG) = 80; M_n= 3920 g/mol. GPC (calibration against PS): N3-PEG-CTA: M_n= 5212 g/mol, M_w= 5733 g/mol; Đ= 1.1; FT-IR: ν = 2970-2680, 2095, 2035, 1736, 1465, 1340, 1275, 1241, 1150, 1108, 1065, 954, 840 cm^{-1}.

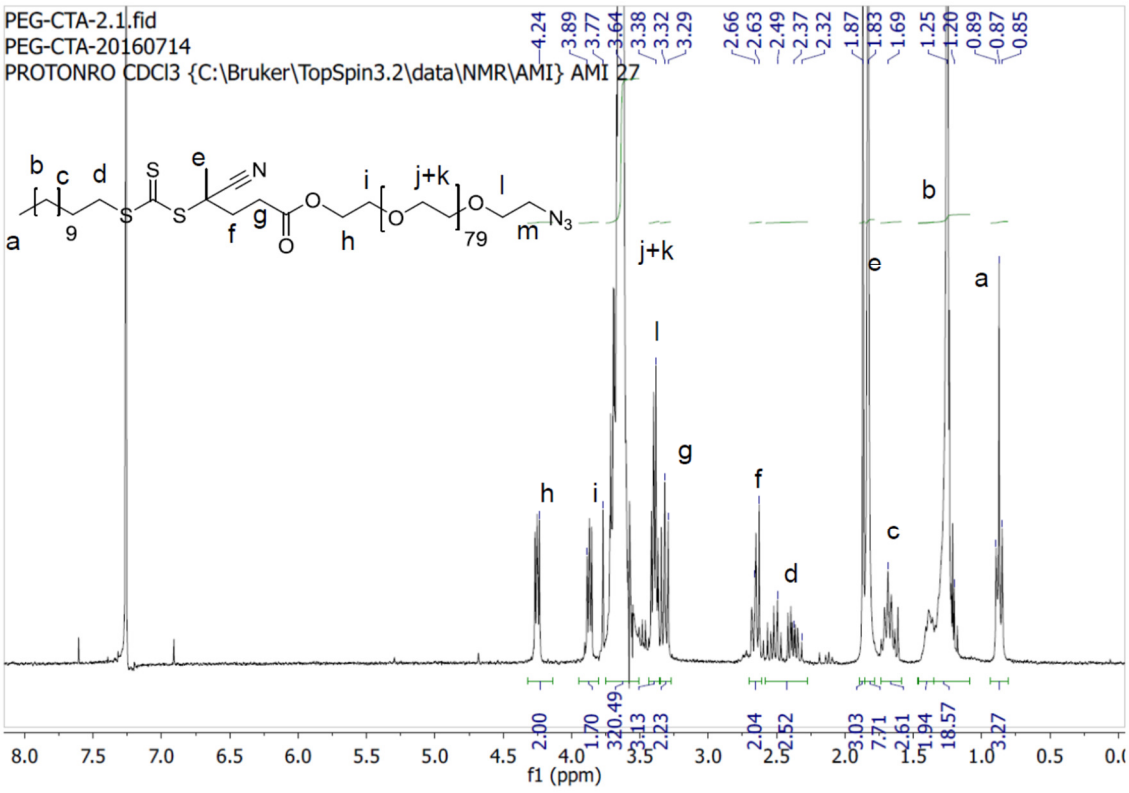

^{1}H NMR spectrum of N_3-PEG-CTA.

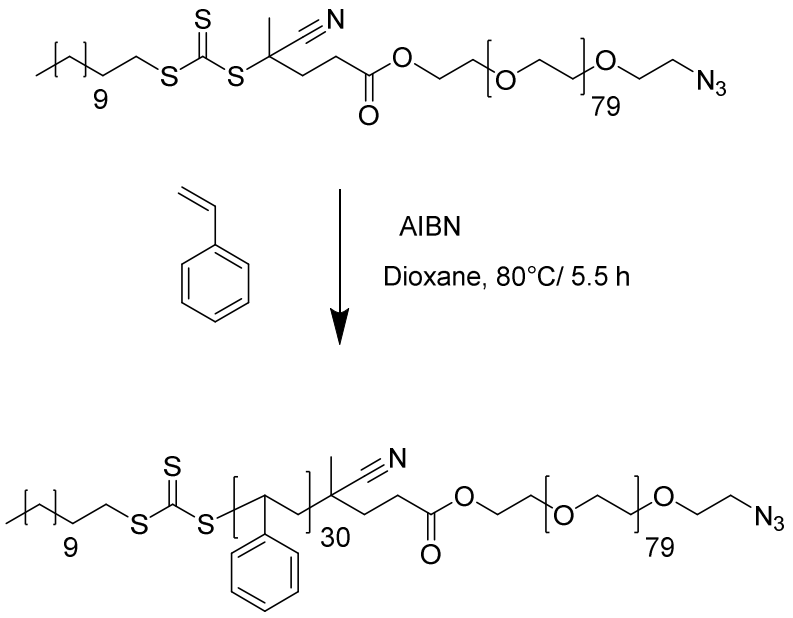

Synthesis of polystyrene-block-PEG-azide ($PS_{(30)}$-b-$PEG_{(79)}$-N_3).

N_3-PEG-CTA (0.2 g, 59 µmol, 1 eq.) was introduced in a dry Schlenk tube containing a magnetic stirring bar. Styrene (0.676 ml, 0.612 g, 5.882 mmol, 100 eq.) and AIBN (2.4 mg; 14.7 µmol; 0.25 eq.) were added and the mixture was dissolved in 0.9 ml dry dioxane. The solution underwent 3 cycles of freeze-pump-thaw cycles to remove oxygen. The flask was then filled with argon and immersed in an oil bath heated at 80°C for 5 ½ hours. After the reaction, the Schlenk tube was transferred to a cold water bath to quench the polymerization, and the solution was concentrated using a rotary evaporator. The block copolymer was precipitated into diethyl ether and dried under vacuum. The yield of the reaction was 65% (0.25 g). ^{1}H NMR (400 MHz, $CDCl_3$): δ_H 7.25-6.25 ppm (broad, 153.9H, a); 5.78-5.72 and 5.26-5.23 ppm (residual vinylic protons of styrene); 4.17 ppm (broad, 1.5H, d); 3.86 ppm (t, 2.0H, e) 3.52 ppm (s, 320H, c); 2.10-1.25 ppm (broad, 142, b + f); degree of polymerisation (PEG) = 80; degree of polymerization (PS) = 30; Mn= 6923 g/mol. GPC (calibration against PS): N_3-PEG-CTA: M_n= 5212 g/mol, M_w= 5733 g mol-1; Đ= 1.1; PS-b-PEG-N_3: M_n = 10490 g/mol, M_w = 12380 g/mol, Đ = 1.18. FT-IR: ν = 2700-3120, 1960, 1745, 1605 1454, 1340, 1280, 1240, 1110, 965, 843, 760, 700, 540 cm^{-1}.

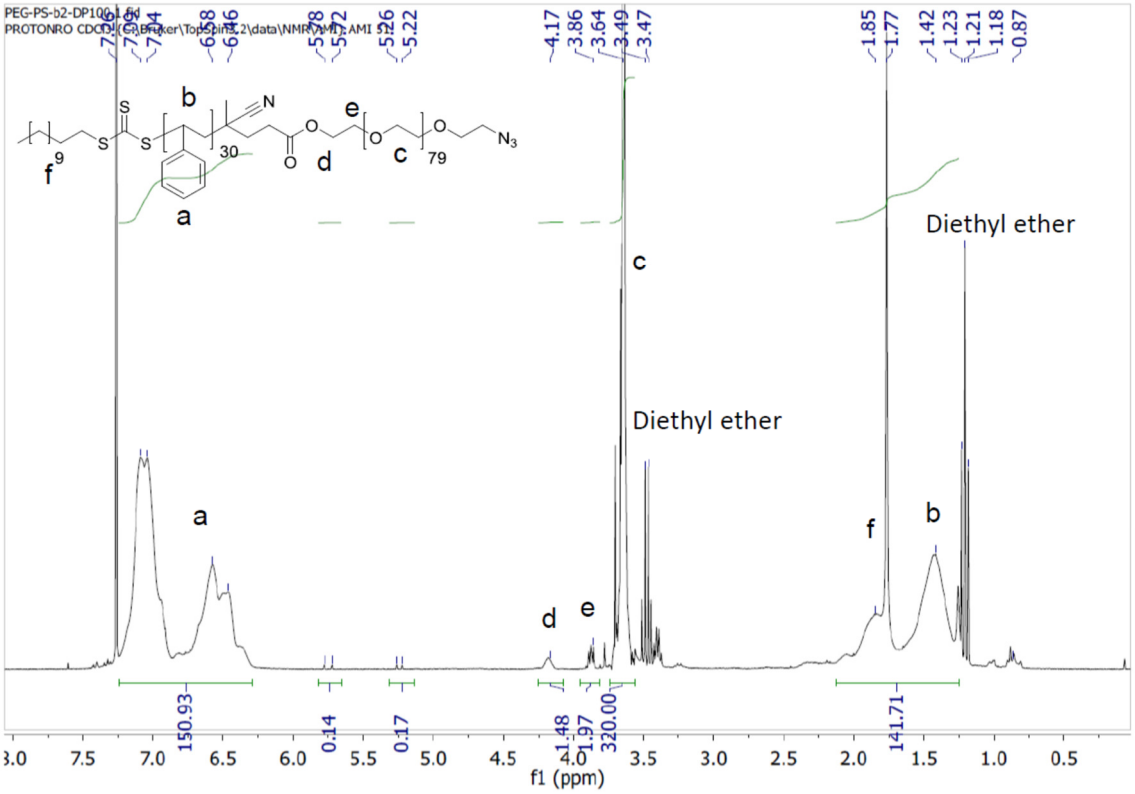

^{1}H NMR spectrum of $PS_{(30)}$-b-$PEG_{(79)}$-N_3.

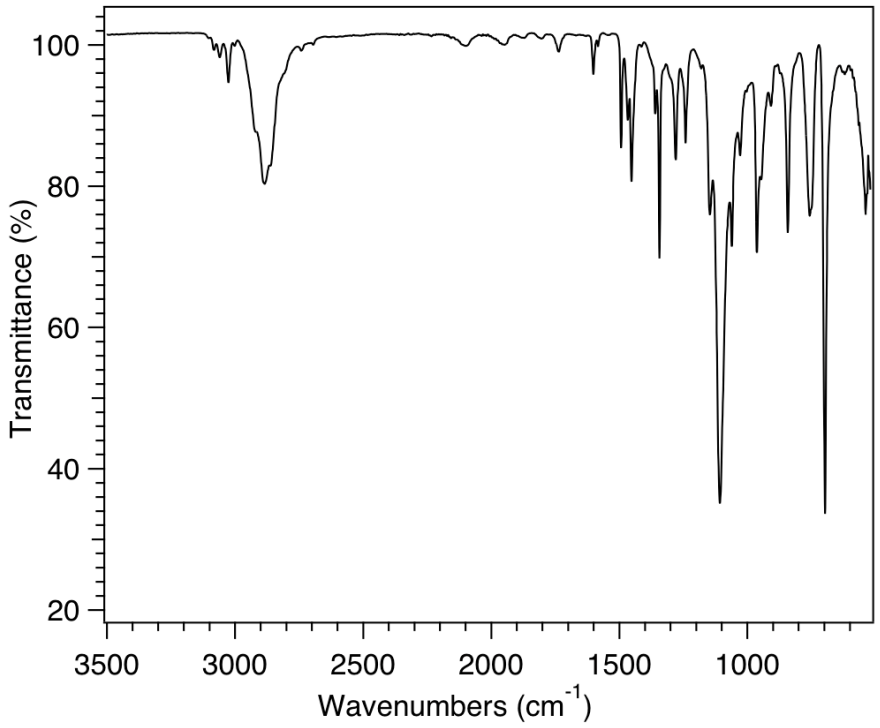

FT-IR spectrum of $PS_{(30)}$-b-$PEG_{(79)}$-N_3.

OD SIZE DISTRIBUTION: ANALYSIS

The experiments were performed by A. Caciagli and the present author. The MATLAB programme was written by A. Caciagli.

DLS was employed to analyse the size of the nanoemulsions obtained by ultrasound emulsification. DLS experiments were performed with a Malvern Zetasizer Nano ZSP. In order to verify the consistency of the results, three independent measurements, each consisting of 15 runs, were carried out for each sample. The results reported all show consistency relative to this procedure.

Video image analysis was employed to analyse the size of the microemulsions obtained by both microfluidics and membrane emulsification. Optical microscopy was done using the equipment described in Chapter 2.4.7. For the segmentation of the droplets and the determination of their size, a custom program based on the Canny edge detector was implemented in MATLAB. The method, adapted from Akella et al. (S. V. Akella, A. Mowitz, M. Heymann, S. Fraden, *Cryst. Growth Des.* 2014, 14, 4487.) employs the following strategy:

1. Original image.
2. Contrast enhancement via Contrast Limited Adaptive Histograph Equalization (CLAHE).
3. Low-pass filtering by pixel averaging.
4. High pass filtering by background subtraction & CLAHE.
5. Binarization via Canny edge detector.
6. Morphological binary dilation and binary negation.
7. Search of connected components, size filtering, hole filling.
8. Circle identification by least square fitting.

The method was robust and detected a large fraction of the objects with almost no false positives.

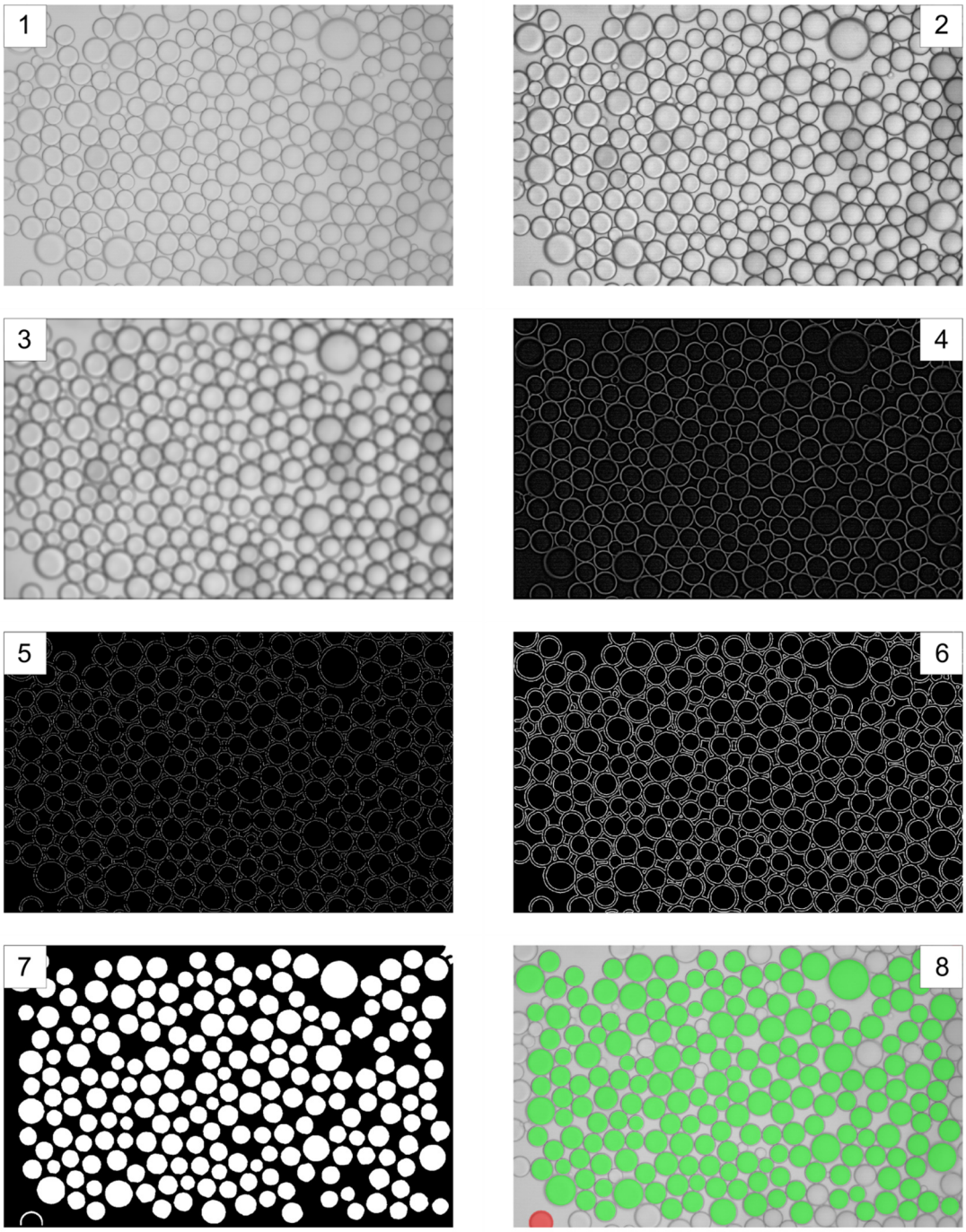

Droplet detection and size estimation. The different steps in the method are numbered according to their explanation in the main text. In (8), the green masks indicate successfully detected droplets, while the red masks indicate discarded detections due to size filtering or boundary vicinity.

Therefore, it was possible to quantify OD stability over time. Due to redistribution of the dispersed phase (oil in this case), emulsion droplets can undergo destabilization. Mainly two processes are responsible: Ostwald ripening and/or coalescence. Ostwald ripening is a process whereby the dispersed phase diffuses between droplets as a consequence of

chemical potential gradients. Coalescence is the fusion of two (or more) droplets due to the disruption of the liquid film between them and is driven by the high surface tension between the droplet and the continuous phase. The effect can be greatly reduced or stopped by adding a surfactant reducing this surface tension, which stabilizes the interface and prevents the breakup of droplets due to surface stresses or fluctuations. Block copolymer surfactants are reported to be highly efficient in stabilizing emulsions due to their strong anchoring to the oil/water interface and the formation of a thick adsorbed polymer-brush layer offering good steric stabilisation. They might suffer, tough, from the difficulty of emulsification.

To assess the stability of the droplets against coalescence we measured the size distributions of the droplets at different shelf times. The results are summarised in Figure 5.3 for the different droplet types and emulsification methods as reported in the main text.

The short-time stability (2 days) was excellent for all six different combinations of droplets and methods. No appreciable change in mean size or polydispersity was visible. For the membrane emulsification (ME) and microfluidic (μFL) droplets, this is thought to be a consequence of the stable film formed by the surfactant on the interface. For the ultrasonic (US) droplets, in addition to the previous effect there was an increased diffusion due to the small droplet size, which should have decreased creaming and hence enhanced stability.

Long-time stability (3 months) varied between the different emulsification methods. Both the ME droplet populations showed an increase in the mean size and PDI signalling a flattening of the size distribution and a shift toward higher values. The μFL droplets showed almost no change in the distribution parameters: the diblock/hexadecane showed a negligible mean size shift while the triblock/silicone oil droplets displayed a shift of approximately 1.5 μm in the mean size. The US droplets were similar to the ME ones: both populations showed an increase in mean size and PDI, the effect being more visible for the F108 droplets.

Assuming that the film stability for both oil-surfactant combinations was roughly comparable, the previous observations suggest that Ostwald ripening (and not coalescence) was the primary cause of droplet destabilisation in our system. The μFL droplets provided an excellent case in support of this hypothesis. The diblock copolymer droplets were almost monodisperse while the F108 were a bit more polydisperse. The destabilisation over long shelf time was appreciable only for the F108 droplets,

correlating with their polydispersity. Thus, Ostwald ripening (an effect mostly appreciable in polydisperse systems) might be the primary cause of the shift in mean size. The US droplets confirm this hypothesis: the F108 droplets had a larger starting PDI and showed the largest shift in the mean size.

In conclusion, both the adopted surfactant-oil combinations lead to a stable polymeric surfactant film between droplets, preventing coalescence. Observations showed that shifts in droplet sizes over long shelf times had likely been caused by Ostwald ripening, which had a slow rate in both our systems (di- and triblock copolymer) due to the oil adopted having a large molecular weight.